Exploring twisted bilayer graphene with nano-optics

by

Niels Caspar Herman Hesp

Thesis Advisor:
Prof. Dr. Frank H.L. Koppens

ICFO – Institut de Ciències Fotòniques
UPC – Universitat Politècnica de Catalunya

October 2021

Thesis committee:

Prof. Dr. Dmitri Basov (Columbia University, United States)
Prof. Dr. Marco Polini (University of Pisa, Italy)
Prof. Dr. Georgia Papadakis (ICFO – Institut de Ciències Fotòniques, Spain)

Abstract

Nano-optics studies the behaviour of light on the nanoscale. In particular, it probes the interaction of light with objects, often of nanometre-size, and reveals fine details of the material's optical properties. Optoelectronics is an integral part of optics and describes the interaction between light and electronics, such as the detection of light and subsequent conversion to an electrical signal. Understanding such mechanisms at the nanoscale is of importance for improving imaging and light-harvesting applications. In this Thesis, we apply near-field microscopy to study optics on the nanoscale. It probes optical properties using light interacting with the near-field electromagnetic field near the material's surface.

Twisted bilayer graphene (TBG) is formed by stacking two layers of graphene — a one-atom-thick sheet of carbon atoms — with a small twist angle. This causes an interference pattern in the atomic lattice called a moiré pattern, which affects the electronic properties dramatically. The discovery of unconventional superconductivity in TBG in 2018 made it a thriving field of research. Adding to this, TBG revealed strongly correlating states and topological features, making it a host of tunable exotic phases that may shed light on the origins of unconventional superconductivity. These phenomena motivate us to study the optical properties of TBG on a nanoscale, which have received little attention thus far.

In the first part of this Thesis, I describe spatially oscillating patterns within selected regions of TBG that we detected using near-field microscopy. We interpret them as a manifestation of plasmons — electrons moving collectively in a wave-like pattern — driven by interband transitions. We model these areas with a reduced interlayer coupling, which enhances the strength of interband transitions and explains the observed plasmon dispersion.

After this, I discuss large-scale periodic features observed in minimally twisted bilayer graphene ($\theta < 0.1^\circ$) by photocurrent nanoscopy. For these small twist angles, the atoms rearrange in triangular domains separated by a network of domain walls. We find that the domain walls convert heat injected in the domains into a measurable current via the photothermoelectric effect. Our results uncover the sharp changes in electronic properties at the domain walls, which govern the optoelectronic response.

I focus in the second part of the Thesis on the development of new experimental techniques, which enable nano-optical studies on exotic states of TBG and its relatives. I show that the semiconducting material WSe_2 can be used as an ambipolar transparent top gate for infrared near-field experiments. This enables full control of the carrier density and transverse displacement field without blocking near-field access.

Hereafter, I describe a commercial cryogenic near-field microscope with a base temperature of 10 K, which required modifications for reliable operation. I present an active damping system to oppose the vibrations in the system and enhance the mechanical stability. We further improve the AFM stability by changing the AFM excitation position.

In the final two Chapters I examine the photoresponse of TBG at low temperature. We observe semi-periodic modulations across our sample, which we believe manifests a second-order superlattice arising from TBG aligned to the hBN substrate in combination with strain. In a different sample, we reveal a spatially inhomogeneous response from which we deduce a map of the local twist angle.

Resumen

La nano-óptica estudia el comportamiento de la luz en la nanoescala. En particular, mide la interacción de la luz con objetos, normalmente de tamaño nanométrico, y revela los detalles de las propiedades ópticas del material. La optoelectrónica es una parte integral de la óptica y describe la interacción entre la luz y la electrónica, como por ejemplo la detección de la luz y su sucesiva conversión a una señal eléctrica. Entender estos mecanismos en la nanoescala es de vital importancia para mejorar sus aplicaciones en imagen y en captación de luz. En esta Tesis, aplicamos la técnica de microscopía de campo-cercano para estudiar óptica en la nanoescala. Medimos las propiedades ópticas usando luz que interacciona con el campo electromagnético cercano a la superficie del material.

Una bicapa de grafeno rotada (TBG por sus siglas en inglés) se forma al apilar dos capas de grafeno — una lámina de carbono de un solo átomo de grosor — con un pequeño ángulo entre ellas. Esto provoca un patrón de interferencia en la red atómica que se llama patrón moiré, que afecta las propiedades electrónicas dramáticamente. El descubrimiento de superconductividad no-convencional en TBG en el 2018 lo convirtió en un campo de investigación en auge. Además, el TBG ha revelado estados fuertemente correlacionados y características topológicas, convirtiéndolo en un portador de fases exóticas ajustable que podría arrojar luz sobre los orígenes de la superconductividad no-convencional. Estos fenómenos nos motivan a estudiar las propiedades ópticas del TBG en la nanoescala, que hasta ahora has recibido poca atención.

En la primera parte de esta Tesis, describo patrones que oscilan espacialmente dentro de las regiones seleccionadas de TBG que detectamos usando microscopía de campo-cercano. Los interpretamos como la manifestación de plasmones — electrones moviéndose colectivamente en un patrón ondulatorio — promovidos por transiciones inter-banda. Modelamos estas áreas con un acoplamiento inter-capa, lo cual mejora la fuerza de las transiciones inter-banda y explica la dispersión plasmónica observada.

Después de esto, hablo de características periódicas de gran escala observadas en bicapas de grafeno rotadas mínimamente ($\theta < 0.1^\circ$) usando nanoscopía de fotocorriente. Para estos pequeños ángulos, los átomos se reagrupan en dominios triangulares separados por una red de paredes de dominio, que gobiernan la respuesta optoelectrónica.

En la segunda parte de la Tesis me concentro en el desarrollo de nuevas técnicas experimentales, que permiten estudios nano-ópticos en estados exóticos de TBG y familiares. Enseñaré que el material semiconductor $\mathrm{WSe_2}$ puede ser usado como una puerta superior para experimentos de campo-cercano en el infrarrojo. Esto permite un control completo de la densidad de portadores y del campo de desplazamiento eléctrico sin bloquear el acceso del campo-cercano.

Sucesivamente, describo un sistema comercial de microscopía de campo-cercano con una temperatura base de 10 K, que requirió modificaciones para una operación fidedigna. Presento un sistema de amortiguación activa para contrarrestar vibraciones en el sistema y mejorar la estabilidad mecánica. Continuamos mejorando la estabilidad del AFM cambiando la posición de su excitación mecánica.

En los dos capítulos finales examino la fotorespuesta del TBG a temperaturas bajas. Observamos modulaciones semi-periódicas en nuestra muestra, que creemos que manifiesta una super-red que proviene del TBG estando alineado con el substrato de hBN en combinación con deformación. En una muestra diferente, revelamos una respuesta espacial inhomogénea con la que deducimos un mapa del ángulo de rotación.

Prologue and acknowledgements

In my view, this Thesis comprises a summary of the meaningful and interesting results that were acquired in the past five years. As some might know, I prefer things to be well organized and planned, yet, I have to find out that most results were not the outcome of any well-defined experimental plan. In fact, it turns out that there is practically no overlap with the Thesis Proposal that was written four years ago. It has taught me to avoid careful planning where possible. With research being unpredictable, most schedules are not met and, consequently, only cause stress. Instead, just working systematically with an ordered task-list is more effective.

Within the largely untouched field of twisted bilayer graphene, conducting the experiments felt like a real exploration, especially with novel optical techniques. This excited me nearly every day when getting up and walking to the ICFObus. I experienced the finest, though scarce, moments when conducting experiments that suddenly yielded unexpected results. Figures 3.1b, 4.2, 5.5a and 7.3 are examples of this, whose appealing patterns appeared on the measurement screens in nearly the same way. A second round of joy and satisfaction came in the exact moment of 'decoding' the photocurrent maps (Chapters 4, 7 and 8). It felt like solving a puzzle, searching for the underlying structure that fits the observed patterns. Altogether, this illustrates to me the beauty of science.

This involved quickly adapting to new techniques, which was particularly encouraged by Frank. Just four weeks after starting my PhD, with a half-day crash course from Achim on using the s-SNOM, I was sent to Rainer Hillenbrand's lab in San Sebastián with the most precious device alive in our group: the 'Columbia'-device. The week after, the same device had to be measured in the lab of Miriam Vitiello in Pisa, where the electric sparks were literally coming from optical tables. Fortunately, after a mental struggle, on the very last evening we obtained the desired results while keeping the device alive. In a similar fashion, when I was in Alexey Kuzmenko's lab in Geneva struggling with electronic noise in their cryoSNOM, Roshan had to be flown in as the 'transport-expert' (just because he did his PhD in Andre Geim's lab), three full days after he joined ICFO. However, no fundamental problems caused the noisy signals: it was a matter of wrapping aluminium foil around the cables to shield them.

Speaking about the cryoSNOM: this whole project seemed to be plagued by Murphy's law ('Anything that can go wrong will go wrong'). It arrived by the end of 2019, more than three years after Frank was awarded the required ERC grant. Main culprit was a near-perfect match of our floor resonance at 16 Hz, with those of the springs inside the cryoSNOM. These strong floor vibrations came as a surprize, in particular considering that 'there is no metro passing underneath ICFO'. With all the basement space filled, we had to be creative in finding a solution for this rather comprehensible problem. To our astonishment, small piezo-ceramic blocks formed key in the solution. A thin 1x1 cm^2 layer of this material is able to set 200 kg into motion under the application of a voltage, which, when set up correctly, counteracts the disturbing vibrations in the system.

Obtaining the results presented in this Thesis has only been possible with the help of others, which I like to acknowledge in the following. In addition, I received funding from the European Union's Horizon 2020 programme under the Marie Skłodowska-Curie grant agreement Ref. 665884 and from the ERC grant agreement Ref. 726001.

I first wish to thank Frank for offering me the opportunity to spend the past years in the nano-optoelectronics group at ICFO. Your approach of presenting a general vision, defined by the measurement technique and device architecture, while leaving sufficient freedom in carrying out the experiments, has worked out very well. As soon as something interesting popped up in a running experiment, your involvement becomes even more apparent by appearing daily in the lab. Instead of putting pressure on me (to which I am insensitive), your motivation achieves an encouragement that made experiments successful. To me, it was without doubt the right choice to pursue a doctorate under your supervision.

Research greatly benefits from collective efforts, and I had the luck to be surrounded by a fantastic group of people that directly contributed to the scientific results discussed in this work. In particular, I wish to thank Daniel, Yuan, Petr, Hanan, Pandian and Yuanda for putting their samples under investigation in our experimental setups. I am especially indebted to Daniel and Petr, who provided their best pre-characterized magic-angle samples, and never gave up after numerous of them did not survive the near-field studies. During the measurements, if any help was needed, David and Hanan always stood ready, and Sergi has become the new cryoSNOM-expert while I was writing my Thesis. There was also no shortage of listening ears that were continuously open for discussing new ideas or results. A five-minute chat with Iacopo, Roshan, Petr or Frank was often more effective than sitting an hour alone in the office. Likewise, the Python tools developed by Iacopo and Pietro greatly simplified calculations. Lastly, the welcoming visits to the labs of Alexey Kuzmenko, Rainer Hillenbrand, Khaled Karrai and Miriam Vitiello were a great pleasure and insightful in many aspects.

I am thankful for all the institutional support that ICFO has offered, allowing me to conduct the experiments in an effective manner. In particular, Carlos and his team did a fantastic job in setting up the heavy equipment in L208 with a non-stop dedication. In a similar fashion, I am going to miss the blazing-fast purchasing process managed by Santi and Magda, for whom one reference is sufficient to have the item at ICFO the next day. I spent a substantial part of my time in the cleanroom facilities, always well taken care of by Luis, Johann and Xavi. José and this team from the electronic workshop showed a great craftsmanship, and likewise did Xavi and his team from the mechanical workshop. Moreover, Laia, Anne and their colleagues smoothly coordinated the administrative processes and, finally, I thank all the ICFOnians working behind the scenes in making ICFO a wonderful place to be.

Furthermore, I am pleased with the help I received in writing this Thesis. Iacopo, Frank, Petr, Roshan, Shuchi and the committee members critically proofread the Thesis and suggested numerous improvements. Sergi kindly translated the abstract to Spanish, and Blender-expert Matteo made an artistic illustration of collective excitations in twisted bilayer graphene, presented on the cover. In addition, Laia and her colleagues arranged the formalities in the process towards the Thesis defence.

The nano-optoelectronics group led by Frank has been a great team to be part of. The shared motivation, yet with an informal and easy-going mood, creates an enjoyable environment to spend every day. The various group outings, dinners and pizza-served journal clubs testify to this. Notably, throwing snowballs between two jacuzzis in a real

igloo-complex was something new to me. It has been a great time in the office, shared with Hanan, Iacopo and David, where the number of objects and sheets of paper on (and under) the table uniquely define everyone's desk. It was a privilege to share the office with our group's only in-house theorist, Iacopo, who is always ready to explain basic questions on physics.

The countless explorations in the rural countryside have been the perfect way to escape life at ICFO. Together with Shuchi, Anika, Callum, Zafer, Christina, Richard, Anne and Nick, nearly every mountain peak in Catalunya was reached, while Aamir, Iacopo, Roshan, Hara, Achim and Rafaël joined us to get a taste of the broad variety of food in Barcelona.

Ik ben ontzettend dankbaar voor alle steun van mijn ouders, zussen en aanhang. Jullie hebben de brede interesse, discipline en motivatie in voorgaande jaren aangebracht die mij op het pad hebben gezet dat tot ICFO leidde. Al is het op afstand, jullie constante belangstelling voor ons leven in Spanje maakte het altijd prettig om onze ervaringen te delen.

Last, but not least, I am immensely happy to have Shuchi with me in the past years. It has been the foremost benefit of the laser safety course, where we met each other. I could share all my excitement about plasmons and frustration about the cryoSNOM with you. Not surprisingly, you often said 'your PhD is my PhD', reminding me each time that you suffered probably more than I did when I spent evenings in the lab or gave up the weekends in writing this Thesis. I hope that the relief is also shared. Your charm, care and love has made this journey in Barcelona a truly wonderful period, which only marks the beginning of the bright future ahead for the two of us.

Contents

1. Introduction

This Chapter introduces the physics of twisted graphene structures. First we discuss the main features linked to the moiré superlattice, followed by an overview of the recent experimental developments in this field. We finish by outlining the aims and structure of this Thesis.

The experimental discovery of graphene in 2004 marked the advent of two-dimensional (2D) materials as an exciting new field to be explored[1,2]. By now, the community efforts have led to a rich palette of 2D materials[3]: semimetals like single- and multilayer graphene[1,2], insulators like hexagonal boron nitride (hBN)[4], the class of transition metal dichalcogenides serving as semiconductors[5], superconductors such as BSCCO[6], and ferromagnets like $\mathrm{CrI_3}$[7]. Only several years later, it became clear that stacking various 2D materials leads to a new series of phenomena, linked to their 'third dimension'[3]. The mechanical stability in such heterostructures is guaranteed by the relatively weak van der Waals forces between these layers[3]. Whilst such structures are still only nanometres thin, their properties are strongly modified by the interaction between the different layers, which has led to various discoveries. Examples include the enhanced phonon-limited mobility in graphene[4,8,9], the fractal-like energy spectrum known as the Hofstadter butterfly[10–12], and the electrons gas acting as a hydrodynamic liquid[13,14].

Thus far, the twist angle between different layers remained uncontrolled when creating these heterostructures. This changed in 2016, when the tear-and-stack technique was introduced. It consists of cutting a single 2D crystal in two parts, followed by placing one part on top of the other at a controlled twist angle θ[15,16]. In 2018, a breakthrough was made leading to a new impulse in the field of graphene. By rotating two graphene monolayers with respect to each other by a 'magic angle' $\theta \approx 1.05^\circ$[17], this system can be brought into a superconducting state for temperatures below 2 K[18]. This particular state in magic-angle twisted bilayer graphene (MATBG) shares several similarities with unconventional superconductivity, while being a highly tunable material via the *in situ* adjustable carrier density. The physics behind this discovery originates from the dramatic changes in the band structure occurring for small twist angles between two graphene sheets[17,19–21]. An emerging set of flat bands with high density of states leads to correlated insulator states, topological physics like the anomalous Hall effect, and superconductivity[18,22–31].

This broad variety of phenomena motivates us to study the optical properties of twisted bilayer graphene, which have retrieved little attention thus far. In particular, we will use a scanning probe technique to explore them on the nanoscale.

1.1. Moiré patterns in twisted graphene structures

A moiré pattern is an emerging periodicity that arises when two lattices are placed on top of each other at a small relative angle. This periodicity is determined by the periodicity of the underlying lattices and twist angle. As illustrated in Figure 1.1a, such superlattice can be as simple as two sets of lines with a relative rotation. In more complex structures like a honeycomb lattice, such rotational misalignment causes the formation of a large-scale triangular superlattice (Fig. 1.1b). By superposing two lattices with slightly different periodicities a moiré pattern can be obtained without twisting the layers.

The moiré structure does not repeat exactly upon translation by the superlattice periodicity, as a rigorously periodic structure only occurs for a set of commensurate angles[19,32]. However, we can use an approximate description in terms of a periodic lattice, as long as the superlattice periodicity is much larger than the periodicity of the underlying lattices. Such a description goes under the name of continuum models and allows the use of all concepts of periodic lattices, such as the Bloch theorem and the Brillouin zone.

When two real crystals are stacked on top of each other with a certain twist angle, the

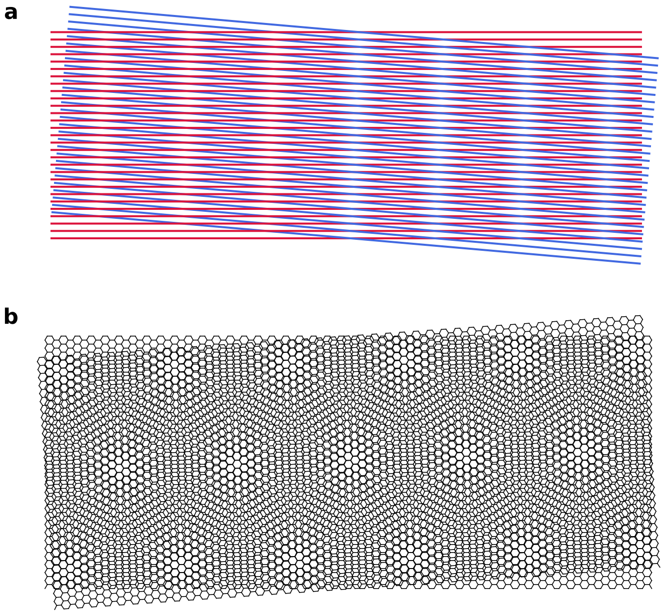

Figure 1.1: Formation of moiré superlattices. **a** By superposing two sets of periodic lines at a small relative rotation, a new larger periodicity emerges referred to as a moiré pattern. **b** By slightly misaligning two honeycomb lattices (such as graphene) a triangular moiré lattice is formed. The AA sites of this superlattice are those where the two sheets perfectly overlap with each other, while the AB/BA regions correspond to the Bernal-stacked areas.

actual positions of atoms can deviate from the ones predicted by the rotation of two rigid lattices[33,34]. This rearrangement of atoms minimizes the total energy of the superlattice and is called lattice relaxation. This causes corrugation and distortion of the superlattice, and is especially important when the twist angle is small.

Also in twisted bilayer graphene (TBG) such moiré pattern emerges by superposing two graphene sheets with hexagonal lattices at a small twist angle θ (Fig. 1.1b). The triangular superlattice has a lattice constant d that is related to θ by $d = a/[2\sin(\theta/2)]$, with $a \approx 0.246$ nm being the lattice constant of single-layer graphene[17,19–21]. For the 'magic angle' $\theta \approx 1.05°$, the moiré periodicity is about 13 nm. The top view of TBG shown in Fig. 1.1b reveals regions where the two sheets are locally in the AA-stacking configuration surrounded by regions where the stacking configuration is of the energetically-favoured AB- or BA-type (Bernal stacking)[34].

Electrons can tunnel from one layer to the other with a tunnelling amplitude that depends on the local alignment between the two layers[17,19]. Consequently, the interlayer tunnelling amplitude is spatially modulated with the periodicity of the moiré lattice. Effectively, this produces a longitudinal and transverse potential, which both act on graphene's Dirac fermions[35]. These two potentials have an amplitude on the order of 100 meV, and localize electronic states close to the charge neutrality point (CNP) in the regions where the alignment between the two layers is an AA-like configuration[18,22,32,36].

In a band structure picture and owing to these two potentials, a pair of narrow energy

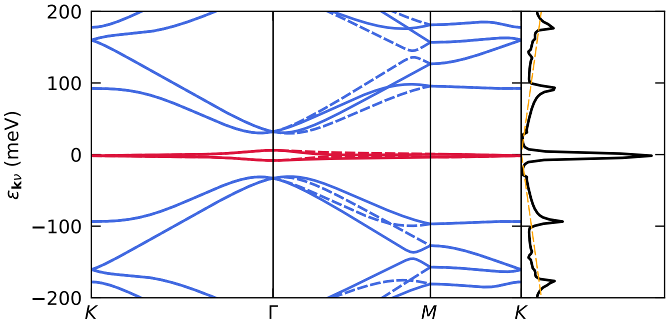

Figure 1.2: Electronic band structure of magic angle twisted bilayer graphene. Calculated band structure according to the single-particle description[38] for $\theta = 1.05°$. Solid (dashed) lines represent the bands in the valley close to the K (K') point of the original graphene layers. The flat bands are plotted red, which lead to a sharp peak in the density of states (right panel), while the bands in blue are referred to as the remote bands. The dashed orange line corresponds to the density of states of single-layer graphene.

bands forms close to CNP at the magic angle, as depicted in Fig. 1.2. Because of their flatness, the electrons move at a greatly reduced speed across the lattice and cause a high density of states, which is part of the reason why these topological bands are held responsible for the observed correlated phenomena[18,22–31]. Switching off the scalar potential enhances the flatness of the bands making them perfectly flat throughout the superlattice Brillouin zone at the magic angle[35,37].

Lattice relaxation in TBG is of importance for the twist angles we are interested in ($\theta < 2°$)[39,40]. Especially, minimally twisted bilayer graphene (mTBG, $\theta < 0.1°$) exhibits an extreme form of lattice reconstruction, wherein the lattice changes radically into alternating triangular domains of AB/BA Bernal-stacked regions separated by a network of narrow

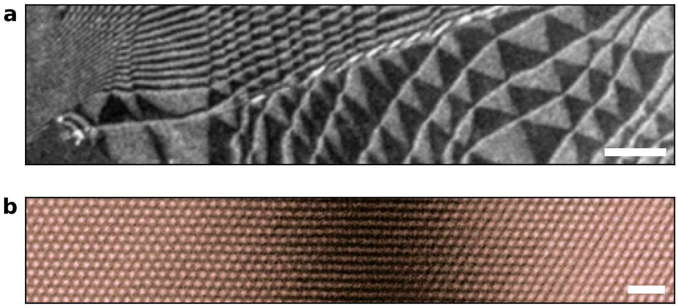

Figure 1.3: Lattice relaxation in minimally twisted bilayer graphene. **a** TEM image of domain structure formed in minimally twisted bilayer graphene due to lattice reconstruction. The light/dark triangular regions correspond to the AB/BA domains, separated by thin domain walls. Scale bar is 150 nm. **b** Zoom of the registry shift occurring at a domain wall, where the graphene lattices displace smoothly with respect to each other. Scale bar is 1 nm. Both panels are adapted from Ref. 33.

domain walls[33,39,41,42] (Fig. 1.3). The changes in the atomic registry through the domain walls cause a dramatic change of the local electronic properties over a length scale of ~ 10 nm[33]. These domain walls are of particular interest due to the topological states they host[42–45]. We note that this phenomenon is generic for twisted 2D materials, and similar extreme reconstruction effects are present in other systems[46].

1.2. Recent experiments on twisted graphene

Twisted bilayer graphene has been explored before superconductivity and strongly correlated states were found in 2018[18,22]: initial scanning tunnelling spectroscopy experiments confirmed the presence of flat bands[21]. These weakly-dispersive bands lead to van Hove singularities, which are sharp peaks in $\nabla_{\mathbf{k}}\epsilon_{\mathbf{k}}$, and manifest themselves as peaks in the density of states that were seen in these experiments.

Once the right techniques became available to twist the graphene layers in a controllable fashion[15,16], it was shown how the twist angle could easily be determined. This is a typical starting point for experiments because of the sensitivity of occurring phenomena on the twist angle, especially near the magic angle. A transport experiment showed that a peak in the resistance at 'full filling' carrier density n_s is linked to the twist angle $\theta \approx \sqrt{\sqrt{3}d_0^2 n_\mathrm{s}/8}$ in radians[15]. This particular carrier density corresponds to four carriers per superlattice unit cell and completely fills or empties the flat bands (Fig. 1.2). A more precise approach to determine the twist angle requires mapping of the Landau levels in a magnetic field[22]. Another technique involves measuring Brown-Zak oscillations in the magnetoresistance, with a frequency dependent on the twist-angle[47].

Thus far, a variety of experimental probes has been used to explore the physics of TBG, including electronic transport[18,22–26,39], quantum capacitance[27], scanning tunnelling microscopy[21,28–31], scanning magnetometry[48] and local compressibility[49,50]. We discuss three particular lines of investigations.

Transport experiments laid the first stones towards understanding the phase diagram of TBG and its relatives, primarily because the lowest temperatures (~ 10 mK) are only accessible via this route. It revealed a flavourful phase diagram, shown schematically in Fig. 1.4. It consists of band insulators at filling factors $\nu = \pm 4$ (full filling), corresponding to either 4 holes or electrons per moiré unit cell, and correlated insulating states at integer filling factors that become less resistive in an applied magnetic field. In some cases (varying between samples), superconducting domes appear adjacent to the correlated insulating states, yielding a strong analogy with unconventional superconductors. The obvious question arose to what extent the superconducting and correlated states have a common origin, and to what extent they compete with each other. By varying the degree of electronic screening in experiments, it became clear that each of the phases can exist without the presence of the other, suggesting these phases to be not tightly bound to each other[51–54]. Especially the superconducting states benefit from stronger electron-electron (e-e) correlations, in other words, a stronger Coulomb interaction[54].

These correlated phases in MATBG arise from strong electron-electron interactions. To understand its origin, we consider the Hamiltonian $\mathcal{H} = H_\mathrm{k} + V_\mathrm{ee}$, where H_k accounts for the kinetic energy and the interaction with the lattice, and V_ee describes the e-e interactions. Owing to the flat bands, the kinetic energy of the corresponding states is small. This causes the single-particle term H_k to quench, which means that H_k can be regarded as a

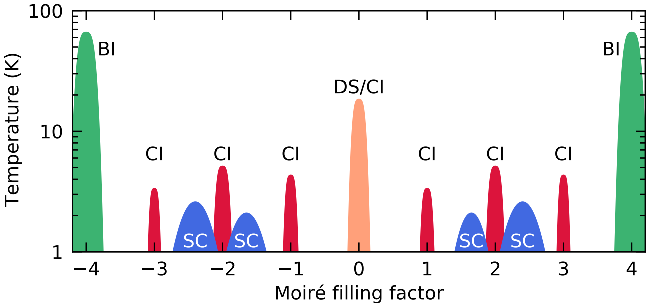

Figure 1.4: Phase diagram of twisted bilayer graphene. Schematic illustration of a typical phase diagram measured in MATBG. The moiré filling factor ν indicates the number of electrons per moiré unit cell. $\nu = \pm 4$ corresponds to completely empty or filled flat bands, at which the system acts as a band insulator (BI). For the other filling factors, correlated insulating (CI) states occur, with superconducting (SC) domes surrounding them. At CNP ($\nu = 0$) the system is in a Dirac semimetal (DS) or CI state.

constant and effectively drops out of the Hamiltonian. As a consequence, only the term V_{ee} remains and e-e interactions dominate the physics in MATBG. A series of electronic phases emerges from strong e-e interactions, which manifest themselves as correlated insulating states, superconductivity, and ferromagnetism[25,26]. The latter is rather peculiar given the non-magnetic nature of the carbon atoms. The e-e interactions can also be linked to a degree of nematic order found in MATBG, which was observed as a change in the electronic properties along different spatial directions[28,29,31,55].

In the case of minimally twisted graphene, transport experiments are challenging due to the inhomogeneous nature of the superlattice. Yet they showed that the topological nature of the domain wall network has a strong influence on electron transport properties[45,56–58].

The main drawback transport experiments face is that they probe physics only on a global scale, while details on a nanometric scale remain hidden. In particular, twisted heterostructures are expected to exhibit twist-angle inhomogeneity, because of its tendency to rotate back into alignment[59–61]. Therefore, local scanning probe measurements are of great value as they allow mapping various properties on a length scale similar to the moiré unit cell. Scanning SQUID and STM measurements were able to measure locally the twist angle and determined its variation to be $\pm 0.05°$[48,62]. STM measurements visualized the periodic potential modulation and provided an insight into details of the band structure such as the gap sizes and strength of the e-e correlations[21,28–31]. Local compressibility measurements revealed that while adding carriers in these bands, a phase transition occurs at each integer filling, where all carriers are being taken by a single spin/valley flavour[49]. Especially for mTBG local probes are essential, given its dramatic structural changes across relatively long distances ($\sim$ 100 nm or more). It is particularly useful to study the lattice relaxation dynamics[40,63–65] in mTBG, as it helps in understanding the lattice reconstruction in MATBG[40]. Scanning probe experiments also extended beyond twisted graphene structure, demonstrating ferroelectric behaviour modulated across the formed domains in minimally twisted structures based on hBN crystals[66–69].

Optical studies involve exciting an electron from one band to a higher available state, which in the case of MATBG is interesting due its flat bands (Fig. 1.2). The large degree of band nesting between the flat and remote bands leads to a resonance in the absorption spectrum[70,71]. As the distance between the bands grows with twist angle (Appendix A.4), the optical spectrum could in principle serve as a fingerprint to identify the twist angle[72]. The energy bands are predicted to change with carrier density[73], which could also be observed optically. In addition, the rotational misalignment allows for an inherently chiral response[74,75]. With a distance between the bands or approximately 100 meV between the M and K points, the dominating region of interest lies in the infrared spectrum. As the infrared free-space wavelength is similar to typical device sizes, this poses a hurdle for far-field experiments and explains why most optical experiments performed on TBG (or graphene on aligned hBN) employed near-field optical probes[41,76–79]. In particular for mTBG structures, nano-optical probes were used to visualize the domain wall network through the reflection of plasmon and phonon polaritons on the domain walls[41,78,79].

Currently, one of the main open challenges in the field is the control of twist-angle disorder[80]. This is of importance, as for instance modest twist-angle inhomogeneity can hinder the formation of a continuous superconducting path between two leads. Broadly speaking, a more uniform moiré lattice will allow more exotic phases to exist. This requires improvements in fabrication techniques, guided by precise characterizations of the twist-angle inhomogeneity. Another direction recently attracting more attention is the effect of a transverse electric field between the two graphene layers. Under such displacement field, the AB/BA regions open locally a gap, which strongly modifies the physics of magic angle twisted graphene systems[81,82]. In the case of minimally twisted bilayer graphene, the gap opening under a transverse field could enable low-loss plasmon propagation within the domain wall network[83,84].

1.3. Aim and outline of this Thesis

The techniques discussed in the previous Section are sensitive only to the static (very low frequency) response of the system. In systems like TBG where e-e interactions play a dominant role, experimental techniques that probe the response to perturbations carrying a finite in-plane wavevector q and angular frequency ω are expected to be rich sources of information. One of these techniques is scattering-type scanning near-field optical microscopy (s-SNOM)[76–78,85,86], which enables with a spatial resolution of 20 nm the measurement of the dispersion relation of collective electronic excitations, such as Dirac plasmons in doped graphene[85–87]. Several works have predicted collective excitations in TBG structures[83,84,88–92], for which s-SNOM is particularly suited. These predictions include interband plasmons in charge-neutral TBG[89,91], undamped intraband plasmons within the gap of TBG[90,92], and topologically protected plasmons within a domain wall network[83,84]. The advantage of local probing techniques over global transport methods is an additional reason for us to choose s-SNOM as the main technique for our investigations.

With only minor adaptations, an s-SNOM system allows us to perform nanoscale photocurrent measurements as well. This technique has proven itself as a tool for optoelectronic studies on graphene-based devices[93–96]. This encourages us to perform photocurrent nanoscopy on twisted graphene structures to study its optoelectronic response. A general prerequisite for such photo-induced currents is the lack of an inversion centre, whether it is extrinsically defined by doping inhomogeneity in the form of pn-junctions, or due to a broken inversion symmetry in the crystal structure. In this regard, the structures of moiré superlattices[10–12,15,97] are well suited for photoresponse applications, since the crystal symmetry can be easily reduced by a twist-angle induced atomic-scale reconstruction[39,98]. The sharp changes in electronic spectra can serve as local junctions, thus providing an intrinsic photoactive region created by the moiré superlattice. Such changes can form due to the domain structure in mTBG. Likewise, small twist-angle variations typically present in magic angle samples can act as built-in junctions, allowing for optical mapping of twist-angle disorder.

Considering the recent development on twisted nanostructures described in this introduction, together with the focus on nano-optoelectronics in the group of Prof. Koppens, we define two objectives at which we aim the work of this Thesis: i) understanding the optical and optoelectronic properties of twisted bilayer graphene systems and their connection to the fundamental structure of these systems; ii) establish new techniques to study the exotic states of twisted graphene systems at low temperatures.

Keeping this in mind, we structure the work comprised in this Thesis as follows:

- In Chapter 2 we outline the experimental techniques employed in this work. First we discuss the steps involved in device fabrication, and subsequently describe the principles behind s-SNOM and photocurrent nanoscopy. Two examples demonstrate how these tools can be used to measure collective excitations and their characteristics.

- In Chapter 3, we apply s-SNOM to study the optical properties of twisted bilayer graphene near the magic angle, with an emphasis on collective excitations related to the moiré minibands. Our data reveal a plasmonic excitation in undoped TBG directly related to the interband transitions from the flat to remote bands. Its dispersion points to a reduced tunnelling strength at the AA-stacked regions, which might originate from screening owing to e-e interactions.

- In Chapter 4 we unravel the optoelectronic response within a single moiré unit cell of minimally twisted bilayer graphene. Our measurements reveal a spatially rich photoresponse, whose sign and magnitude are governed by the fine structure of the moiré lattice and its orientation with respect to measurement contacts. This results in a strong directional effect and points towards a photothermoelectric induced response. We finally show how phonon polaritons are able to interact with domain walls and influence the measured photoresponse.

- In Chapter 5 we demonstrate the suitability of WSe_2 as an ambipolar transparent top gate electrode for near-field experiments. This study shows that few-layer WSe_2 is able to tune the plasmon wavelength of an embedded bilayer graphene layer, without obstructing near-field access. We experimentally extract the gating efficiency of WSe_2, that can be modelled by a combination of quantum and geometric capacitances.

- In Chapter 6 we present a cryogenic near-field microscope, enabling near-field experiments down to 10 K. It is based on a commercial system, to which we made several modification to improve its performance, with a particular focus on mechanical stability. This will allow future near-field studies of the exotic states of matter in twisted heterostructures.

- In Chapter 7 we apply cryogenic photovoltage nanoscopy to unveil a second-order superlattice in MATBG closely aligned to the hBN substrate. We find a structure of large-scale modulations covering the entire sample, and interpret it as the interference of moiré lattices formed by MATBG and graphene aligned to hBN. Our results provide a real-space visualization of broken inversion symmetry and our model shows the importance of small amounts of strain on this superstructure.

- In Chapter 8 we develop a method to measure the local twist angle in TBG using photovoltage nanoscopy. We measure a strongly varying photoresponse with position and carrier density in our sample. Guided by s-SNOM and transport measurements, we interpret the photoresponse on the bases of the photothermoelectric effect. As a demonstration of this method, we provide a map of the twist angle in our sample.
- We conclude this Thesis by summarizing our work in Chapter 9 and presenting an outlook to the horizon of this field.

2. Experimental methods

This Chapter outlines the main experimental techniques used in this work, starting with the fabrication techniques of van der Waals heterostructures. We continue by introducing the near-field optical miscrocope, which serves as the main workhorse of all studies presented here. After discussing the scattered optical signals we measure, we conclude by showing how this tool is used to measure simultaneously the photovoltage response of our samples.

2.1. Fabrication of van der Waals heterostructures

Over the recent years, fabrication of van der Waals heterostructures has become a rather standardised technique. After the realization that hexagonal boron-nitride (hBN) provides a much smoother substrate for graphene[4,8], and at the same acts as a strong dielectric, it has become the favourite choice of material for encapsulating graphene. It triggered the idea that virtually any combination of two-dimensional materials can be stacked on top of each other, opening a plethora of new phenomena to be explored[3].

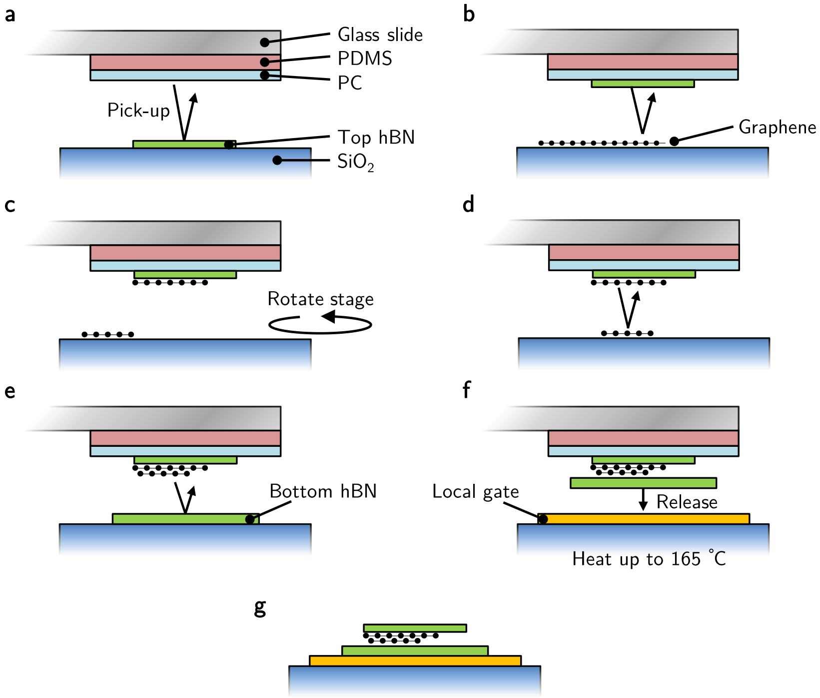

Figure 2.1: Fabrication of a twisted heterostructure. a We start with a PDMS stamp covered with a thin PC film, which we use to pick up the top hBN flake, followed by picking up part of the graphene flake (**b**). We subsequently rotate the stage by the desired twist angle (**c**) and pick up the remaining graphene (**d**). After picking up the bottom hBN flake (**e**), we heat the stage to 165 °C and release the stack onto a pre-patterned local gate (**f**). The PC film is removed by dissolving the chip in chloroform (**g**). All steps before releasing the stack are performed at 40 °C.

Figure 2.1 schematically illustrates the steps involved in fabricating a stack of twisted bilayer graphene encapsulated in hBN. It employs a thin polycarbonate film (PC) mounted via a PDMS slab onto a glass slide, to which most two-dimensional materials tend to stick well[99]. By subsequently picking up flakes, we form a heterostructure, which is usually released onto a metal or graphite local gate. In this process we twist graphene following the 'tear-and-stack' technique, where we pick up only part of a graphene flake, rotate the stage slightly, and pick up the remaining graphene[15,16]. By releasing the stack at an elevated temperature, most air bubbles become sufficiently mobile and are squeezed towards the side of the stack[100,101]. We obtain all the employed 2D materials via micromechanical exfoliation onto a Si/SiO$_2$ chip, and carefully select high-quality flakes using optical microscopy and atomic force microscopy. Since the near-field coupling to graphene decays exponentially with distance, we only use thin hBN flakes serving as top layer ($<$ 10 nm).

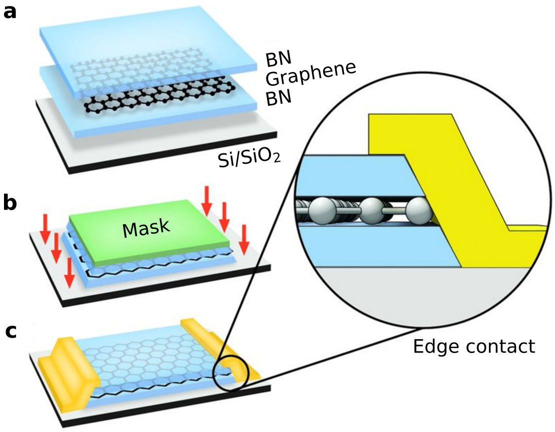

Figure 2.2: One-dimensional edge contact to graphene. **a** A van der Waals heterostructure is fabricated. **b** We shape the device by reactive ion etching (CHF$_3$ and O$_2$ gas mixture) according to a mask defined with electron-beam lithography. **c** Metal is evaporated over the exposed graphene edge, forming a one-dimensional contact. Figure adapted from Ref. 9.

To make a sample suitable for (opto-)electronic measurements, we pattern one-dimensional contacts to the graphene layers. Despite the seeming fragility, this technique actually turns out to yield robust contacts with low resistance in the order of a few 100 $\Omega\cdot\mu$m[9]. Figure 2.2 shows the steps involved in creating such contacts. Either photolithography or electron-beam lithography can be used for defining the masks. Typically, we first shape the stack to a desired structure (typically a Hall bar), after which we run another lithography process to define the position of the contacts. The hBN naturally etches at an angle $\sim 45°$, which helps in covering the exposed graphene edge with metal. Since it turns out that chromium is crucial to form a good bond[9], we typically evaporate Cr(5 nm)/Au(50 nm).

To ensure clean and flat surfaces for near-field measurements, we perform AFM-brooming after the nano-fabrication process has finished. Repeatedly scanning in contact-mode over the sample removes surface residues originating from the fabrication process[102,103]. These residues mask the fine optical and topographic features studied using s-SNOM. Additionally, this AFM-brooming procedure helps to minimize the residues picked up by the apex of the AFM tip, which reduces the loss of near-field signal during these measurements. For this cleaning procedure, we use soft tips (Nanoworld Arrow, stiffness 0.2 N/m) and scan over the surface with a typical force 20-40 nN (corresponding to a pressure of 20-40 MPa) and speed 2-4 µm/s for several hours. After this procedure, the root-mean-square roughness is 120-200 pm, which is similar to that of a pristine hBN flake[4].

2.2. Near-field optical microscopy

Accessing the optical and optoelectronic response of materials on a nanoscale is of great interest, since it offers a wealth of knowledge about their structure and physical mechanisms at play. Despite the relative easy accessibility to far-field experiments, they typically suffer from the diffraction limit that restricts the minimum resolvable distance to

$$d = \frac{\lambda}{2n\sin\theta} = \frac{\lambda}{2NA}, \tag{2.1}$$

with free-space wavelength λ and the medium's refractive index n. $NA = n\sin\theta$ is the numerical aperture of the system. For typical optical experiments using visible light, this limits the resolution to 100s of nanometres. However, as discussed in Sec. 1, the interesting energy range lies in the infrared to far-infrared. For these wavelengths, d is of similar size as the typical device size or even well beyond that, which substantially complicates far-field experiments. In addition, many phenomena have been revealed possessing characteristic length scales of tens of nanometres, which are invisible in far-field experiments.

This motivates us to use near-field optical microscopy as the main tool for our investigations, which essentially probes the near-field electromagnetic field, existing only close to the sample under study. From this, we can resolve the nanoscale spatial variations of the sample's properties, and additionally it is able to uncover collective light-matter phenomena at the nanoscale.

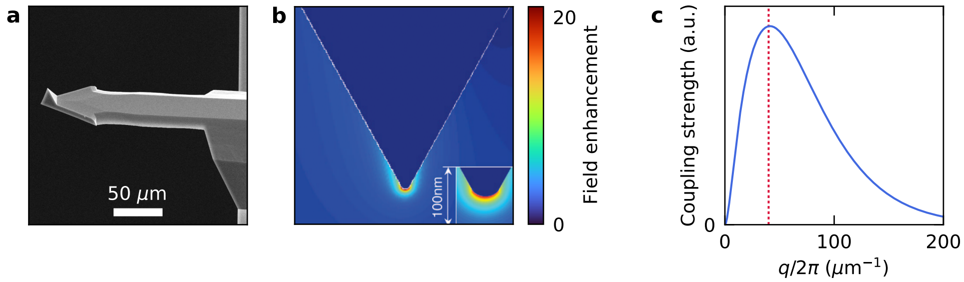

Figure 2.3: Near-field coupling with an AFM tip. **a** SEM photograph of a PtIr coated AFM tip. The apex of the triangular pyramid at the end of the cantilever interacts with the sample. **b** Enhancement of the electric field at the apex due to the lightning rod effect. Figure adapted from Ref. 104. **c** Momentum distribution of the near-field coupling strength provided by an AFM tip with a radius of curvature of 25 nm. The red dashed line marks the momentum corresponding to the inverse of the tip apex's radius. Figure adapted from Ref. 105.

More specifically, we employ a scattering-type scanning near-field optical microscope (s-SNOM), which is built around a sharp metal-coated AFM tip (Fig. 2.3a) that is illuminated with a focussed laser beam[106–109]. Due to the lightning rod effect, a sharp hotspot of light forms at the apex of the tip that can interact with the sample, as shown in Fig. 2.3b. The main implication is that we can bypass the far-field diffraction limit and couple light into the sample on a scale only defined by the sharpness of the apex. In fact, the evanescent waves forming the hotspot of light carry a broad spectrum of momenta[105], as depicted in Fig. 2.3c. This is an essential ingredient for exciting highly confined plasmon-polaritons carrying momenta up to two orders of magnitude larger than the momentum of light in vacuum (for single-layer graphene), and makes s-SNOM an ideal technique for imaging propagating plasmons in graphene-based devices[87,110–112] and phonon polaritons in other layered materials[85,86,113].

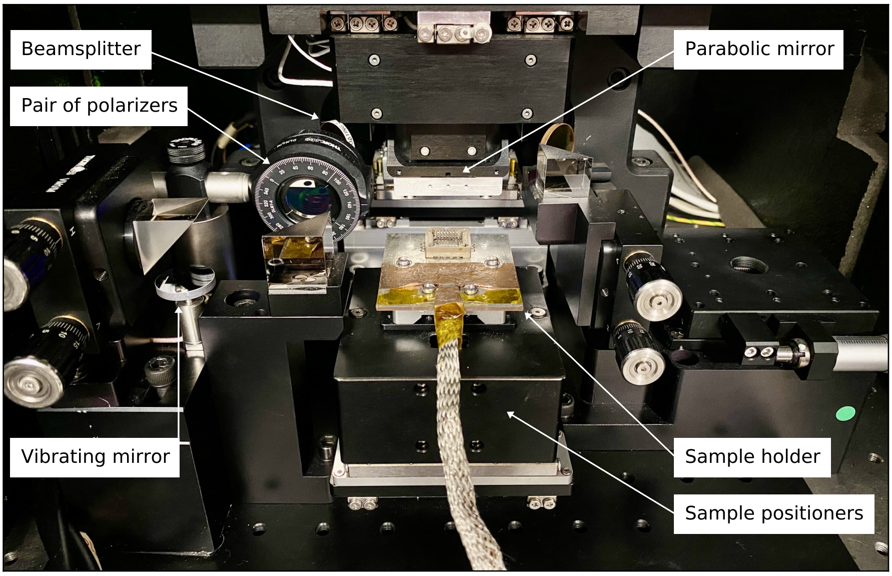

Figure 2.4: Commercial s-SNOM system by neaspec. Photo of our s-SNOM system operated in ambient conditions, with the key components labelled. Samples with electrical connections are mounted in a 28-pin chip carrier, and connected via a flexible cable. The complete system is placed in a box for acoustic isolation, and can be flushed with nitrogen gas to lower the chance of discharges in air caused by the high voltage on the Si gate.

The near-field measurements presented in this work are carried out with a commercial s-SNOM system (neaspec), as shown in Fig. 2.4. A tunable quantum cascade laser (Daylight Solutions) and a CO_2 gas laser (Access Laser) are used as mid-infrared light sources for energies between 100-300 meV (4-12 μm) with a typical power of 10-40 mW. In addition, we can couple in a THz beam generated by gas laser (Edinburgh Instruments) at discrete energies between 5-15 meV (1-4 THz) at a similar power. This light is focussed on the metal-coated AFM tip, for which we use the Arrow model shown in Fig. 2.3a to simplify alignment (Nanoworld, PtIr coating). This model has an apex with a radius of curvature of ≈ 25 nm, which forms naturally the limit on the spatial resolution we can achieve. The AFM tip oscillates at a frequency $\Omega \approx 250$ kHz with a tapping amplitude of 80-100 nm, and modulates the scattered optical signal s that is measured with a fast liquid-nitrogen cooled HgCdTe detector (Kolmar Technologies) for mid-infrared light or a closed-cycle helium-cooled Ge:Ga THz detector (QMC Instruments).

2.3. Principle of operation of s-SNOM

Figure Fig. 2.5 illustrates schematically the optical elements that form in essence an s-SNOM system. The light from our source is attenuated to a desirable level with a pair of infrared wire-grid polarizers, then passes through a beamsplitter and hits the parabolic mirror that focusses the vertically polarized light onto the apex of the AFM tip. After interaction with the sample, the light scatters out from the tip, gets collected and collimated by the parabolic mirror, and the beamsplitter directs the light to another parabolic mirror that focusses the light on a detector. As discussed below, a reference arm allows for interferometric detection, which we use to measure the acquired phase difference of light upon scattering in and out of the sample. A pair of polarizers in the reference arm is used to optimize the power reaching the detector from this arm. All polarizers, beamsplitters and windows through which infrared light passes are made of ZnSe, which is transparent from the visible up to 20 µm. A red HeNe laser overlapping with the infrared beams assists in the alignment procedure.

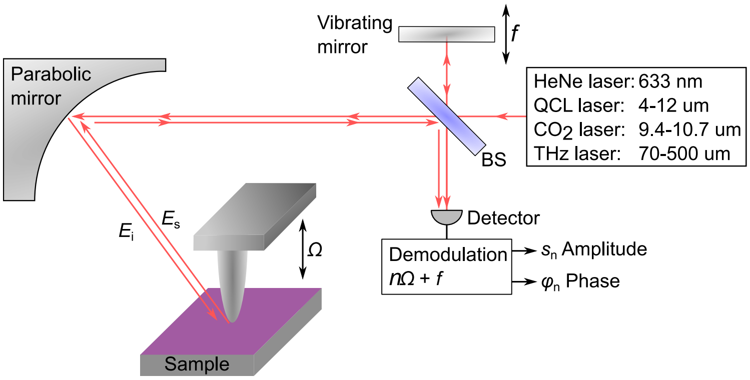

Figure 2.5: Schematic illustration of an s-SNOM system. The interferometric design allows for detecting the amplitude and phase of the near-field signal under the AFM tip. Figure adapted from Ref. 114.

To align this system, we follow a procedure set by the following conditions:

1. The light hits the parabolic mirror parallel to its axis. This is verified by aligning the back-reflected light (using some flat part of the parabolic mirror) on an iris close to the laser source.
2. The light hits the parabolic mirror placed in front of the detector parallel to its axis. We verify this by replacing the parabolic mirror with a flat mirror, aligning the back-reflected light to an iris near the beamsplitter, and placing back the parabolic mirror in the same mount.
3. The apex of the AFM tip sits in the focal point of the parabolic mirror. This is achieved by adjusting the position of the parabolic mirror.
4. The detector sits in the focal point of the parabolic mirror placed in front of the detector. This is achieved by adjusting the position of the detector.
5. The beam from the reference arm interferes at the detector with the out-scattered light. For this, we adjust the angle of the reference mirror.

Key in the operation of an s-SNOM system is to separate the far-field contributions from near-field contributions. To understand the detection scheme that facilitates this, we

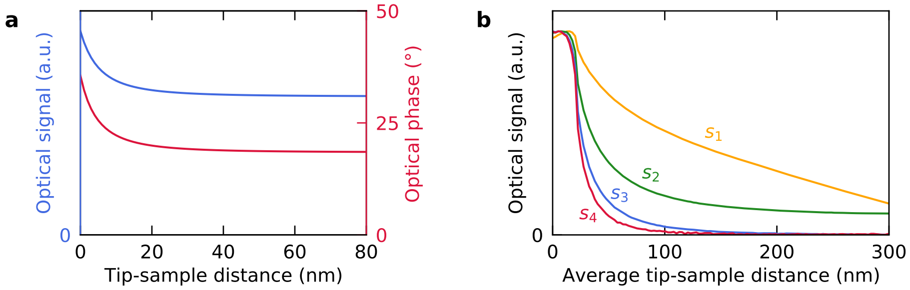

Figure 2.6: Separation of near-field and far-field contributions. **a** The simulated near-field amplitude and phase according to Eq. (2.2) shows a strong enhancement upon bringing the AFM tip close to the sample. For the input permittivities of this calculation, we consider a gold AFM tip and an insulating sample. Figure adapted from Ref. 115. **b** The measured optical signals s_n at different harmonics $n\Omega$ show a strong suppression of unwanted far-field contributions for higher n. These data are provided by Matteo Ceccanti, and taken while approaching the oscillating AFM tip closer to the sample, hence the tip-sample distance is a time-average of the actual position of the cantilever.

model the tip by a point dipole that interacts with a fictive mirror dipole in an homogeneous sample[116]. In this case, the out-scattered electric field E_s is proportional to the incoming field E_i via $\alpha_\mathrm{eff} E_\mathrm{i}$, with

$$\alpha_\mathrm{eff} = \frac{\alpha(1+\beta)}{1-\alpha\beta/(16\pi(a+z)^3))} \tag{2.2}$$

as the effective polarizability of the coupled tip-sample system for tip-sample distance z. Here $\alpha = 4\pi a^3 \frac{\epsilon_\mathrm{t}-1}{\epsilon_\mathrm{t}+2}$ encodes the dielectic permittivity ϵ_t of the tip and its radius of curvature a, while $\beta = \frac{\epsilon_\mathrm{s}-1}{\epsilon_\mathrm{t}+1}$ accounts for the sample permittivity ϵ_s. $\alpha \equiv se^{i\phi}$ is proportional to the detected signal s with phase ϕ. We can benefit from the strong non-linearity of this signal with tip-sample distance, shown in Fig. 2.6a, to separate near- and far-field contributions. By oscillating the tip at frequency Ω, we can convert the modulated optical signal into harmonics $n\Omega$, where each Fourier coefficient $s_n e^{i\phi_n}$ corresponds to the n-th derivative of the optical signal with respect to z[108]. For higher harmonics, this leads to a stronger suppressing of far-field signal. As demonstrated in Fig. 2.6b, by demodulating the optical signal at 3Ω we obtain an almost pure near-field signal free of far-field contributions. Most experimental data shown in this thesis have been acquired at 3Ω, however in some cases 2Ω sufficed. For simplified notation we omit the harmonic where possible such that s and $\Delta\phi$ refer to the measured near-field amplitude and phase difference.

In order to obtain phase-resolved data we use a pseudoheterodyne demodulation scheme[117]. Rather than obtaining the acquired phase difference at each pixel by repeating and post-processing a scan at two different positions of the reference arm, the pseudoheterodyne method does this *in situ*. In this method, the reference arm vibrates at $f \approx 300$ Hz, which is far below Ω. Fig. 2.7 shows the resulting frequency spectrum of the optical signal, wherein the additional modulation generates sidebands at multiples of f at each harmonic of Ω. These sidebands correspond alternately to the real and imaginary part of the complex optical signal, and can easily be converted to s_n and ϕ_n in real time[117].

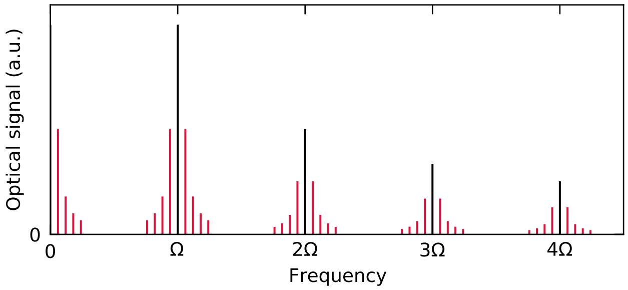

Figure 2.7: Fourier spectrum of the optical signal. The black lines indicate the generated harmonics of the optical signal by oscillating the AFM tip above the sample at frequency Ω. Sidebands at these harmonics are produced by additionally oscillating the reference arm mirror at a much lower frequency, as shown by the red lines. Figure adapted from Ref. 117.

We finally note that it is in general not trivial to relate the measured near-field signal $s_n e^{i\phi_n}$ to the material properties of the sample under study. By using a thin-film inversion model it is feasible to retrieve the local permittivity at the tip position[118–120], however this only works for systems with only one layer on a known substrate. More accurate models have been developed that either treat more carefully the actual response of the AFM tip (rather than a point dipole) or use a machine learning algorithm, yet it only works for simple systems and requires a good guess of the permittivity[121,122]. Fortunately, this does not turn out to be an issue for the projects discussed in this work, as we are mostly interested in the periodicity of spatial variations of the near-field signal, which encode for example the plasmon wavelength.

2.4. Detecting plasmons in graphene using s-SNOM

To illustrate how the system can be used to image collective excitations in van der Waals heterostructures, we discuss a simple example of plasmonic excitations in highly doped single-layer graphene encapsulated in WSe_2. Figure 2.8a plots the near-field phase contrast as function of the tip position in a device fabricated by Karuppasamy Soundarapandian. To be precise, we record the near-field signal while raster-scanning our sample underneath the tip, while maintaining the tip apex positioned in the focal point of the parabolic mirror. The hotspot at the tip interacts with the charge carriers in graphene and produces collective excitations that are reflected by interfaces, return to the tip, and are finally converted into a scattered field, as measured by the infrared photodetector. This leads to oscillations in the near-field signal, as seen in Figure 2.8b. Because plasmons make a round trip, peaks in the near-field signal occur at half the plasmon wavelength, satisfying constructive interference underneath the tip. In addition to these tip-launched plasmons, the graphene edge can also act as a launcher. In that case, the near-field signal underneath the tip is modulated at a spacing equal to the plasmon wavelength. We use the model introduced in Ref. 87 to account for both contributions in the optical signal:

$$s_{\text{opt}}(x) = A\frac{e^{i2qx}}{\sqrt{x}} + B\frac{e^{iqx}}{x^a} + Cx + D \tag{2.3}$$

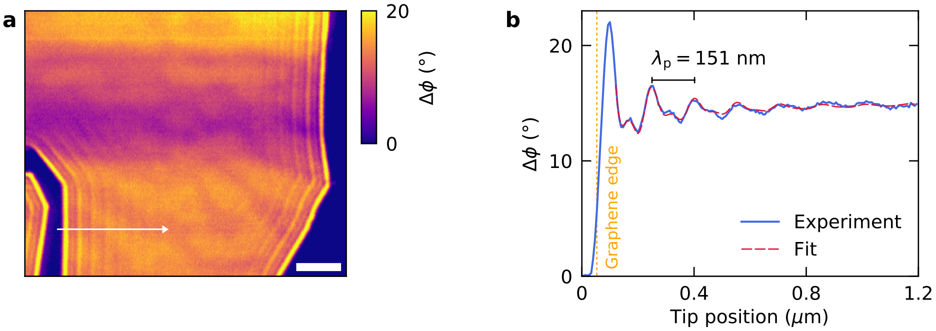

Figure 2.8: Plasmon polaritons in single-layer graphene. **a** Near-field phase contrast of single-layer graphene encapsulated in WSe_2 at a carrier density of $\approx 10^{13}$ cm^{-2}, excitation energy of 117 meV and in ambient conditions. The bright yellow areas correspond a graphene flake, cracked in the bottom left corner. We observe fringes running parallel to the edges of graphene, which decay with distance. The scale bar is 400 nm. **b** Line cut along the white arrow in panel **a**, taken perpendicular to the graphene edge. The oscillations correspond to edge-launched plasmons (λ_p period) and tip-launched plasmons ($\lambda_p/2$ period), both of which we include in the fit according to Eq. (2.3). The dotted orange line corresponds to the edge position of graphene.

with x as the distance from the graphene edge to the tip position, and $q = q_1 + iq_2$ as the complex plasmon wavevector. The first term describes tip-launched plasmons that decay on a scale $\propto 1/q_2$, and takes a geometrical decay factor $\sqrt{x}$ into account. The second term accounts for edge-launched plasmons with a variable decay factor $a \sim 1$. A, B are complex fit parameters, and $Cx + D$ captures any offsets in the signal. From the fit in Figure 2.8b, we can extract $\lambda_p = 2\pi/q_1 = 151$ nm, and a decay length $L_p = 1/q_2 = 550$ nm. This corresponds to an inverse damping ratio $\gamma^{-1} = q_1/q_2 = 2\pi L_p/\lambda_p \approx 23$, serving as a rough indication of propagation damping and is in line with results on hBN-encapsulated graphene[87,112]. This basic analysis has proven to be a powerful tool to gain insight into the fundamental properties of plasmons in graphene-based systems[87,110–112]. We note that throughout this Thesis, the plasmon wavelength λ_p always refers to the inverse of the in-plane wavevector q_1, rather than to the equivalent of the plasmon energy in metals.

2.5. Near-field photocurrent nanoscopy

To study the optoelectronic response of our samples, we employed infrared scanning near-field photocurrent microscopy[93–96]. The technique involves local photoexcitation of carriers using an s-SNOM system combined with an electrical current read out at one of the device contacts. We have to follow a similar demodulation scheme making use of higher harmonics of the cantilever spectrum to extract the near-field components. By measuring near-field photocurrent signals along with the optically scattered light, we obtain a complementary characterization of the local optical response in our samples. We note that in some cases we measure photovoltage, which is linearly related to the photocurrent through the device resistance R as $I_{PC} = V_{PV}/R$. In this way, we can measure the photoresponse between two pairs of contact simultaneously.

The dominating mechanism generating an optoelectronic response in graphene-based devices is the photothermoelectric effect (PTE)[123]. To describe the observed photocurrent features in near-field measurements, we construct a model based on the PTE, in which photocurrent generation proceeds in four steps. First, the electric field generated by the tip induces an oscillating current density in the sample at the excitation frequency ω. Second, this oscillating current causes Joule heating of the electron gas. The power density produced is proportional to the square of the current and has a rectified component $Q(\mathbf{r}, \mathbf{r}_{\text{tip}})$, where $\mathbf{r}$ is the position and $\mathbf{r}_{\text{tip}}$ the position of the tip. Third, the generated heat spreads in the sample on a characteristic length scale referred to as the cooling length[124] (L_{cool}) before being dissipated to the substrate. Finally, since the heat transport is coupled to the charge transport via the Seebeck-Peltier effect, the heat flux is able to generate a net electric current in the presence of Seebeck coefficient gradients. The current and heat flux are governed (at least for small incident power) by a set of linear equations with respect to the source term $Q(\mathbf{r}, \mathbf{r}_{\text{tip}})$. As a consequence, the PTE-induced photovoltage $V_{\text{PTE}}^{(m)}$ at the contact m, with respect to a grounded contact used as a common reference, is then given by a linear relation of the type

$$V_{\text{PTE}}^{(m)} = \int d\mathbf{r} \mathcal{R}_{\text{PTE}}^{(m)}(\mathbf{r}) Q(\mathbf{r}, \mathbf{r}_{\text{tip}}), \tag{2.4}$$

where $\mathcal{R}_{\text{PTE}}^{(m)}(\mathbf{r})$ is the photovoltage responsivity function that encodes the PTE response of the system (details in Appendix B.3). An analogous formula holds for photocurrents. In absence of strong resonant features, for example plasmonic excitations, the response of the system at the energy $\hbar\omega$, given by $Q(\mathbf{r}, \mathbf{r}_{\text{tip}})$, rapidly decays with $|\mathbf{r} - \mathbf{r}_{\text{tip}}|$. This means that $V_{\text{PTE}}^{(m)} \propto \mathcal{R}_{\text{PTE}}^{(m)}(\mathbf{r})$ and the photovoltage (or photocurrent) maps are essentially measuring the responsivity (apart from the convolution with a spread function due to the finite tip dimension).

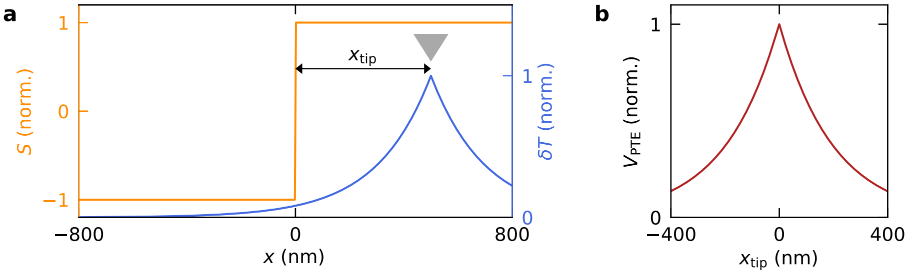

Figure 2.9: Simulated photovoltage for a pn-junction in a 1D channel. **a** In orange: profile of the Seebeck coefficient for a pn-junction in graphene, which we use as input for our simulation. In blue: enhancement of the electron gas temperature due to light coupling in at the tip position x_{tip} (measured relative to the pn-junction), marked by the silver triangle. Heat spreads with a characteristic cooling length L_{cool}. **b** Calculated photoresponse when scanning the tip across the junction, showing a sharp peak in the photovoltage at the junction's interface.

To gain some intuition into the origin of the spatial profile of the photoresponse generated in our devices, we consider the form of the photovoltage responsivity function for a one-dimensional device (derivation in Supplementary Note 5 of Ref. 125). This reads

$$\mathcal{R}(x) = -\frac{1}{\kappa W}\int \mathrm{d}x' \frac{L_{\mathrm{cool}}}{2} e^{-\frac{|x'-x|}{L_{\mathrm{cool}}}} \partial_x S(x'), \tag{2.5}$$

where W is the width of the device and κ its electronic thermal conductivity. In this example (in open-circuit configuration), an infinitely sharp tip creates a spatial profile of electron temperature (Fig. 2.9a) in the form $\delta T(x) \equiv T(x) - T_0 \propto e^{-|x'-x|/L_{\mathrm{cool}}}$, with T_0 being the temperature of the substrate. From Eq. 2.5 we see that the PTE requires an inhomogeneous Seebeck coefficient with a gradient parallel to the path between measurement contacts (Fig. 4.6 provides an example of this directional sensitivity). In addition to that, the responsivity decays away from the Seebeck coefficient S fluctuations on a length scale L_{cool}, since that is the distance that heat is able to travel in the sample. To illustrate this, Figure 2.9 plots the calculated photovoltage across a pn-junction. For such configuration, the step in S at the junction causes a peak in the photovoltage. We finally note that in a system with particle-hole symmetry, $\mathcal{R}_{\mathrm{PTE}}(x)$ is an odd function of the electronic density because $S(x)$ is odd. This behaviour is typically observed in the gate-voltage dependence of the measured photoresponse, where the photoresponse changes sign around the Dirac point due to a change in sign of the carriers' charge.

In our experiments, the measured photocurrent/voltage signal is demodulated with the driving signal of the AFM cantilever as reference signal. However, the actual motion of the AFM cantilever can have a phase offset that varies with the position on the sample (due to tip-sample interaction). This phase offset is given at each pixel by the measured phase delay between the tip-driving signal and the actually detected motion. To correct our photocurrent/voltage signal measured at harmonic n, we subtract at every point n times this phase delay. In addition to this, there remains a global phase offset in the corrected photocurrent/voltage signal due to the electronics in the circuit. Since the

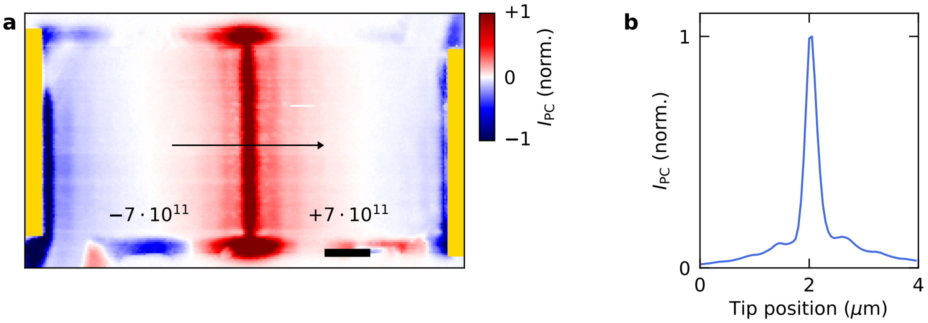

Figure 2.10: Photocurrent nanoscopy on a double-gated graphene device. a Photocurrent map of a graphene device with the left and right side oppositely doped via a metal split-gate (carrier density in units of cm^{-2}). The bright vertical stripes of negative photocurrent are generated by the junction formed at the contacts (marked in gold), while a strong positive photocurrent is produced at the pn-junction in the middle. The vertical fringes running parallel to the pn-junction are acoustic plasmons launched by the sharp edges of the gate electrodes[126]. The excitation energy is 13 meV (3.11 THz) and the scale bar is 1 µm. **b** Line cut along the black arrow in panel **a**. The peak in photocurrent corresponds to the position of the pn-junction. We observe acoustic plasmons near this peak as oscillations on top of the decaying photocurrent signal.

photocurrent/voltage signal is a real-valued quantity, we subtract this global phase offset, which we determine by taking the most frequent phase within a scan.

Figure 2.10 shows an example of a near-field photocurrent map recorded in a graphene device made by Yuanda Gao (device details in Ref. 127). By oppositely tuning the voltages of the two local gates, we create a pn-junction in the middle of the device, which we observe as a bright peak in the photocurrent. It additionally demonstrates that photocurrent nanoscopy can be used to visualize collective excitations[94,95,126], shown here as the fringes running parallel to the junction and corresponding to acoustic plasmons in graphene.

3. Observation of interband collective excitations in twisted bilayer graphene

The single-particle and many-body properties of twisted bilayer graphene (TBG) are strongly influenced by the moiré potential induced by the twist angle between the layers, in particular when the two layers are rotated relative to each other by a small angle near the 'magic angle' $\theta \approx 1.1^\circ$*. In this Chapter, we probe collective excitations of TBG and find a propagating plasmon mode in charge-neutral TBG with* $\theta = 1.1 - 1.7^\circ$*, which is different from the intraband plasmon in single-layer graphene. We interpret it as an interband plasmon associated with the optical transitions between minibands originating from the moiré superlattice. The details of the plasmon dispersion are directly related to the motion of electrons in the moiré superlattice and offer an insight into the physical properties of TBG, such as the band nesting between flat band and remote band, local interlayer coupling and losses. We find a strongly reduced interlayer coupling in the regions with AA-stacking, pointing at screening due to electron-electron interactions.*

3.1. Optical properties of TBG: host of interband plasmons

As introduced in Chapter 1, the band structure of twisted bilayer graphene is interesting from the perspective of optics. Strong band nesting between the nearly flat bands and the nearest conduction and valence bands causes a high joint density of states for the relevant interband transitions[72,128], especially close to the K point. For the twist angle close to the magic angle the energy separation between these bands is ~ 100 meV. This justifies our interest in the optical properties and collective excitations[91,129], as probed by s-SNOM (Fig. 3.1a-c), in the mid-infrared region of the electromagnetic spectrum where photons have energies $\hbar\omega$ in the range $80 - 200$ meV, which is comparable to the above-mentioned energy scale. On the other hand, these energies are much larger than the energy separation between the pair of nearly-flat bands, considered in Ref. 90.

We can qualitatively understand the optical properties of this system in the following way. When light impinges on TBG, its time-periodic electric field shakes electrons around their equilibrium positions (the AA sites, forming a triangular lattice) or — in the more rigorous language of band theory — it induces an interband transition between the ground and excited states at the K point of the superlattice Brillouin zone (Fig. 3.1d-e). If the field carries a finite in-plane wavevector q (provided by the sharp AFM tip), the shaking electrons will build up an oscillating charge density with the same wavevector (plus harmonics due to exchange of reciprocal lattice vectors). This oscillating charge density, in turn, creates an oscillating electric field that adds to the external field. If q and ω are correctly matched, this induced field can be strong enough to sustain the oscillation even after the external field has been turned off. This resonant behaviour gives rise to collective modes that are called interband plasmons, which have been predicted theoretically to emerge in TBG[89,91], but were never studied experimentally so far. At $q = 0$, this collective excitation has the same frequency as the bare interband transition. Upon increasing q, as we show in this work, it acquires a finite dispersion. Thus, these excitations do propagate with a finite group velocity, akin to graphene Dirac plasmons[85,86,130], albeit with very different dispersion. Here, the dispersion depends on the degree of band nesting, which is the phenomenon of two bands being parallel in energy-wavevector space, and details of the e-e interaction potential, which is heavily influenced by screening from nearby dielectrics. We note that a similar collective mode occurs in topological insulators[131,132] or between the rigorously flat Landau-levels of a two-dimensional (2D) parabolic-band electron gas in a perpendicular magnetic field. In this case, while single electrons oscillate at the cyclotron frequency Ω_c, e-e interactions induce a collective mode, known as a bulk magnetoplasmon, which, at long wavelength, has a linear dispersion[133] $\omega(q) = \Omega_c + sq$ with group velocity $s > 0$ reflecting its propagating character.

3.2. Near-field measurements of interband plasmons

The TBG samples for this study were made by Daniel Rodan and Yuan Cao from the MIT group using the tear-and-stack method (Sec. 2.1 provides details). These are encapsulated in hBN, and placed on a metal gate (Table S1 in Ref. 134 provides a list of the studied devices). The twist angle θ is determined at MIT from cryogenic transport measurements[15], as shown in Appendix A.1.

Here, we perform s-SNOM measurements with mid-infrared light (free-space wavelength λ_0 in the range $5 - 11$ µm) in ambient conditions ($T = 300$ K). In brief, we generate a nanoscale light hotspot by focussing a laser beam on the apex of a sharp (apex radius ≈ 25 nm) metallic atomic force microscope (AFM) tip (Fig. 3.1a). This hotspot interacts with the charge carriers and produces collective excitations that are reflected by interfaces, return to the tip, and are finally converted into a scattered field, which is measured by a photodetector. By scanning the tip position, we acquire, simultaneously, a spatial map of the backscattered light intensity s and AFM topography. Noise and far-field contributions to the optical signal are strongly reduced by locking to the third harmonic of the tapping frequency of the tip. The spatial resolution of the obtained images is limited only by the tip radius, as discussed in Section 2.2.

Figure 3.1b shows a typical near-field image of TBG with no gate voltage applied (at zero applied voltage the TBG is close to charge neutrality, see Appendix A.1 and Table S1 in Ref. 134) and an average twist angle of $\theta = 1.35°$, obtained from the transport measurements. Figure 3.1c shows the AFM image recorded at the same time. In the near-field image, for an excitation energy $\hbar\omega = 219$ meV two types or regions can be distinguished. Regions with a rather spatially constant response s (yellow) and regions where s shows clear spatially varying and periodic features. This contrasts with a near-field map taken at lower energy $\hbar\omega = 146$ meV, in which the periodic features are absent (Fig. 3.2e). As reported scanning SQUID measurements on similar samples have shown[48], some regions can exhibit magic-angle behaviour while some other regions do not (for instance, due to lattice relaxation into an angle far from magic angle). In this work, we focus on the regions with the varying and periodic features of this device. Table S1 in Ref. 134 and Appendix A.2 provide results from 14 other devices with $\theta = 1.1 - 1.7°$ and a discussion on the correlation of these regions with tiny topographic features.

In the regions of interest, s displays an oscillatory spatial behaviour. The latter has a characteristic period ≈ 80 nm in all of the regions of interest (with a ± 10 nm spread), about one order of magnitude larger than d. We attribute this oscillatory behaviour to the excitation of a propagating collective electronic mode. The fact that we observe these interference patterns in ungated TBG is in stark contrast with the intraband collective electronic excitations (Dirac plasmons) of single-layer and bilayer graphene, where high doping levels (above 10^{13} cm^{-2}) are required to propagate at the frequencies we focus on ($\hbar\omega = 200$ meV)[78,87,130].

To gain insight into the nature of the collective excitations we probe their frequency dependence by repeating the near-field measurements at different excitation energies, changing $\lambda_0 = 2\pi c/\omega$. Figure 3.2a-e shows a dramatic change in the interference pattern for small variations in λ_0, while the boundaries of the areas where the sample is optically active remain at a fixed position. These data show the dispersive character of the propagating collective excitations that move in Fabry-Pérot-like cavities, due to reflecting interfaces[41,135,136]. At the same time, the scan in Fig. 3.2f for $\hbar\omega = 170$ meV is free of any features. As $\hbar\omega$ coincides with the lower edge of the Reststrahlen band of hBN, the near-field signal is dominated by the top hBN layer. Thus, we conclude that the observed features in Fig. 3.2a-e originate from the TBG itself. If any contamination was present on top of the sample, or if the hBN would exhibit thickness variations, the 170 meV scan would not show such a uniform response as we observe.

More quantitatively, we extract one-dimensional (1D) cuts of the measured s along two specific lines (arrows in Fig. 3.2d). The resulting 1D profiles are shown in Fig. 3.2g as

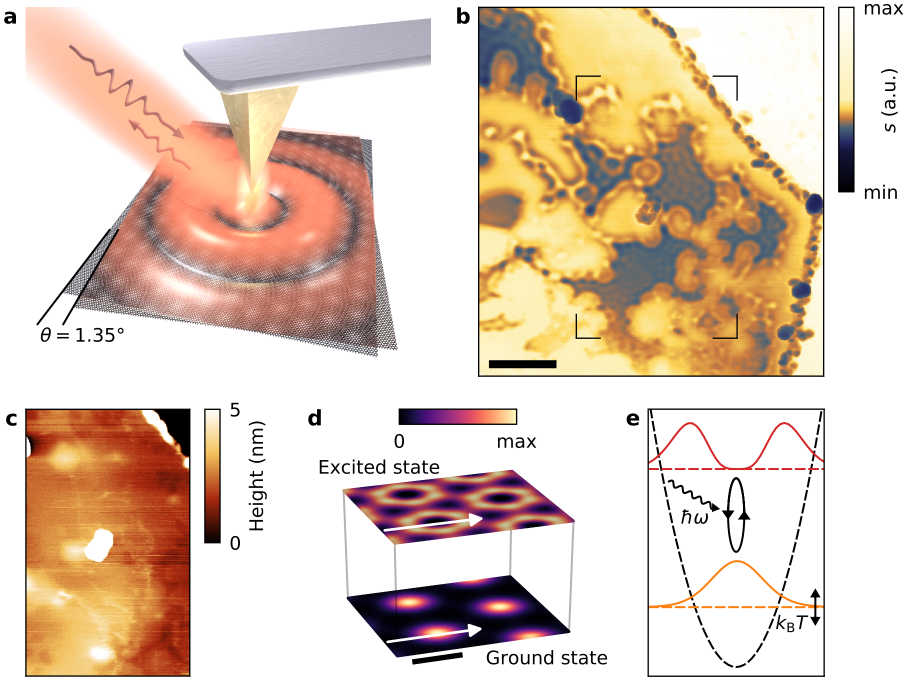

Figure 3.1: Collective excitations in twisted bilayer graphene. **a** Illustration of the s-SNOM experiment: an AFM metallic tip is illuminated by infrared light, which provides sufficient momentum to launch a collective excitation in twisted bilayer graphene. The plasmon can, in turn (for instance, by reflection from an edge or interface), scatter into light at the tip. This scattered light is detected by a photodetector. Credit: Fabien Vialla. **b** Image of the near-field amplitude obtained by scanning the AFM tip and recording the photodetector signal. Propagating collective excitations are visible in certain areas as periodic interference fringes. The illumination photon energy is $\hbar\omega = 219$ meV and the scale bar is 500 nm. **c** AFM image of the marked region in panel **b**. **d** Square modulus of the wave function $|\langle \mathbf{r}|\mathbf{k} = K, \nu\rangle|^2$, associated with one of the flat bands (bottom) and the first excited band (top), evaluated at the K point of the moiré superlattice Brillouin zone. These states are mostly localized around the regions with local AA-stacking (which form a triangular lattice) and are involved in the relevant optical transitions. **e** Line cuts of the wave functions along the white arrows in panel **c** represented in a harmonic confinement potential[35] (black dashed line), with the coloured horizontal dashed lines indicating the energies of the states. An interband transition occurs between the lower-energy state and the excited state. A similar transition is happening, for holes, between the corresponding pair of states, approximately related to the illustrated ones by electron-hole symmetry.

lines for a few representative photon energies, while a colour map as a function of tip position and frequency is reported in Fig. 3.3a (see Supplementary Note 5 in Ref. 134 for other line traces taken in the near-field image). The oscillating signal is well fitted by the following expression, representing a tip-launched, tip-detected wave reflected at an interface: $s_{\text{opt}}(x) = \text{Re}(Ax^{-1/2}e^{2iq}) + Bx$. Here, x is the tip position along the line cut, as measured from the interface, $A \equiv A_1 + iA_2$ and $q \equiv q_1 + iq_2$ are complex fit parameters, and B represents a linear background (Sec. 2.4). Note the factor of two in the exponential

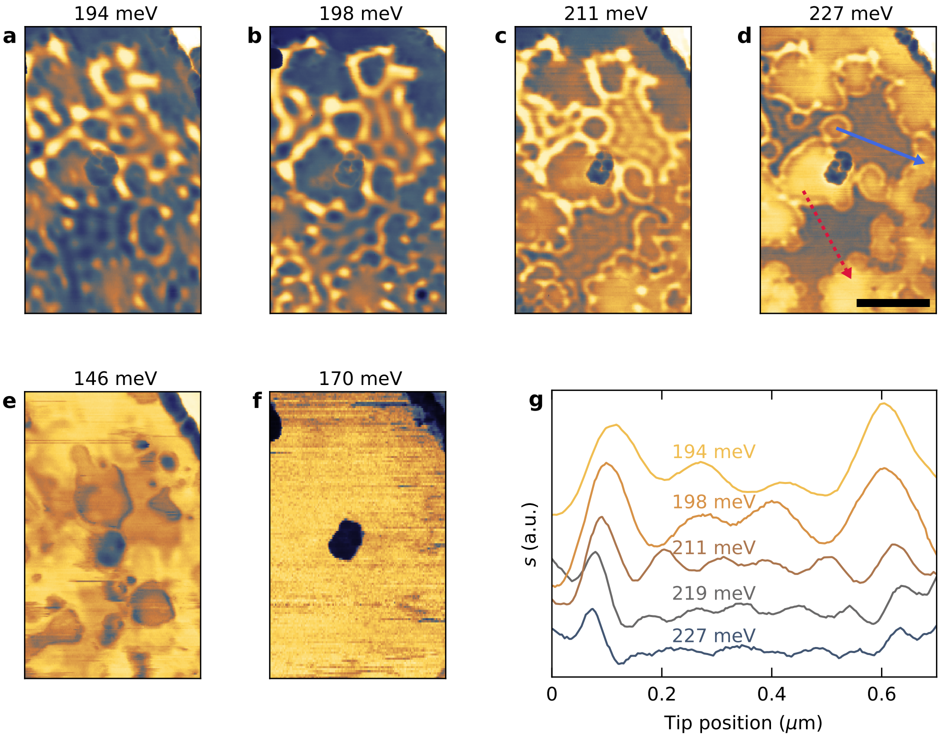

Figure 3.2: Controlling the wavelength of interband plasmons. **a**-**f** Images of the near-field amplitude at different excitation energies E of the area marked in Fig. 3.1**b**. In panels **a**-**d** $\hbar\omega > \hbar\Omega_{\text{exp}}$, while the data in panels **e**,**f** correspond to $\hbar\omega < \hbar\Omega_{\text{exp}}$. The colour scale is the same as in Fig. 3.1**b**. Solid and dashed arrows in panel **d** indicate line traces associated to data in panel **g** and Fig. 3.3**a**, and the scale bar is 500 nm. **g** Line traces along the solid blue arrow in panel **d**, visualizing the strong dependence of the plasmon wavelength on the excitation energy. Lines are vertically separated for clarity.

function that appears because the collective excitation makes a full round trip between the tip and the reflecting interface. Our fitting procedure yields quantitative results for the real part q_1 of the plasmon wavevector q while the imaginary part q_2 is notably smaller (Supplementary Note 5 in Ref. 134 provides further details). We find the inverse damping ratio $\gamma^{-1} = q_1/q_2$ (introduced in Sec. 2.4) to be typically between $20 - 50$, with a lower bound of $\gamma^{-1} = 5$. This is similar to the value found in single-layer graphene[87], $\gamma^{-1} = 25$.

From the extracted values of $q_1(\omega)$ we can construct a dispersion curve for the collective excitation as shown in Fig. 3.3b. For energies above 200 meV, the dispersion is approximatively linear with a group velocity $v_g \approx 0.9 - 1.3 \cdot 10^6$ m/s (dashed and dotted lines in Fig. 3.3b), and crosses the $q_1 = 0$ point for $\hbar\Omega_{\text{exp}} \approx 190$ meV. For lower energies, the typical discretization pattern of a finite size cavity appears (that is, where the distance between the reflecting interfaces is comparable to the plasmon wavelength $2\pi/q_1$). Remarkably, the group velocity is larger than theoretically anticipated, see for instance Ref. 89, where flat plasmonic bands were predicted, and the discussion below. As we will see, this points to a larger spectral weight in the optical transitions. Clearly, the observed

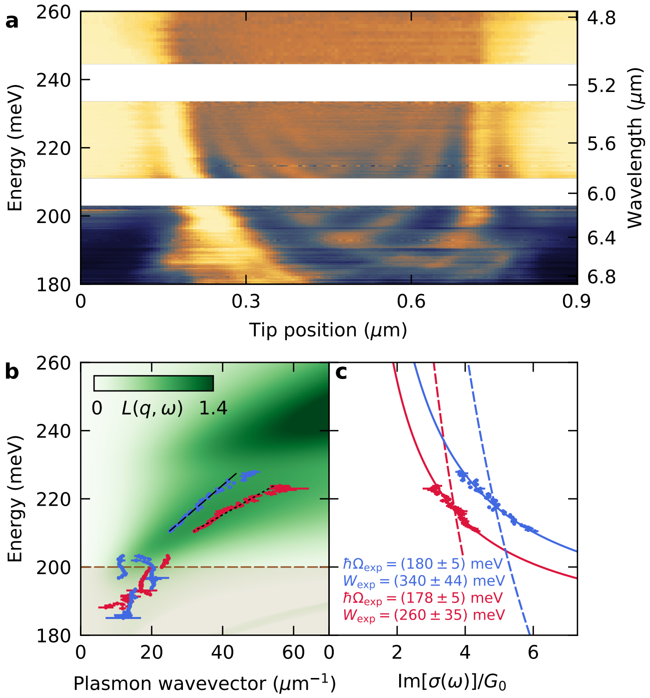

Figure 3.3: Extracting the optical conductivity from the plasmon dispersion. a Near-field amplitude along the dashed red arrow in Fig. 3.2**d**, for a range of excitation energies. The colour scale is the same as in Fig. 3.1**b** and to highlight the plasmonic modes, we normalize each line to the average near-field amplitude within the reflecting interfaces. The white gaps are gaps in the spectrum of the excitation laser. **b** Dispersion relation $q_1(\omega)$ determined from fitting individual line traces in panel **a** to a sinusoidal function (red points). The blue points are obtained in a similar way but from a slightly different location (solid blue arrow in Fig. 3.2**d**). We extract the plasmon group velocity (black dashed/dotted lines) from a linear fit on the blue data points. The horizontal dashed line marks the threshold of the Reststrahlen band of hBN. The colour plot represents the loss function calculated from the chirally-symmetric continuum model[37], and gives a rough estimate of the inverse damping ratio of the modes. **c** Extracted values of the optical conductivity with the same colour coding as in panel **b**. Dots represent experimental data, dashed lines are Drude fits, while solid lines are fits with resonant profiles.

nearly-linear dispersion, initiating from a finite energy $\hbar\Omega_{\text{exp}}$ for $q_1 = 0$, is very different from the typical Dirac plasmon dispersion of doped single- and bilayer graphene, as we discuss in Sec. 3.4. Instead, the observed linear dispersion resembles more the one of a bulk magnetoplasmon[133]: $\omega(q) = \Omega_{\text{exp}} + v_g q_1$.

3.3. Extraction of the optical conductivity

To relate our observations to the electronic bands in the moiré superlattice, we extract the value of the optical conductivity $\sigma(\omega)$ for the optically active regions. In the local approximation[137] (that is, where the optical conductivity is taken to be independent of q and contributions from reciprocal lattice vectors $G \neq 0$ are neglected), the longitudinal dielectric function[138] is given by $\epsilon(q,\omega) = 1 + iq^2 V_{q,\omega}\sigma(\omega)/\omega$, where $V_{q,\omega} = 2\pi F(q,\omega)/[\tilde{\epsilon}(\omega)q]$ is the 2D Fourier transform of the Coulomb potential[126], the permittivity $\tilde{\epsilon}(\omega) = \sqrt{\epsilon_{\|}(\omega)\epsilon_{\perp}(\omega)}$ takes care of the optical response at frequency ω of the hBN crystal slabs[139] surrounding the TBG sample, and $F(q,\omega)$ is a form factor that takes into account the finite thickness of the hBN slabs (Appendix A.3). Finite-thickness effects are important close to the upper edge of the Reststrahlen band of hBN where the in-plane permittivity $\epsilon_{\|}(\omega)$ vanishes and the out-of-plane decay length of the mode diverges. Neglecting the finite thickness of hBN would lead to a wrong dispersion relation, yielding a collective mode that does not enter the upper Reststrahlen band (Fig. 3.3b). Collective modes can be found by solving[138] $\epsilon(q,\omega) = 0$, or by looking at the peaks of the loss function $L(q,\omega) = -\mathrm{Im}(\frac{1}{\epsilon(q,\omega)})$. From the measured collective excitation dispersion, we can find the imaginary part $\sigma_2(\omega)$ of the local conductivity, using the expression $\sigma(\omega) = i\omega/(q^2 V_{q,\omega})$ and neglecting the imaginary part of q (Appendix A.3 shows that we can safely do this without changing the results). The results are shown in Fig. 3.3c.

The simplest possible fitting function, of the Drude form $\sigma_2(\omega) = G_0 W_0/\hbar\omega$ — where $G_0 = 2e^2/h$ is the conductance quantum and W_0 is a fitting parameter with dimensions of energy — yields $W_0 \approx 1100$ meV (that would correspond, for two uncoupled single-layer graphene sheets, to a Fermi energy $E_{\mathrm{F}} \approx 550$ meV in each layer) and a very poor fit. This confirms that our data are not consistent with a regular intraband graphene Dirac plasmon. A much better fit is obtained by using the following resonant form: $\sigma_2(\omega) = G_0 W_{\mathrm{exp}} \frac{\hbar\omega}{\hbar^2\omega^2 - \hbar^2\Omega_{\mathrm{exp}}^2}$, with W_{exp} and Ω_{exp} as fitting parameters. We find $\hbar\Omega_{\mathrm{exp}} \approx 180$ meV and a spectral weight $W_{\mathrm{exp}} \approx 300$ meV for both presented datasets. Supplementary Note 9 in Ref. 134 further discusses the influence of a Drude response in this analysis.

3.4. Comparison between plasmons in TBG and single- and bilayer graphene

Single-layer graphene (SLG), as well as Bernal-stacked bilayer graphene (BG), can display plasmonic excitations[87], though there are key differences with the observations made here for TBG. To make a comparison, we calculate the loss function $L(q,\omega)$ as introduced in the previous Section for the three systems. For SLG we use the local, frequency-dependent conductivity taken from Ref. 140, while we calculate the local, frequency-dependent conductivity of BG using the Kubo formula from its band structure (Appendix B.4 with $d_y = 1$), taking into account the non-zero displacement field. For the conductivity of TBG we employ the chirally-symmetric continuum model as will be introduced in Sec. 3.6. We perform all calculations with $T = 300$ K and consider the finite-thickness effect of hBN. The simulated device structure consists of a metal gate, 47 nm bottom hBN, followed by SLG, BG or TBG, and 13 nm top hBN. Figure 3.4 displays the results.

We find that only highly doped SLG and BG can host intraband plasmonic excitations with a dispersion qualitatively (but not quantitatively) similar to what we have found (Fig. 3.4b-c). For SLG we considered a Fermi level $E_{\mathrm{F}} = 0.5$ eV, which can be reached via electrostatic gating only at the breakdown voltage of hBN (~ 1 V/nm). The fact that we observe the collective excitations in ungated (thus nearly charge-neutral) TBG marks a strong difference from SLG and BG. Besides interband plasmons, TBG is also predicted to hosts intraband excitations, as seen for energies below 30 meV in Fig 3.4d. However,

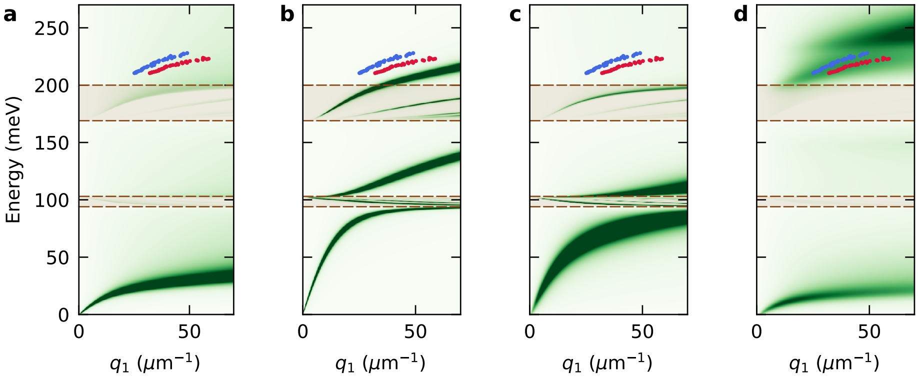

Figure 3.4: Comparison of calculated loss function for SLG, BG and TBG. **a** The loss function of SLG at $E_F = 0$ eV. The strong excitations at low energies are intraband plasmons at THz-frequencies resulting from thermally excited carriers[126]. The data points are the same as those in Fig. 3.3**b**. The brown dashed areas indicate the lower and upper Reststrahlen bands of hBN. **b** Same as in panel **a** but for $E_F = 0.5$ eV, corresponding to a doping level of $1.85 \cdot 10^{13}$ cm^{-2}. The plasmonic mode hybridizes with hBN phonons, as seen by the crossing near 100 meV. **c** The loss function of BG for $E_F = 0.2$ eV, corresponding to a doping level of $1.62 \cdot 10^{13}$ cm^{-2}. **d** The loss function of TBG as calculated from the chirally-symmetric continuum model[37] for $\theta = 1.35°$. The mode for $\hbar\omega < 30$ meV corresponds to an intraband plasmon, while the interband excitations are reflected by the modes at $\hbar\omega > 200$ meV. The colour scale is for all panels the same as Fig. 3.3**b**.

we have not been able to detect such modes in our experiment.

Furthermore, the typical SLG and BG plasmons are predominantly observed near edges of the device or particular defects within the samples[41,135,136]. The observation of enclosed patches of optical activity in TBG, formed by reflecting interfaces possibly linked to local strain and twist-angle variations (Appendix A.2), is something not seen in SLG.

3.5. Interband plasmons in gated twisted bilayer graphene

Finally, we measure on one of our devices the carrier-density dependence of the dispersion of the collective excitation by applying a voltage bias between the TBG and the metallic gate. To this end, we conduct measurements in a cryogenic near-field microscope (Chapter 6), allowing us to perform near-field imaging and measurements of the global transport properties at the same time.

Figure 3.5a shows a near-field image of another TBG device at finite doping, recorded at a temperature of about 10 K. It exhibits one region with an oscillatory pattern inside, which we interpret as interband plasmons due to the strong similarity with the collective excitations discussed above. As discussed in Supplementary Note 7 in Ref. 134, we do not observe a change of the collective excitations with temperature. To study the effect of doping, we first measure the two-probe resistance of this TBG device (Fig. 3.5b) as a function of gate voltage V_G. Two distinct peaks in the resistance away from the CNP correspond to the full-filling states of two different regions at $\theta \approx 1.1°$ and $\theta \approx 1.3°$

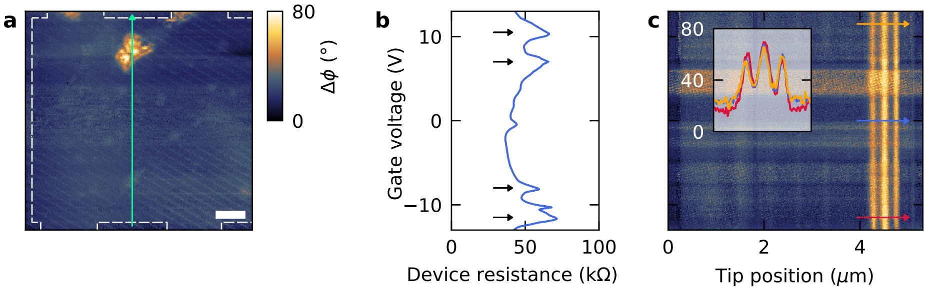

Figure 3.5: Interband plasmons in a gated device. **a** Near-field image of the scattering phase in a different TBG device, measured at $V_G = -9$ V. The red square marks a region exhibiting collective excitations. **b** Two-probe device resistance between the bottom two leads as function of gate voltage. The four marked peaks in the resistance correspond to full-filling states at two different twist angles within the device, and the resistance peak near 0 V marks the CNP. The y-axis is shared with panel **c**. **c** Near-field scattering phase along the green arrow in panel **a** for a range of gate voltages. Three line traces at different voltages show that there is no substantial change in the collective excitations upon gating the device. The sample temperature in all measurements shown here is 10 K and the excitation energy is 134 meV.

(Eq. (A.1)), providing a rough indication of the twist angle in the region with collective excitations.

We now take a line cut through the middle of the device, crossing the region with collective excitations, and vary the gate voltage while recording the near-field phase signal (Fig. 3.5c). From this measurement, we see that there is no substantial change in either the recorded periodicity or near-field phase signal of the collective excitations upon doping the device beyond its full-filling state. As discussed in Appendix A.4, our calculations only show minor changes in the loss function upon filling of the bands until $\nu \approx 1.5$. These data strengthen the interpretation in terms of collective modes originating from an interband transition, as those are much less affected by the carrier density than intraband plasmons (Sec. 3.4).

3.6. Theoretical model for interband transitions in TBG

We now seek a theoretical justification for the resonant lineshape (Fig. 3.3) extracted from the experimental data and for the values we have found for Ω_{exp} and W_{exp}. This is in large part developed by Iacopo Torre, Pietro Novelli and Marco Polini. At the level of the random phase approximation (RPA) for the dynamical dielectric function[138] $\epsilon(q,\omega)$, the unknown quantity $\sigma(\omega)$ is approximated by using its value for the non-interacting 2D electron system in TBG. We note that $\sigma_{\text{xx}} = \sigma_{\text{yy}} = \sigma$, since the system has three-fold rotational symmetry. The latter can be calculated exactly by employing the Kubo formula[138], once the eigenstates $|\mathbf{k},\nu\rangle$ and bands $\epsilon_{\mathbf{k},\nu}$ of the single-particle problem are given. Here $\mathbf{k}$ represents the electronic wavevector. The quantities $|\mathbf{k},\nu\rangle$ and $\epsilon_{\mathbf{k},\nu}$ can be found from a band structure calculation for TBG at a given θ. Here, we have used results obtained from *ab initio* $\mathbf{k}\cdot\mathbf{p}$ perturbation theory[141], which accurately accounts for the effects of intrinsic atomic relaxation in pristine samples. The resulting bands $\epsilon_{\mathbf{k},\nu}$

are shown in Fig. 3.6a. We clearly see that band nesting occurs near the K point of the superlattice Brillouin zone, where two (relatively flat) bands — say ν and ν', connected by vertical lines with arrows in Fig. 3.6a — are such that $\nabla_{\mathbf{k}}\epsilon_{\mathbf{k},\nu} \simeq \nabla_{\mathbf{k}}\epsilon_{\mathbf{k},\nu'}$ in a range of values of $\mathbf{k}$. In other words, the bands are parallel to each other for a wide range of $\mathbf{k}$. The joint density of states for these pairs of bands is large at the transition frequency and the resultant optical absorption spectrum $\sigma_1(\omega) \equiv \mathrm{Re}[\sigma(\omega)]$ has a peak at a nearby frequency Ω_{th} as shown in Fig. 3.6b. At the CNP, $\theta = 1.35°$, and $T = 300$ K (used for all calculations in this work), we find $\hbar\Omega_{\mathrm{th}} \approx 115$ meV and an associated spectral weight $W_{\mathrm{th}} \equiv 2\hbar \int_{\mathrm{peak}} d\omega \frac{\sigma_1(\omega)}{\pi G_0} \approx 64$ meV. Because of causality, $\sigma_1(\omega)$ and $\sigma_2(\omega)$ are related by a Kramers-Kronig transform[138]. The resonant lineshape introduced above for $\sigma_2(\omega)$ yields $\sigma_1(\omega) = \pi G_0 W_{\mathrm{exp}}[\delta(\hbar\omega - \hbar\Omega_{\mathrm{exp}}) + \delta(\hbar\omega + \hbar\Omega_{\mathrm{exp}})]/2$. This implies that our simple resonant fitting formula for $\sigma_2(\omega)$ represents the peak seen in the microscopically calculated $\sigma_1(\omega)$ at Ω_{th} — see Fig. 3.6b — with a delta peak at Ω_{exp} with spectral weight W_{exp}.

While Ω_{th} is in a reasonable agreement with Ω_{exp}, there is notable disagreement with the spectral weight since $W_{\mathrm{th}} \ll W_{\mathrm{exp}}$. The sources of this spectral weight mismatch can be multiple. To gain understanding, we resort to a more flexible continuum band-structure model[38]. This contains two parameters, u_0 and u_1, denoting the interlayer coupling in the AA regions and AB/BA regions, respectively. Results based on such continuum model with the choice[38] $u_0 = 79.7$ meV and $u_1 = 97.5$ meV present only minor quantitative differences with respect to those of *ab initio* $\mathbf{k}\cdot\mathbf{p}$ perturbation theory shown in Fig. 3.6b and are reported in Supplementary Note 10 in Ref. 134. Also, calculations in Ref. 89 give qualitatively similar results. The same continuum model with $u_0 = 0$ and $u_1 \neq 0$, which is endowed with unitary particle-hole symmetry, has been introduced in Ref. 37 as an idealization of reality.

Intriguingly, we find that the conductivity calculated from this chirally-symmetric continuum model (CS-CM)[37] — for $u_0 = 0$ and $u_1 = 97.5$ meV — displays a much better agreement with our experimental data. The bands $\epsilon_{\mathbf{k},\nu}$ of the CS-CM are shown in Fig. 3.6c, while the optical absorption spectrum is reported in Fig. 3.6d. Also here, σ_2 displays a resonant profile, but the resonant energy is $\hbar\Omega_{\mathrm{th}} \approx 199$ meV and the spectral weight is $W_{\mathrm{th}} \approx 162$ meV, in much better agreement with our experimental results. The loss function, calculated from this CS-CM is shown in Fig. 3.3b and overlaps very well with the superimposed experimental data. This suggests that the optical spectral weight is strongly enhanced in the optically active regions and this enhancement can be explained by an effective suppression of the AA interlayer coupling in the same regions. Appendix A.4 provides additional calculations for different twist angles.

Motivated by this finding, we perform a systematic scan of the AA tunnelling amplitude in a range going from $u_0 = 0$ meV — corresponding to the CS-CM — to $u_0 = 79.7$ meV, which is the value given in Ref. 38. For each value of u_0 we calculate the band structure, extract the optical conductivity, and fit it with a resonant profile to extract the parameters $\hbar\Omega_{\mathrm{th}}$ and W_{th}. The results are shown in Fig. 3.7. The resonant frequency increases monotonically with decreasing u_0 and crosses the experimentally measured value around $u_0 \approx 40$ meV. The spectral weight has instead a non-monotonic behaviour but gets closest to the experimental data approximately in the range $20 < u_0 < 40$ meV. We performed the same procedure on the *ab initio* $\mathbf{k}\cdot\mathbf{p}$ perturbation theory model by scaling the parameters corresponding to the AA tunnelling. The results are qualitatively similar, apart from a rigid shift, as shown in Fig. 3.7. The rigid shift is primarily caused by a small difference between the models' effective AB coupling u_1. This can also be viewed as a tunable parameter of

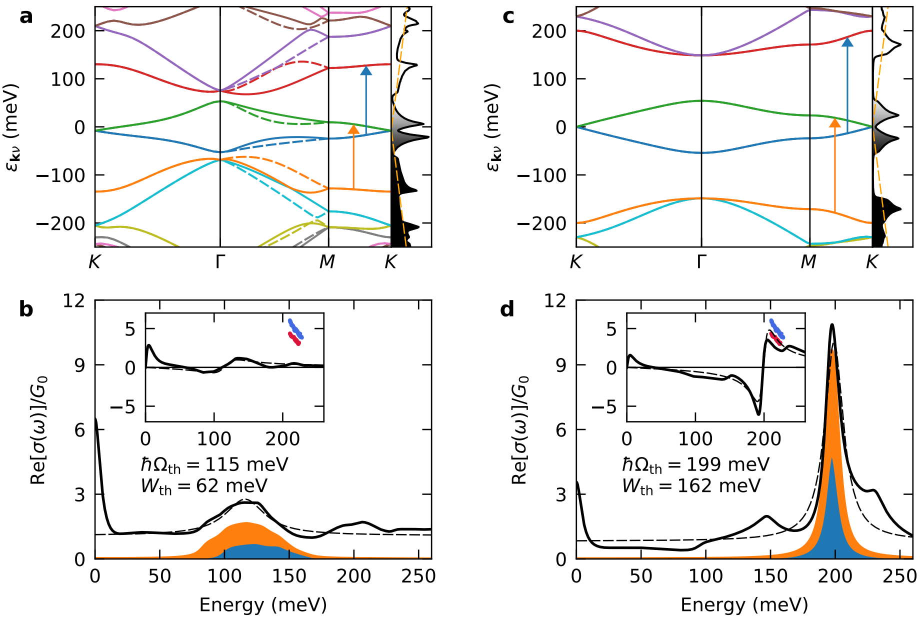

Figure 3.6: Electronic band structure and optical conductivity of twisted bilayer graphene with $\theta = 1.35°$. **a** Electronic band structure $\epsilon_{\mathbf{k}\nu}$ of TBG with $\theta = 1.35°$ along the $K\Gamma MK$ contour of the superlattice Brillouin zone from *ab initio* $\mathbf{k} \cdot \mathbf{p}$ perturbation theory[141]. The most relevant bands are $\nu = -2$ (orange), $\nu = -1$ (blue), $\nu = 1$ (green), and $\nu = 2$ (red). The corresponding wave functions at the K point for $\nu = -1$ and $\nu = 2$ are shown in Fig. 3.1**d**. Solid (dashed) lines represent the bands in the valley close to the K (K') point of the original graphene layers. The panel on the right shows the density of states with the colour shading representing band occupation at room temperature. The orange dashed line represents the density of states of single-layer graphene. Vertical arrows highlight the most relevant interband optical transitions. **b** Calculated real part of the optical conductivity (black thick line) using the Kubo formula and the band structure in panel **a**. Orange (blue) shading represents the contribution to the total optical conductivity of the pair of bands with $\nu = -2$, $\nu' = 1$ ($\nu = -1$, $\nu' = 2$), corresponding to the transition marked by an orange (blue) arrow in panel **a**. The dashed line is the Lorentzian fit to the most relevant interband feature and is used to extract the resonance parameters. The inset shows the imaginary part of the optical conductivity (normalized to G_0), together with the experimental data from Fig. 3.3**c**. **c**-**d**. Same as in panels **a**-**b** but with the band structure of the chirally-symmetric continuum model[37].

the theory and controls the location of the magic angle. An extensive theoretical discussion of collective modes in TBG as a function of the band-structure parameters can be found in Ref. 91.

Thus, our experiments suggest that, in particular regions of the sample, the AA tunnelling amplitude is substantially reduced with respect to the AB tunnelling amplitude but still has a non-vanishing value. This finding is compatible with the results of Refs. 15,18,22 that reported on the gap size between the flat bands and the first excited band at the Γ point of the superlattice Brillouin zone. This quantity provides a direct measure of the difference $u_1 - u_0$ and was found to be in the range $30 - 60$ meV. The apparent suppression

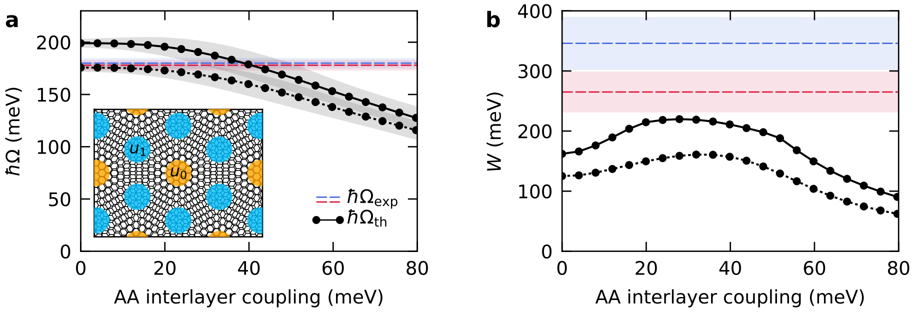

Figure 3.7: Calculated properties of the relevant interband transition as functions of the tunnelling amplitude in the AA regions. **a** Interband energy extracted from a Lorentzian fit of the optical conductivity. The solid (dotted) line corresponds to the model described in Ref. 141 (Ref. 38). The grey shaded areas represent plus/minus the half width at half the maximum of the Lorentzian fit. In both theoretical models used in this work (Ref. 141 and 38), $\Omega_{\rm th}$ decreases monotonically upon increasing the AA interlayer coupling u_0. These calculations were performed by setting $\theta = 1.35°$ and $u_1 = 97.5$ meV. The blue and red dashed lines correspond to the experimentally-determined resonant frequencies (Fig. 3.3**c**), with the corresponding shaded area indicating the uncertainty. The inset illustrates a triangular moiré lattice with the interlayer coupling strengths u_0, u_1 on the AA (yellow) and AB/BA sites (blue), respectively. **b** Same as in panel **a** but for the spectral weight $W_{\rm th}$. The latter displays a maximum for intermediate values of u_0.

of tunnelling in the AA regions compared to the one in the AB/BA regions (that is, the fact that $u_0 < u_1$) can stem from e-e interactions or extrinsic effects. It is known[35,37] that u_1 is responsible for a (non-Abelian) gauge field acting on the electron system, while u_0 induces a scalar potential. Electron-electron interactions act between density fluctuations and, because of the continuity equation between longitudinal current fluctuations. Consequently, screening due to e-e interactions tends to suppress the longitudinal field due to u_0, while having a smaller impact on the transverse gauge field due to u_1.

Extrinsic factors can also alter, locally, the value of u_0. We suspect that these include the way samples are prepared, the AFM-brooming procedure (Appendix A.2), and, possibly, the hBN encapsulation. It frequently happens that samples prepared in different laboratories display some macroscopic differences in their physical characteristics, such as twist angle[48], electrical transport[18,22–24,26,39] and spectroscopic features[28–31].

Before concluding, one may also hypothesize that our samples present a highly inhomogeneous strain distribution with patches where the associated pseudo-magnetic field $\mathbf{B}_{\rm S} = B_{\rm S}\hat{\mathbf{z}}$ is finite and nearly uniform[142] and regions where $B_{\rm S} = 0$. A resonant conductivity profile, as observed in experiments, would naturally arise in this case at the frequency of the pseudo-cyclotron resonance. We analyse this potential explanation of our observations in Supplementary Note 11 in Ref. 134 and conclude that it is unlikely since it would require an unreasonably large amount of strain to match the observed resonant frequency.

3.7. Conclusion

In summary, we have observed propagating interband collective excitations in TBG in the mid-infrared spectral region, with larger-than-expected group velocity and thus a larger spectral weight of the infrared optical transitions. The usefulness of models with reduced AA tunnelling coupling[37,38,141] in interpreting our experimental data could point to the enhanced role of e-e interactions. We expect that our work will encourage further theoretical and experimental studies to assess the intrinsic (that is, e-e) and extrinsic factors that can effectively renormalize the band-structure parameters and the reasons for the observed sample inhomogeneity. Future low-temperature studies can moreover elucidate the role of electronic correlations in the upper bands and the contribution of collective excitations to many-body ground states[143], while terahertz near-field imaging can offer a local probe of the electronic phase transitions[144].

4. Nano-imaging photoresponse in a moiré unit cell of minimally twisted bilayer graphene

In this Chapter, we perform near-field photocurrent nanoscopy on minimally twisted bilayer graphene (mTBG). With this, we probe nanoscale photocurrents in mTBG and observe a unique photothermoelectric effect governed by the symmetry breaking of the domain wall network. Our measurements are supported by simulations of the spatial photocurrent profile in our devices that shows the photoresponse originates from microscopic variations in the Seebeck coefficient intrinsic to the moiré lattice. By varying the doping, we observe anomalous sign reversals in the photocurrent that hints to the importance of strain gradients in mTBG. In addition, we observe a localized photoresponse close to the domain walls of the moiré unit cell that is attributed to additional electron heating from propagating polaritons.

4.1. Experimental scheme and device characterization

Minimally twisted bilayer graphene (mTBG) undergoes symmetry breaking due to the formation of a domain wall network, which motivates us to study its photoresponse by means of infrared scanning near-field photocurrent microscopy. As detailed in Sec. 2.5, this involves local photo-excitation of carriers using an s-SNOM system combined with electrical current/voltage read out at the device contacts. As we find in this work, the sharp domain walls act as local junctions converting electronic heat into a current (Fig. 4.1a). Spatially mapping out the photocurrent/voltage patterns in our samples allows us to unravel the underlying domain wall network and its properties.

The studied mTBG samples were fabricated using the tear and stack method[15,16] (Sec. 2.1). In brief, the heterostructure structure consists of a van der Waals stack of mTBG fully encapsulated with hBN and deposited on top of a Si/SiO_2 wafer. Our sample (Fig. 4.1b) also contains gold contacts for photocurrent/photovoltage read out and simultaneous electrostatic gating of the channel with the silicon backgate.

To characterize the local structure in our devices, we first measured the near-field optical scattering signal of our samples (Sec. 2.2). Figure 4.1c shows a near-field image of the optically scattered light measured at high doping $n \sim 5 \cdot 10^{12}$ cm^{-2} in our mTBG sample (Appendix B.1 for doping estimation). It reveals a set of bright fringes forming

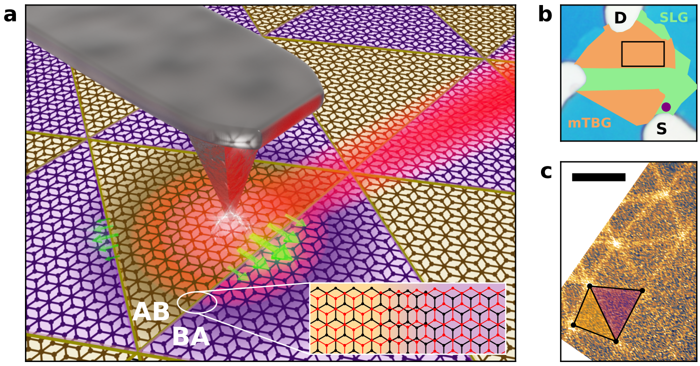

Figure 4.1: Design of experiment and device. **a** Schematic illustration of near-field photocurrent experiments performed in minimally twisted twisted bilayer graphene (credit: Matteo Ceccanti). The moiré domains of different stacking configurations are highlighted by yellow and purple shaded areas. The AFM tip couples infrared light into the device, causing the electron temperature to elevate locally. The photothermoelectric effect converts this heat partially into a current that can be read out by the contacts. Inset: Zoom of the domain wall structure separating AB-BA domains of the moiré lattice. **b** Device schematic of the main device under study. It consists of different regions of single-layer graphene (SLG) and minimally twisted bilayer graphene (mTBG) due to folding/stacking faults during the heterostructure assembly. The geometry for photocurrent measurements in Fig. 4.2 is marked by S (source) and D (Drain). The third contact is left floating. The purple dot marks the position where the calibration of carrier density is done (Appendix B.1). **c** Near-field scattering phase image corresponding to the yellow marked rectangle in Fig. 4.2, measured at $E = 117$ meV and $n \sim 5 \cdot 10^{12}$ cm^{-2}. The two shaded triangles mark two domains. Scale bar is 500 nm.

a triangular network of alternating AB/BA domains; the purple/yellow triangles highlight two neighbouring AB/BA domains. These features have already been studied extensively in near-field scattering experiments and were attributed to enhanced optical conductivity at the domain walls of mTBG[41,78,135]. Their observation in our experiment thus confirms the presence of atomic reconstruction[39] expected in mTBG and allows direct structural mapping of the moiré lattice in our samples.

For the following photocurrent measurements we used a fast current amplifier (Femto DLPCA-100). For simultaneous measurement of the photovoltage between two pairs of contacts, we used two differential voltage amplifiers (Ithaco 1201) with one common contact grounded. The carrier doping in our samples is tuned by applying a DC voltage between the Si backgate and our device. To avoid detecting unwanted far-field contributions to the scattered or photocurrent/voltage signal, we detect the near-field signals at the second or third harmonic of the cantilever oscillation.

4.2. Measuring near-field photoresponse in mTBG

Figure 4.2 shows a near-field photocurrent map of our sample measured in the mTBG region with an excitation energy $E = 188$ meV, which exhibits a number of interesting features. First, a clear periodicity in the photocurrent is observed throughout the entire sample. It can be easily seen by following the zeros in photocurrent (white lines and white features) that trace the periodicity intrinsic to mTBG. Notably, the periodicity varies from ~ 100 to ~ 1000 nm in different regions of the device. We attribute this behaviour to local variations in the twist angle ($\theta \sim 0.1 - 0.01°$) inherent to twisted moiré superlattices[48,64]. Second, the photocurrent exhibits alternating domains of negative response (blue regions) and positive response (red regions). This is most clearly seen in the device region with largest moiré periodicity (centre area in Fig. 4.2). Third, in these larger areas a second fringe can be seen running parallel to the domain walls. This double-step like feature closely resembles that of propagating polaritons typically observed in near-field scattering and photocurrent experiments on graphene[110,111,127] and hBN[95,113] close to crystal edges, and will be discussed in detail below. Importantly, this periodic structure in the photocurrent

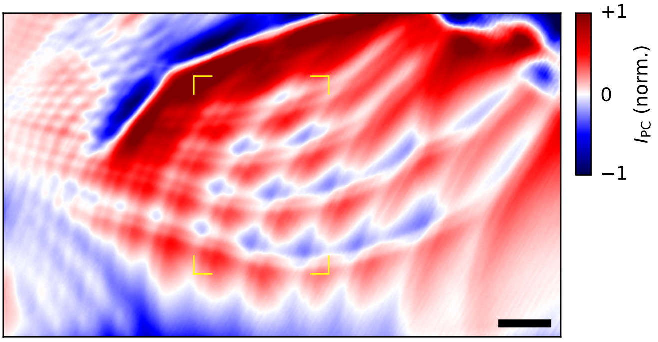

Figure 4.2: Near-field photoresponse in minimally twisted bilayer graphene. Photocurrent map of mTBG corresponding to the black rectangle in Fig. 4.1**b**, measured at carrier density $n \sim 1 \cdot 10^{12}$ cm^{-2} with an excitation energy $E = 188$ meV. Scale bar is 500 nm. The map is normalized by the maximum measured I_{PC}.

was characteristic in our other studied mTBG devices (Appendix B.2).

The spatial pattern of photoresponse is highly sensitive to the position of measurement contacts with respect to the moiré periodicity. Figure 4.3a shows a zoomed photovoltage map of the region with largest domains in Fig. 4.2d. This triangular pattern resembles the moiré pattern of mTBG (Fig. 4.1a), with zero crossings seemingly tracing the domain wall network of the moiré superlattice. However, when comparing our photoresponse data with our optical scattering data Fig. 4.1c), we find that the actual structure of the moiré lattice is rather different. The purple/yellow shaded triangles in Figure 4.3a highlight the positions and orientation of two neighbouring AB/BA domains measured by optical scattering (corresponding triangles in Fig. 4.1c). From this we can see that this measurement does not capture the entire structure of the moiré lattice, and we lose a set of domain walls at 45° to those observed in Figure 4.3a. Strikingly, those additional domain walls appear simply by measuring between a different pair of contacts (Fig. 4.3b). In this scheme, the actual structure of the moiré lattice is clearly visible and the spatial profile of the photoresponse is more complex than anticipated. For example, we find that the measured photovoltage exhibits sign reversals not only at domain wall boundaries (Figure 4.3c), but also within the AB/BA stacked domains. Moreover, the spatial patterns of the photoresponse within each moiré unit cell varies largely between AB and BA stacking configurations.

To elucidate the role and mechanism of photoresponse in mTBG, we studied the gate-voltage dependence of the photocurrent within the moiré domains. In Figure 4.4a, we plot the line trace of the measured photocurrent made across domain walls (black dashed line in Fig. 4.3a) for different gate voltages $V_G - V_D$, where V_D is the position of the charge neutrality point (CNP) determined from the gate dependence of the optically scattered signal (Supplementary Note 3 in Ref. 125). The positions of domain walls are marked by the black arrows. The first thing to note, is that the gate-voltage dependence of

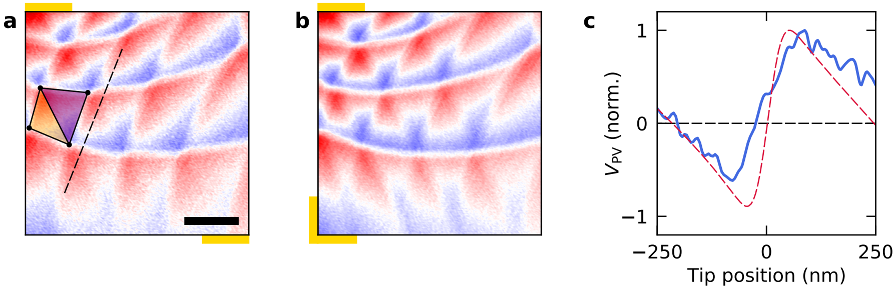

Figure 4.3: Photoresponse in the moiré unit cell of mTBG. **a** Zoomed map of measured photovoltage V_{PV} in the same sample presented in Fig. 4.1 (corresponding to the area with the largest domains in Fig. 4.2), measured at excitation energy $E = 117$ meV and carrier density $n \sim 1 \cdot 10^{12}$ cm^{-2}. The map is normalized to the maximum measured V_{PV}. Colour code: blue: -1, red: +1. The yellow/purple shaded triangles correspond to those in Fig. 4.1**c**. The gold annotations illustrate roughly the relative position of contacts used for measuring voltages. Scale bar is 500 nm. **b** Same as panel **a** but for a different choice of contacts (gold annotations) measured simultaneously. **c** Line cut across a horizontal domain wall in panel **b** (blue), together with a line trace of the simulated profile in Fig. 4.6**d** (dashed red).

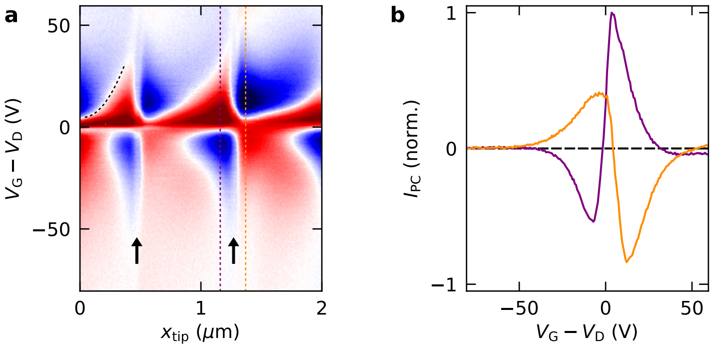

Figure 4.4: Gate dependence of photoresponse in mTBG. a Photocurrent as a function of gate voltage V_G (with respect to the position of the Dirac point V_D) measured for a line trace that crosses several domain walls (black dashed line in Fig. 4.3**a**). Black arrows mark the position of observable domain walls for this choice of contacts. The gate voltages correspond to carrier densities within roughly $\pm 6 \cdot 10^{12}$ cm^{-2}. **b** Gate-voltage response along the two line cuts highlighted in panel **a**, on two opposite sides of the domain wall.

the photoresponse is particularly sensitive to the position of the excitation spot within the moiré unit cell. On top of that, it is extremely non-monotonic, such that for some excitation positions it exhibits up to three sign changes. Figure 4.4b plots line cuts of the gate-voltage dependence for two excitation positions (marked by coloured dashed lines in Figure 4.4a). On one hand, the observed non-monotonic behaviour strongly resembles that of the photothermoelectric effect in graphene[123,145,146] that is strongest for lower n and exhibits sign reversals around CNP. This is not surprising considering the unit cell of mTBG is comprised mostly of AB Bernal stacked bilayer graphene, whose photoresponse is dominated by the photothermoelectric effect in the presence of spatially varying Seebeck coefficients[123,124,145,146]. On the other hand, some other features such as the two additional sign changes away from charge neutrality, which depend on the spatial location, are rather peculiar.

4.3. Photothermoelectric effect in a domain wall network

With Figures 4.3 and 4.4 in mind, we constructed a model based on the photothermoelectric effect (PTE) to describe the observed photocurrent features in mTBG, following the general description of the PTE introduced in Sec. 2.5. The details of this model are worked out in large part by Iacopo Torre. In the moiré superlattice of mTBG, the local layer alignment transitions smoothly in the region of the domain walls, which is expected to cause local gradients in the Seebeck coefficient, as required for the PTE. To corroborate this, we calculated (Appendix B.4 for full details on the calculation) the Seebeck coefficient of bilayer graphene as a function of the layer alignment in the Relaxation Time Approximation[91] and mapped the local alignment to the distance from a domain wall using the result in Ref. 33. By this procedure we obtained the spatial profile of the Seebeck coefficient across a domain wall, as depicted in Figure 4.5b. This shows that the Seebeck

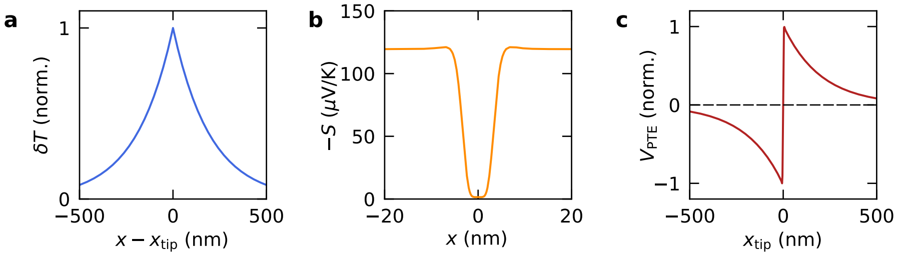

Figure 4.5: Simulation of the photothermoelectric response of a single domain wall. **a** Profile of the electron temperature increase induced by local photoexcitation as a function of distance (x) from the excitation position (x_{tip}), for a cooling length of 200 nm. **b** Calculated Seebeck coefficient as a function of position within two moiré unit cells separated by a domain wall at $x = 0$ nm. **c** Line trace of the calculated photovoltage across a domain wall using the thermal profile and Seebeck coefficient of panel **a** and **b**.

coefficient dips sharply at the domain walls of the moiré superlattice. By considering equation Equation (2.5) and recalling that $V_{\mathrm{PTE}}^{(m)} \propto \mathcal{R}_{\mathrm{PTE}}^{(m)}$, we plot the expected photovoltage profile in the vicinity of the domain walls in Fig. 4.5c for a typical thermal profile induced by local photoexcitation (Fig. 4.5a). Notably, the photovoltage follows a non-monotonic dependence with position through the domain wall, changing sign as it crosses the middle of the domain wall. Such behaviour can indeed be seen in our data along certain domain walls (Fig. 4.3c).

Whilst the one-dimensional model (Fig. 4.5c) describes well the sign changes across certain domain walls (Fig. 4.3c), the full two-dimensional spatial map can be more complex as one must consider the photocurrent contributions from different domain walls due to the finite cooling length L_{cool}. The full spatial profile of $\mathcal{R}_{\mathrm{PTE}}^{(m)}(\mathbf{r})$ can be calculated if the entire measurement geometry of the system (Fig. 4.6a) and the spatial profile of the Seebeck coefficient (Fig. 4.6b) are known. We perform this calculation using the Finite Element Method (Appendix B.3). The calculation is greatly simplified thanks to a elegant reciprocity relation[147,148].

Figure 4.6c and Fig. 4.6d plot the simulated photocurrent for the two measured contact configurations (Fig. 4.6a) in the same area corresponding to the measurement in Fig. 4.3a and Fig. 4.3b respectively. The simulations are carried out at a fixed doping $n = 10^{12}$ cm^{-2}. Comparing Fig. 4.6c,d with Fig. 4.3a,b we find good agreement between our measurements and the simulations. Not only do our simulations accurately capture the spatial sign changes observed in our sample, but also the differing local photoresponse between AB and BA stacked regions (Fig. 4.3b and Fig. 4.6d). Importantly, the simulations also capture the strong directional effect observed. To understand this behaviour, we recall that the PTE can generate a global current only in regions where the gradients of Seebeck coefficient contain a part running parallel to the projection of current flows between contacts. This means that the domain walls perpendicular to the projection of current flows contribute strongest to the measured photocurrent and are minimum for those that run parallel. The current projections for the two contact configurations are sketched in Fig. 4.6a, where the red and white lines depict projections for the contact configuration of Fig. 4.3a and Fig. 4.3b respectively. They are also drawn in Fig. 4.6b to illustrate their orientation relative to the domain wall networks measured in Fig. 4.3a,b. In the first configuration (red lines), we find

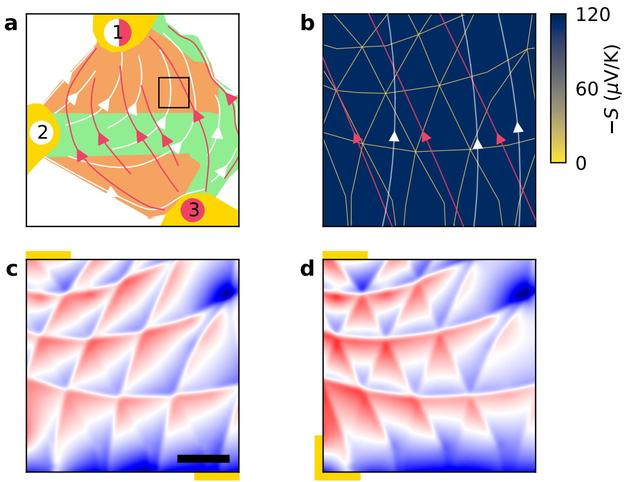

Figure 4.6: Simulations of the photothermoelectric response in mTBG. **a** Illustration of the geometry used in our photocurrent simulations. The yellow semi-circles indicate contact probes, the green single-layer graphene regions and the orange mTBG regions. The red projection of current flows corresponds to a configuration wherein current flows between contacts 3 and 1, while the white field lines correspond to current flowing between contacts 2 and 1. The black square highlights the region shown in panels **b**-**d**. **b** 2D spatial map of the calculated Seebeck coefficient (Appendix B.4) that goes into our model, along with the projections of current flows shown in panel **a**. **c** Zoom of the photovoltage simulations in the region of mTBG (same area as Fig. 4.3**a**). Here we convolute the calculated responsivity with a Gaussian function of width 15 nm to account for the finite tip radius. Colour code: blue: -1, red: +1. Scale bar is 500 nm. **d** Same as in panel **c** but for a different measurement geometry (same as Fig. 4.3**b**).

that some domain walls run almost parallel to the current projections. Therefore, photoexcitation at these domain walls does not contribute to the globally measured current, and they remain completely hidden in our measurement (Fig. 4.3a). Whereas in the second case (white lines), there is always a component perpendicular to all sets of domain walls such that they all contribute to the globally measured current (Fig. 4.3b). This result also demonstrates the crucial importance of measurement geometry[149] in understanding the nanoscale photoresponse of solid-state crystals.

Good agreement between the simulations and experiment points towards a photothermoelectric dominated photoresponse in the moiré lattice of mTBG. Indeed, qualitatively the spatial sign changes across domain walls and doping dependent sign changes around the CNP are well described by our photothermoelectric model; we attribute the slight shift of zero crossings from $V_G - V_D$ (Fig. 4.4) to additional photocurrent mechanisms that may play a role at the CNP[150]. Even the additional sign changes observed away from CNP (purple trace in Fig. 4.4b), can be explained within the framework of the PTE by considering an enhanced Seebeck coefficient at the domain walls with respect to the calculated one (Supplementary Note 7 of Ref. 125). That said, it does not accurately describe the spatial dependence of the gate-voltage response, specifically, the sign reversal of the photoresponse within the moiré domains shifting with applied gate voltage (dashed line in Fig. 4.4a). This behaviour points towards a spatially varying parameter not considered in our model, for example, a spatially varying Seebeck coefficient within the AB/BA domains themselves that is not localized at the domain walls. Such behaviour might be expected in the case that lattice reconstruction in mTBG imposes considerable strain in the AB regions[40], which might enhance the Seebeck coefficient of bilayer graphene locally[151]. A simplified model, which includes a spatially varying Seebeck within the AB/BA domains, is presented in Supplementary Note 7 of Ref. 125 and shows similar features as the experimental data.

Another peculiarity in the data is the high doping behaviour ($V_G - V_D > 40$ V), in which the spatial sign changes across domain walls becomes nearly absent (Fig. 4.4a) and the spatial profile resembles that of a constant background, which changes sign when changing carrier polarity. This is illustrated in Fig. 4.7a that plots a photocurrent map for a doping $n = 4 \cdot 10^{12}$ cm^{-2}, where we observe large areas of the moiré lattice exhibiting either a constant positive or negative photoresponse. In the simplest case, we might attribute this additional photocurrent to nearby pn-junctions caused by deformations/stacking faults in our heterostructure. However, our measurements of the cooling length from these interfaces ($L_{\mathrm{cool}} = 240$ nm) show a fast decay of such contributions (Appendix B.5). Hence, the data suggests another photocurrent mechanism might be present in mTBG. For example, we considered the possibility of photogalvanic currents (Appendix B.6). Further work is required to understand these additional background phenomena.

4.4. Photoresponse from hyperbolic phonon-polaritons

Finally, we address the double step-like feature that is observed close to the domain walls (Fig. 4.2, Fig.4.4a, Fig.4.7a). At first inspection, those features resemble that of propagating polaritons in graphene/hBN heterostructures typically observed in s-SNOM experiments[85,86,110,111,113]. As shown in this work, the domain walls also act as local photoactive junctions which would thus enable thermoelectric detection of polariton modes[95,126,152]. For investigation, we studied the wavelength dependence of the double-step feature focussing on energies 150 – 200 meV where it appeared strongest (Fig. 4.2). Figure 4.7b plots the photoresponse as a function of excitation wavelength for a line trace made across several domain walls in one of our mTBG samples. For all energies, we observe the expected photocurrent profile generated at domain walls by the photothermoelectric effect (Fig.4.5c). However, we also observe an additional feature that disperses with energy in the specific range 180 – 200 meV but is completely absent for lower energies. This spectral range corresponds to the upper Reststrahlen band of hBN and suggests those features originate from propagating phonon polaritons in hBN.

For further analysis, we compare in Figure 4.7c line traces of the measured photoresponse (yellow arrow in Fig. 4.7b) at different energies after subtraction of a smooth background. Note, whereas we plot the modulus to make analysis easier, we draw attention to the fact that the actual response is a reduction in the measured photocurrent compared to the background (Fig. 4.7b). Following this procedure for all traces in Fig. 4.7b, we plot in Figure 4.7d the distance between peaks and the domain wall as function of excitation energy (red dots). When the excitation energy is inside the Reststrahlen bands of hBN, the AFM tip can excite hyperbolic phonon-polaritons that travel in hBN as collimated rays that propagate with a fixed angle $\theta_{\mathrm{BM}} = \tan^{-1}\left[\mathrm{Re}\left(\frac{i\sqrt{\epsilon_{x,y}}}{\sqrt{\epsilon_z}}\right)\right]$ relative to the vertical direction[152] (ϵ_i being the components of the dielectric function of hBN). This produces a series of

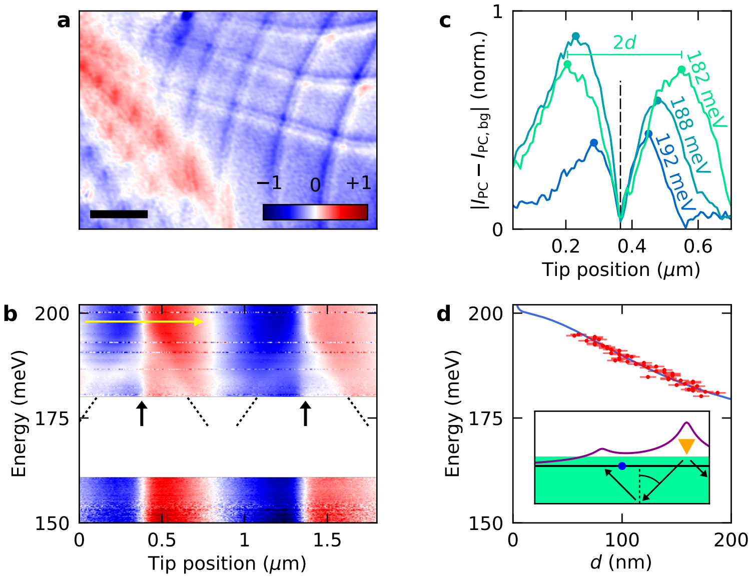

Figure 4.7: Anomalous photocurrent and non-local heating via polariton rays. **a** Spatial map of the normalized photocurrent (I_{PC}) at an excitation energy of 117 meV and doping $n \sim 4 \cdot 10^{12}$ cm^{-2}. Scale bar is 500 nm. **b** Normalized I_{PC} as a function of excitation energy and excitation position (x_{tip}) crossing two domain walls (marked by black arrows) in another of our mTBG samples. Colour code: blue: -1, red: +1. The dashed lines are guides to the eye showing the dispersive nature of the double-step feature, which appears as a local reduction of the photocurrent magnitude on either side of the domain wall. The white area corresponds to a gap in the spectrum of our laser. **c** Line traces (as absolute value) of a few energies taken from panel **b** (yellow arrow in panel **b**) plotted after background subtraction; the background is experimentally extracted from the line trace at 202 meV where the double-step feature is not observed. We define the distance between the peaks as $2d$. **d** Distance between the domain wall and observed peak (d) plotted for different excitation energies (red dots), along with a fit to $a\lambda_{ray}$ (blue line). We estimate the error in d to be ±7.5 nm based on the spatial resolution of our scan. The inset is a schematic showing the thermal profile (purple) induced by light coupled in via the AFM tip (yellow triangle). In addition to heating the electron lattice, the tip also excites hBN phonon rays (black arrows), which are able to propagate to the opposite side of the domain wall (blue dot) and cause additional heating that produces a photocurrent contribution of opposite sign.

maxima of electric field intensity close to the surface separated by a distance $\lambda_{ray} = 2t \cdot \tan\theta_{BN}$, where t is the total thickness of the hBN. We note our photocurrent measurements are more sensitive to ray-like modes rather than the first eigenmode typically observed in s-SNOM experiments[113,153,154] (details in Appendix B.7). Following this insight, we fit the distance d between the dispersing feature and the domain wall (Fig. 4.7d) with the function $d(\omega) = a\lambda_{ray}(\omega)$, with a as a proportionality constant. The fit yields $a = 0.63$ and shows good agreement with experimental data (Fig. 4.7d) providing strong evidence that the dispersing feature is caused by hBN hyperbolic phonon-polaritons. We observe that $a < \frac{t_{top}+2t_{bot}}{2t_{top}+2t_{bot}} = 0.95$ (hBN ray passing once through the top-hBN and twice through the bottom hBN), which suggests that phonon-polariton rays launched by the AFM tip propagate beyond the domain wall into neighbouring domains. This is consistent with the fact that the dispersing feature traces a reduction in the measured photocurrent, because propagating phonon polaritons heat the mTBG on the side of the domain wall opposite to the tip (sketched in inset of Fig. 4.7d). This produces photocurrents that counteracts the one generated by the heat directly produced by the tip, leading to a small reduction of the photocurrent signal (Fig. 4.7b). We note that Fig. 4.4a and Fig. 4.7a also show a fainter double step feature, while the data are taken outside the Reststrahlen bands of hBN. We speculate that the double step feature in this case might originate from heating by propagating plasmon polaritons that have been shown to scatter/reflect from domain walls of mTBG[41,78,135].

4.5. Conclusion

In this Chapter, we showed that near-field photocurrent spectroscopy is a valuable tool for studying the optoelectronic properties of moiré superlattices. Our moiré-scale resolved measurements, and related work from the group of Prof. Basov[155], reveal a spatially rich photoresponse governed by the symmetries of the reconstructed lattice that would go unnoticed in typical far-field photoresponse experiments. Good agreement of our simulations with experimental data shows the importance of hot carriers in the photoresponse of mTBG and, at the same time, shows the crucial link between global measurements and local excitation in photocurrent experiments. This work should thus motivate further near-field photocurrent studies on related moiré superlattices including twisted transition metal dichalcogenides[98] and small-angle twisted bilayer graphene.

5. WSe_2 as transparent top gate for near-field experiments

Independent control of carrier density and out-of-plane displacement field is essential for accessing various fascinating states in 2D material heterostructures. While being straightforward in transport experiments, such control has remained a challenge for near-field studies because metal electrodes block the near-field access. In this Chapter, we experimentally verify that WSe_2 *can be used as a transparent top gate in infrared s-SNOM experiments. We perform nano-imaging of plasmons in bilayer graphene and tune the plasmon wavelength using a few-layer* WSe_2 *gate, allowing us to extract the gating efficiency. A minimal model that takes the quantum capacitance of* WSe_2 *into account explains the observed gate response.*

Near-field optical microscopy has proven itself as a rich technique for exploring the optical properties of materials on the nanoscale. Most near-field studies on 2D materials and their heterostructures performed these days use scattering-type scanning near-field microscopy (s-SNOM), where a sharp metallic tip generates a hotspot of light interacting with the sample. Such sharp tip also bridges the momentum mismatch between free-space light and collective excitations, making s-SNOM an appealing tool for imaging such excitations[85,86].

A key parameter in many s-SNOM experiments on 2D-materials is the carrier density, which is typically tuned via the field effect induced by a gate electrode below the sample. A notable example of this tunability is found in single-layer graphene, where the carrier density has a direct impact on the plasmon dispersion. Varying the carrier density in these experiments has given crucial information to understand the nature of these collective excitations, in particular their carrier-density dependence and the role of many-body effects[87,110–112,127]. Tuning the carrier density also gave an insight into the plasmonic properties of a photonic lattice formed by minimally twisted bilayer graphene[78]. Besides being a tuning knob in experiments, a modulation of the carrier density can enhance the sensitivity of the near-field signal via a lock-in detection scheme. This technique was employed to detect intersubband transitions in transition metal dichalcogenides (TMDs)[120].

The field effect does not only inject carriers into the sample of interest, it also induces a perpendicular displacement field. Whilst the effect of such field on the properties of single-layer graphene is only minor as it is only one atom thick, it can have a more pronounced effect in other materials. For instance, a displacement field modifies the band structure of bilayer graphene by opening a band gap[156]. Hence, independent control of the carrier density and displacement field is of great relevance for exploring novel states of matter using s-SNOM. Domain walls in gapped bilayer graphene are predicted to host long-lived plasmons with lifetimes two orders of magnitude higher than in single-layer graphene[83]. Recent experiments have shown tunability of correlated states in twisted double bilayer graphene using a displacement field[157,158], while twisted trilayer graphene under a displacement field has raised the bar of T_c in graphene-based systems beyond 2 K[81,82]. Thus far, such independent control of carrier density and displacement field has remained a hurdle in s-SNOM experiments, as it requires one of the two gate electrodes to be placed above the material of interest. Since a metal electrode on top of the sample screens the electric fields, it effectively blocks the near-field access to the sample.

Recent experiments have made advances in realizing a transparent top gate for s-SNOM experiments, but still face certain drawbacks. While single-layer graphene is sufficiently transparent to probe near-field signals through it[63], its own plasmonic resonance interferes with the optical response of the material underneath, complicating the interpretation of the observed near-field signal[159,160]. Still, for studying structural changes that are insensitive to the plasmonic modes of graphene this is not an obstacle[63]. As alternative the TMD MoS_2 has been proposed, which indeed does not host any resonances that disturb the near-field signal[159]. However, since this material is unipolar due to Fermi level pinning at the contacts, it can only introduce p-type doping in the material below[161].

5.1. Design of experiment and device

In this experiment we seek for a material acting as an infrared-transparent top electrode, of which we validate its performance in the most relevant way. By studying the change in induced plasmon wavelength λ_p (defined by the inverse of the in-plane wavevector) in bilayer graphene we assess the carrier density induced by the top gate, while at the same time we characterize to what extent a charged top layer obstructs the observation of plasmons.

An ideal transparent top gate electrode should be a van der Waals material, ensuring flat surfaces and easy integration in the stacking procedure. By utilizing a flake of only a few layers in thickness, our near-field probe can still come sufficiently close to interact with the exponentially-decaying near-field electromagnetic field of the sample. Furthermore, it should be free of strong intraband absorbtion and plasmon or phonon resonances in the infrared region as they might obscure the detected signal. These resonances can also hybridize with the polaritons of interest originating from other layers, complicating the interpretation. In this regard a low-mobility material is favoured, as any inherent plasmonic resonances will be strongly damped, while this does not limit its capacity to host static charges in its role as top gate. Finally, for complete tunability our top gate has to be ambipolar, in order to introduce carriers of both electron and hole type.

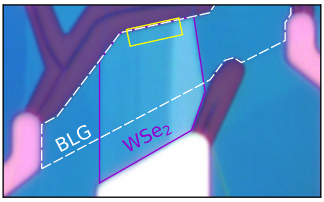

Figure 5.1: Optical image of device. Optical image of our device, with the locations of bilayer graphene (dashed white) and WSe_2 (solid purple) indicated.

To overcome the drawbacks faced in previous experiments and in light of these requirements, the TMD WSe_2 seems an ideal candidate. This semiconducting material can be exfoliated down to a single layer of 0.7 nm[162,163] and has relatively low mobilities up to 500 cm^2/Vs[162,164]. In contrast to MoS_2, WSe_2 is ambipolar and thus allows for injecting both carrier types[165]. A common issue arising with TMDs is the Schottky barrier forming at the metal-semiconductor interface, typically severely blocking transport through either the valence or conduction band. This can be overcome by making use of two different metals for either the source and drain contacts[166]. However, since we intend to use WSe_2 solely as a gate electrode, a highly resistive contact does not pose an issue, provided we do not modulate the carrier density at high frequencies.

A potential alternative to a TMD could be a thin mono-crystalline film of bulk metal such as gold. In order to be transparent in the relevant optical range, the electrode thickness should be well below the skin depth of the material to avoid screening the near-field electromagnetic field. Typical metals have a skin depth of 10s of nanometres for infrared frequencies[167], which requires the metal film to be only several nanometres thick. Whilst this has recently been accomplished with silver films[168,169], the growth process does not allow for an easy integration and such thin films tend to show thickness inhomogeneity[169].

Figure 5.2 shows a schematic of the dual-gated device used in this experiment using WSe_2 as top gate. Following the same stacking and nano-fabrication techniques outlined in Sec. 2.1, we built a device consisting of hBN-encapsulated bilayer graphene (BLG). From commercially available WSe_2 crystals (HQ Graphene) we exfoliate a thin staircase flake acting as a top gate. Given the quick decay of the near-field signal in the out-of-plane direction, we use a 4 nm thin top hBN flake. The Si/SiO_2 bottom gate serves as a traditional backgate to bring BLG into a highly doped state where plasmons do not suffer from Landau damping[87]. In addition, the bottom gate provides a reference for determining

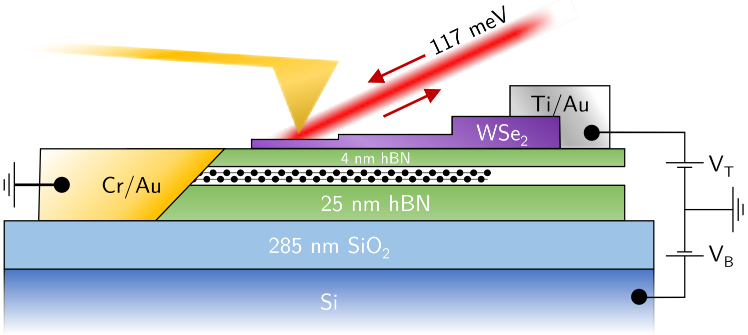

Figure 5.2: Device schematic. Schematic of our near-field experiment on a device consisting of hBN-encapsulated bilayer graphene. By applying a voltage to a staircase flake of WSe_2 (2-6 layers), we tune the carrier density in bilayer graphene without obstructing the near-field access, as verified by probing the plasmon properties. Together with the Si gate this allows full control of the carrier density and displacement field in bilayer graphene.

the plasmon wavelength λ_p as function of the induced carrier density n. Low-resistance contacts to BLG are made by reactive ion etching in a CHF_3/O_2 gas mixture, followed by Cr/Au metallization. The WSe_2 flake is contacted with Ti/Au with the aim to avoid a high Schottky barrier. However, as explained above and more recent in-house experiments showed, Cr/Au provides an equally well-functioning contact to a WSe_2 top gate. Finally, to prepare the device for s-SNOM measurements, we mechanically cleaned the top surface using contact-mode AFM brooming[102]. Figure 5.1 shows a picture of the device. Over the course of two months, we did not observe any signs of degradation of the WSe_2, despite performing the experiments in ambient conditions.

5.2. Measuring and controlling plasmons through WSe_2

Figure 5.3 shows a near-field image of highly doped BLG ($n \sim 10^{13}$ cm^{-2}), which we induce by solely using the bottom gate at $V_B = 80$ V along with photodoping. The latter involves photoexciting defect states at the SiO_2/hBN interface[93,170], which effectively sets

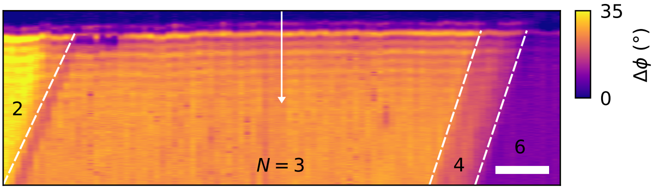

Figure 5.3: Spatial map of plasmon polaritons in BLG. Map of the near-field phase contrast at the edge of the bilayer graphene, corresponding to the yellow box in Fig. 5.1. The Si gate induces a high carrier density $\sim 10^{13}$ cm^{-2} ($V_B - V_D = 145$ V), allowing the propagation of plasmon polaritons, as seen by the fringes running parallel to the edge. The area shown is covered by WSe_2 of various thicknesses, as indicated by the number of layers. The excitation energy is 117 meV and the scale bar is 300 nm.

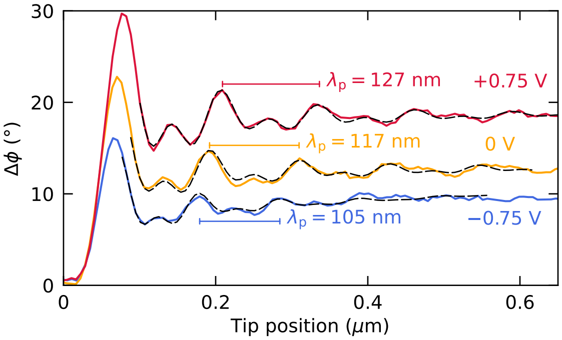

Figure 5.4: Controlling plasmon wavelength with a WSe$_2$ top gate. Line cuts along the white arrow in Fig. 5.3 demonstrate the effect of the WSe$_2$ top gate while keeping $V_B - V_D = 145$ V. Without obstructing near-field access, applying a voltage to WSe$_2$ alters the carrier density in BLG (V_T indicated for each line cut), which affects the measured plasmon wavelength λ_p as extracted from a fit (black dashed lines).

the charge-neutrality point V_D at -65 V. The fringes running parallel to the BLG edge are a manifestation of plasmon polaritions, which we observe as both tip-lauched edge-reflected ($\lambda_p/2$ period) and edge-launched (λ_p period)[87], see Eq. (2.3). In this case the voltage on the top gate is 0 V, meaning WSe$_2$ acts as a simple dielectric, and hence we do not expect any alteration/obscuration of the measured plasmons.

As a next step, we apply a voltage V_T on the WSe$_2$ top gate while keeping BLG in the same highly doped state, and record the near-field signal along the arrow in Fig. 5.3. At this location the top gate consists of three layers of WSe$_2$ with total thickness of ≈ 2.2 nm. Figure 5.4 demonstrates that by applying a voltage to the top gate we are able to change the observed plasmon wavelength. By fitting the oscillations to the model introduced in Sec. 2.4 we determine the change in plasmon wavelength to be ± 10 nm for $V_T = \pm 0.75$ V. This means that WSe$_2$ is able to induce carriers of both types in BLG, and thus acts as

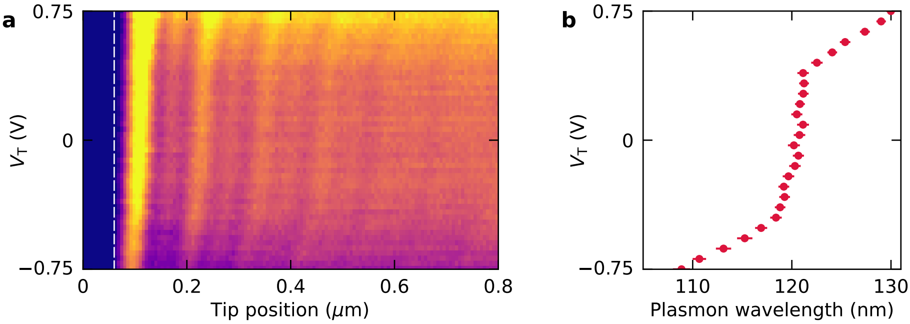

Figure 5.5: Systematically measuring the response of the WSe$_2$ top gate. **a** Line cut of the near-field phase signal along the white arrow in Fig. 5.3 for a range of top gate voltages, while $V_B - V_D = 145$ V. The edge of bilayer graphene is marked with a dashed line. Colour scale is the same as in Fig. 5.3, covering 18 degree phase difference. **b** The extracted plasmon wavelength shows a piece-wise linear dependence on the top gate voltage. The error bars represent $\pm 1\sigma$.

an ambipolar top gate. In addition, the near-field contrast is not affected in the slightest manner, validating that it fulfils well the transparency condition.

To study the response of the transparent top gate in more detail, we measure the near-field signal while systematically scanning the voltage on the top gate, shown in Fig. 5.5a. Judging by the fringe spacing for different V_T, these data suggest that the top gate only becomes 'active' for high $|V_\mathrm{T}|$. To examine this quantitatively, we fit the data to Eq. (2.3) for each voltage, and extract the plasmon wavelength as function of top gate voltage (Fig. 5.5b). We find indeed a piece-wise linear function with an inactive region for low $|V_\mathrm{T}|$, while the slope of $\lambda_\mathrm{p}(V_\mathrm{T})$ is rather similar for $|V_\mathrm{T}| > 0.4$ V.

5.3. Determining the gating efficiency of WSe$_2$

To understand the particular shape of $\lambda_\mathrm{p}(V_\mathrm{T})$ from a perspective of the electrostatics in our device, we first need to determine the induced carrier density in BLG by the WSe$_2$ top gate. To do so, we calibrate $\lambda_\mathrm{p}(n)$ by using the Si bottom gate as a reference. According to Eq. (5.1) introduced below, when $V_\mathrm{T} = 0$ V the induced carrier density can be described by a simple parallel plate capacitor only dependent on V_B. We measure the plasmon fringes along the same line cut while varying voltage on the bottom gate and keeping $V_\mathrm{T} = 0$ V (Fig. 5.6). By applying the same fitting procedure, we extract a linear dependence of the plasmon wavelength on V_B, as is expected for a two-dimensional conductor with parabolic bands[171]. Using the capacitance of the Si gate as mentioned below and $V_\mathrm{D} = -74$ V in this measurement, we estimate the plasmon wavelength in nm as $\lambda_\mathrm{p} = 8.23n + 34.5$ with n in units of 10^{12} cm^{-2}, corresponding to the linear fit in Fig. 5.6b.

From this calibration, we can convert the measured change in plasmon wavelength (Fig. 5.5b) to the induced carrier density Δn by the WSe$_2$ top gate. Figure 5.7a shows this, along with a fit to a minimal model that calculates n for given bottom and top gate voltages.

This model calculates the carrier density n in BLG for given gate voltage V_B and V_T,

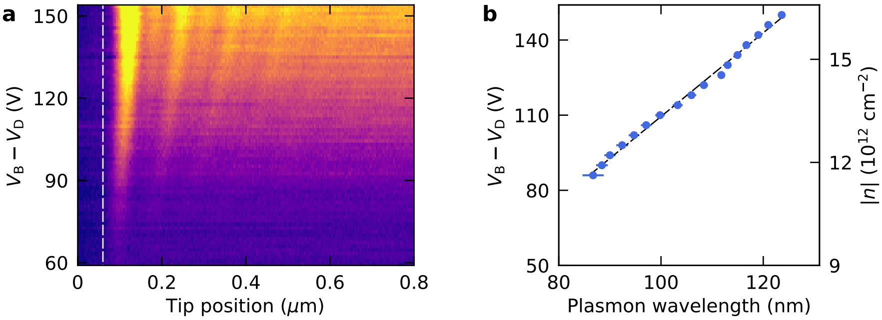

Figure 5.6: Calibrating the plasmon wavelength to the carrier density. **a** Near-field phase signal along the same line as Fig. 5.5**a** for a range of bottom gate voltages ($V_\mathrm{T} =$ 0 V), serving as calibration to determine the carrier density induced by the WSe$_2$ top gate. **b** The extracted plasmon wavelength scales approximately linear with the bottom gate voltage and carrier density, as indicated by a linear fit (dashed line). The definitions of colour scale and error bars are the same as in Fig. 5.5.

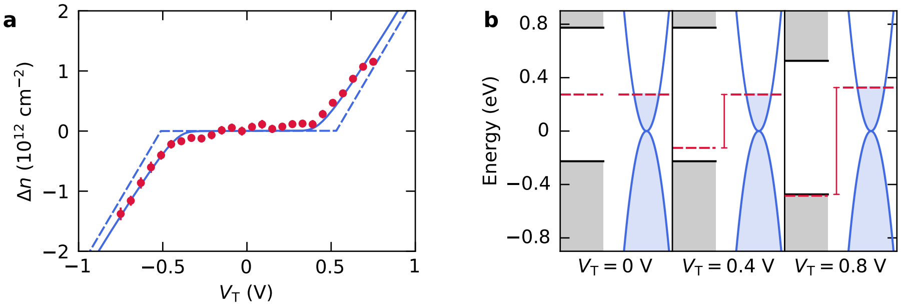

Figure 5.7: Gating efficiency of trilayer WSe$_2$ and band alignment. **a** Induced shift in the carrier density Δn in BLG by applying a voltage to WSe$_2$ through a 4 nm hBN layer. The flat response for small top gate voltages ($|V_\mathrm{T}| < 0.4$ V) arises from the intrinsic gap in WSe$_2$, while for larger voltages ($|V_\mathrm{T}| > 0.4$ V) WSe$_2$ acts as a conductor and the slope is determined by the geometric capacitance. From a fit according to the electrostatic model with $T = 300$ K we extract a gap of 1.04 eV in WSe$_2$ (solid line). The dashed line represents the calculated Δn at zero temperature using the same fit parameters. **b** Band alignment of semiconducting WSe$_2$ (grey bands) with respect to BLG (blue bands) for three different positive top gate voltages. For small V_T, the chemical potential of WSe$_2$ shifts down by V_T (middle panel). Once V_T is large enough that the chemical potential of WSe$_2$ reaches the valence band edge, carriers are injected in BLG moving its chemical potential upwards (right panel). At the same time, the bands of WSe$_2$ and BLG are shifted apart such that the V_T equals the difference in chemical potentials, indicated by the vertical bar.

and takes the electrostatics and equilibrium of the electrochemical potential into account. The latter requires extra attention, since the top gate WSe$_2$ is not an ideal conductor. The model is worked out by Iacopo Torre, and is presented in detail in Appendix C.1. In this simplified model we consider both BLG and few-layer WSe$_2$ as perfect two-dimensional materials neglecting the electrostatic potential drop between the different layers. To be consistent with this assumption we also neglect the modification of the band structure of BLG due to the presence of an out-of-plane field and the corresponding opening of a gap. This leaves us with a simple parabolic band model for BLG with an energy-independent density of states determined by the effective mass $m^* \approx 0.046 m_\mathrm{e}$ with m_e being the bare electron mass[156]. It is beyond our scope to accurately model the carrier density dependence of BLG here, which would require either a more complex screened tight-binding model[172], or various fitting parameters[173].

The main result of our model is captured by the following equation

$$n = \frac{C_\mathrm{B}(V_\mathrm{B} - V_\mathrm{D})}{e} + \frac{C_\mathrm{T} V_\mathrm{T}}{e} + \frac{C_\mathrm{T} \Delta\mu_{\mathrm{WSe}_2}(V_\mathrm{T})}{e^2}, \tag{5.1}$$

where $C_\mathrm{T} \approx 7.7$ mF/m^2 and $C_\mathrm{B} \approx 0.12$ mF/m^2 are the geometric capacitances corresponding to the top and bottom gate, e is the unit charge and $\Delta\mu_{\mathrm{WSe}_2}$ is the shift in chemical potential of WSe$_2$ and is set to zero for $V_\mathrm{T} = 0$ V. From this equation we see that for $V_\mathrm{T} = 0$ V, the carrier density in BLG can be described by the geometric capacitance of the bottom gate (first term), which we used for the calibration of $\lambda_\mathrm{p}(n)$ above. On the other hand, once we fix V_B, the change in carrier density is determined by the geometric capacitance of top gate (second term) and the quantum capacitance of WSe$_2$

(last term). The interplay of the last two terms causes the step-like behaviour seen in Fig. 5.7a. Details on the function $\Delta\mu_{WSe_2}(V_T)$ are presented in Appendix C.1, along with the full solution of Eq. (5.1) used for the fit in Fig. 5.7a.

A band alignment diagram of WSe_2 and BLG explains gating response in more detail (Fig. 5.7b). Starting with a BLG at a high carrier density induced by the bottom gate, the chemical potentials of WSe_2 and BLG are aligned for $V_T = 0$ V. In this situation the chemical potential of WSe_2 resides within the valence and conduction bands. Upon increasing V_T, owing to the low quantum capacitance of WSe_2 in its insulating state, $\Delta\mu_{WSe_2}$ shifts down by V_T until it reaches the valence band. Once that happens, holes are introduced in the valence band and the induced electrons in BLG shift the chemical potential of BLG upwards. Due to the relatively high density of states of the valence band of WSe_2, its chemical potential remains close to the valence band edge for higher carrier densities. Since the difference in chemical potential between WSe_2 and BLG has to be equal to V_T, the bands of WSe_2 and BLG separate in energy for higher carrier densities.

In fitting the data to our model in Fig. 5.7a, we only leave the valence and conduction band energies as free fit parameters, while the other parameters can be estimated with sufficient accuracy. The fit yields a band gap of 1.04 eV, and is almost perfectly centred at $V_T = 0$ V. The error is largely determined by the estimation of the density of states in WSe_2: reducing or increasing this by an order of magnitude changes the extracted band gap by ±0.1 eV. Even though a gap of 1.04 eV agrees well with DFT calculations[174–176], experimental values typically report higher values around 1.45 eV[175,177,178]. We believe that the discrepancy with our results is caused by the charge imbalance present in WSe_2 when generating an external electric field. The internal field due to the charge imbalance can modify the electronic bands and is expected to reduce the gap size[174–176].

5.4. Conclusion

In summary, here we have shown that few-layer WSe_2 is well suited as ambipolar transparent top gate for near-field experiments. This is demonstrated by tuning the plasmonic excitations in bilayer graphene via a WSe_2 top gate, without hindering near-field access. Nanoscale measurements of the plasmon wavelength allow us to extract the gating efficiency, which we capture in a minimal model that considers the geometric and quantum capacitances. We expect other members of the TMD class to be equally suitable as infrared transparent top gates due to their similarity, while their scalability via CVD growth allows for easy device integration[179–182]. This work paves the way for future cryogenic near-field experiments on exotic states in dual-gated sample geometries[81–83,157,158].

6. Development of a cryogenic near-field optical microscope

In this Chapter, we introduce a cryogenic near-field microscope, encompassing a commercially available system with several modifications. We discuss the technological challenges in the development of this system, which includes the operation of AFM in vacuum, and the passive and active vibration isolation schemes. We conclude the Chapter by demonstrating its performance.

With near-field optical microscopy proven itself as a robust and versatile technique[183], interest has grown to bring s-SNOM to a cryogenic environment. Several challenges are to be faced, such as operating an AFM in vacuum and thin layers freezing on the sample surface in cold environments. In 2013, the first home-built cryoSNOM was capable to operate down to 20 K[184], studying the insulator-metal transition in VO_2 and V_2O_3. A few years later, more systematic mapping of the insulator-metal transition in V_2O_3 showed reliable operation of their home-built system[185]. In 2018, the same group reported on the fundamental limits of plasmon propagation in graphene, using s-SNOM at 60 K[112]. Both cryogenic s-SNOM systems only cool the sample, while leaving all the surrounding objects at room temperature. Despite such design giving a partial simplification of operation, it limits the base temperature to $\approx$ 20 K. To overcome the issue of ice-deposition on the sample, the latter system works in ultra-high vacuum, severely complicating modifications to the system.

The acquisition of neaspec by attocube in 2014 brought s-SNOM and cryogenics expertise together. Based on the attoDRY800 cryostat and the neaSNOM platform, they developed a commercial cryogenic s-SNOM system: cryo-neaSNOM. In this section, we give an introduction to this system, and discuss the two foremost challenges of such systems: operation of AFM in vacuum, and the passive and active vibration isolation schemes. To demonstrate the performance we present noise figures and an example of hBN phonon-polaritons measured at 10 K.

6.1. Description of cryo-neaSNOM

The cryo-neaSNOM uses a radically different design by employing a closed-cycle helium cryostat, as opposed to the previously mentioned home-built systems that require a constant consumption of liquid helium. This different approach facilitates a constant and robust operation with a base temperature of 5.5 K, but comes at the cost of relatively strong mechanical vibrations of several micrometres induced by the cryocooler[186]. However, proper vibrational isolation of the attoDRY800 cryostat from the optical table minimizes these vibrations to the order of nanometres[187].

Figure 6.1 shows a front-view of the system as installed at ICFO. While the near-field detection scheme is the same as outlined in Sec. 2.2, there are several notable differences. With the attoDRY800 cryostat sitting below the optical table, the vacuum chamber leaves sufficient space on the optical table for the interferometric detection unit and a movable hood hosting the optics for AFM detection. We place on the corners of the optical table two masses used for active mechanical stabilization of the optical table as we discuss later.

Inside the system, we find a relatively compact structure forming the core of our system, as displayed in Fig. 6.2. The sample, AFM tip and parabolic mirror can be independently moved using cryo-compatible stacks of x,y and z positioners. Additional xy and z scanners are placed underneath the sample to facilitate raster-scanning during measurements. These three towers of positioners are placed on a frame that rests on four small springs, which passively damp the vibrations from the cold plate below. Since these springs are rather stiff, we have to ensure the frame resting on it finds its ‘relaxed’ position each time an AFM tip or sample is exchanged. To do so, we move the parabolic mirror to the side, allowing a red pilot laser to reflect on the flat part of the parabolic mirror. By gently tapping the structure, we verify that the backreflected light coincides with an iris. Two heaters

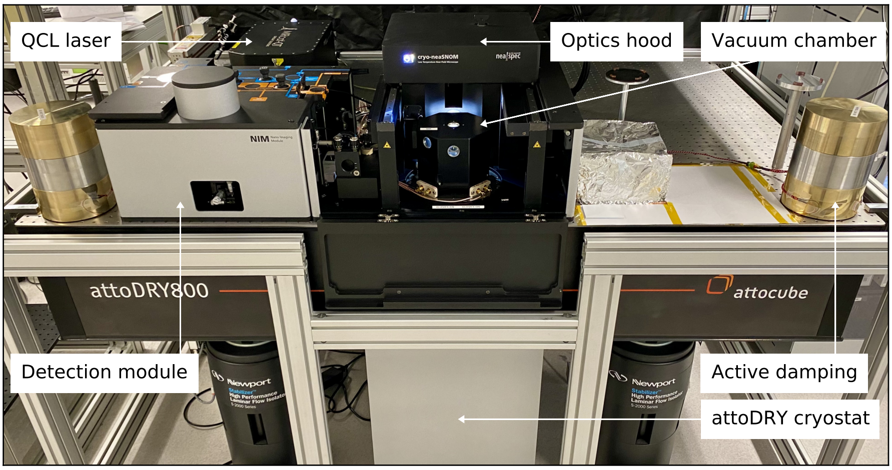

Figure 6.1: cryo-neaSNOM as installed in ICFO. Front view of the system with most important elements labelled. The two masses on the corners are placed in line with the vacuum chamber and form part of the home-built active vibration isolation system.

provide independent temperature control of the sample and AFM tip. For achieving proper vacuum levels, coils with fabric immersed with activated charcoal act as cryopumps when the system is cold, while a cold shield maintained at ≈ 40 K covers the complete inner structure and captures any molecules released from the vacuum shroud. This brings the pressure down to $\approx 5 \cdot 10^{-6}$ mbar with the system at base temperature. However, since this is measured underneath the optical table and far from the cryopumps, we estimate that the actual pressure near the sample is about one order of magnitude lower, effectively bringing it close to an ultra-high vacuum environment. This is in line with the fact that we do not observe any ice growth on the sample, provided we keep the system in a proper vacuum state at all times possible. A variation of this system is also used for quantum optics experiments[188].

6.2. AFM operation in vacuum

One of the central challenges of such system is the AFM operation in vacuum conditions. The tight space in the chamber complicates a practical but efficient solution for cantilever excitation, while at the same time one also has to deal with the greatly enhanced quality factor due to the lack of air damping. Since we operate the AFM in tapping mode, we have to excite the cantilever motion with a dither, which is usually a piezoceramic element attached to the holder of the AFM tip. By driving the dither element with an oscillating voltage at the cantilever resonance, the tiny deformations of the piezoceramic material induce vibrations in the nearby holder, sufficient to excite the cantilever resonance.

In the original configuration of the cryo-neaSNOM, the dither is placed on the side of the AFM tip holder, facilitating a simple exchange of the AFM tip (Fig. 6.3a). However, we found that this is a very ineffective way of driving the cantilever, as is apparent in the mechanical spectrum of the cantilever. Figure 6.4a displays the spectrum recorded in ambient conditions, showing a large number of resonances but making it unclear what the

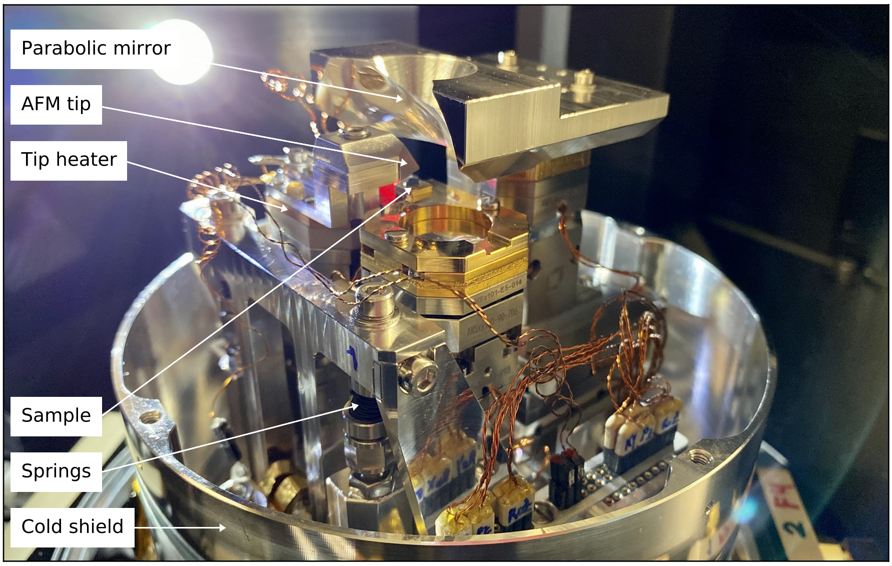

Figure 6.2: Inner structure of the cryo-neaSNOM. The parabolic mirror, sample and AFM tip are each mounted on a tower of nanopositioners, which together sit on a structure resting on springs.

actual resonance of the tip is. Only in vacuum the main cantilever resonance becomes visible (Fig. 6.4b), however many additional resonances remain. As we will discuss later, any nearby resonances interfere and prohibit stable performance when we artificially broaden the main resonance intending to obtain a more stable AFM operation. Thus, a clean mechanical spectrum is of pivotal importance and exhibits ideally only one resonance.

In order to understand what causes many resonances to appear in the cantilever spectrum, we devise a modified excitation scheme as shown in Fig. 6.3b. Instead of the dither element placed on the side of the tip holder, we glue a small piezoceramic element slightly above the AFM tip. Besides this location being much close to the cantilever, it also allows for inducing vibrations along the same direction as the cantilever motion. The recorded mechanical spectrum clearly indicates a much more effective excitation, as shown by the sole presence of the main resonance in Fig. 6.4a,c. This shows the importance of aligning the directions of motion of the dither and cantilever, which, in the case of perpendicular alignment, leads to a weak excitation of the main resonance whilst strongly coupling to unwanted resonances. As alternative route to this piezoacoustic excitation we suggest a photothermal excitation scheme, where a modulated light beam sets the cantilever into motion avoiding any resonances of the tip holder[189].

Equally important is to drive the cantilever at an optimum Q-factor, defined by $f/\Delta f$ with f as the resonance frequency and Δf as the full-width half-maximum bandwidth of the squared tapping amplitude. To allow for faster feedback and thus less degradation of the AFM tip, it is beneficial to reduce the Q-factor. Standard silicon AFM tips have a Q-factor $\sim$ 1000 in ambient conditions, yielding satisfying performance. However, upon changing to a vacuum environment this value shoots up to $10000 - 20000$ (Fig. 6.4), far above what is suitable for our experiments. In order to reduce the effective quality

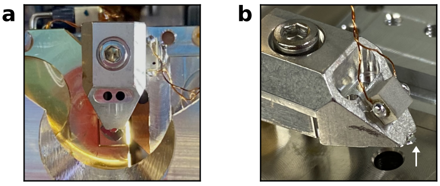

Figure 6.3: Dither placement for cantilever excitation. **a** Top view of the AFM tip holder in the original design of the cryo-neaSNOM, with the dither placed on the right side of the AFM tip holder. **b** In our adapted configuration we glue the dither on top of the AFM tip holder, with a layer of cigarette paper in between to prevent shorting the dither to the holder. The white arrow points at the cantilever.

factor in vacuum environment, we feed the dither with an out-of-phase signal. This is an established technique dubbed as Q-control, where the recorded tip motion is fed into a circuit shifting the phase by $\pi/2$ and adding this contribution with a certain gain factor to the original drive voltage[190,191]. As depicted in Fig. 6.5, this built-in feature of the system brings the Q-factor easily down by more than an order of magnitude. This artificial way of reducing the quality factor shows the importance to have a clean spectrum in the first place, since any nearby resonances can actually be amplified by the out-of-phase signal. We would like to point out that a thicker PtIr coating also helps to reduce the Q-factor slightly[192]. For this reason, we prefer to use a 50 nm coated tip in the cryoSNOM, rather than the 25 nm coated tips used in the room temperature s-SNOM system. We finally note that in most cases we make use of the tip heater and keep the AFM tip at room temperature while the system is cold. Although this brings the base temperature of the system from 5.5 K up to 10.5 K, it makes the operation of the AFM much more reliable, as the cantilever spectrum tends to change substantially when cooling down the tip.

6.3. Vibration isolation strategy

For proper operation of the cryoSNOM it is essential to minimize the vibrations in the system. In particular the tip-sample distance variations over time should in the ideal case not exceed $\approx$ 1 nm, since the near-field signal is strongly affected by such variations (Fig. 2.7b). However, placing the system on a non-rigid structure, such as springs, allows for rotational freedom that disturbs the alignment conditions presented in Sec. 2.3. Therefore, finding the optimum configuration is not a trivial task. To understand the details of this aspect, we first give an overview of the apparatus' features and what can be adjusted, after which we discuss the actual measured vibrations, and to finish by presenting a novel active damping scheme.

The attoDRY800 system is designed to minimize the transmission of floor vibrations to the surface of the optical table, as well as to reduce the impact of the cryocooler pulses. To this end, the system consist of an optical table and a cryostat that is resting on the lab floor (Fig. 6.1). Flexible thermal links from the cryostat to the inner structure of the cryoSNOM provide a weak mechanical connection. However, we suspect that the flexible vacuum bellow passes most of the vibrations to the surface of the optical table.

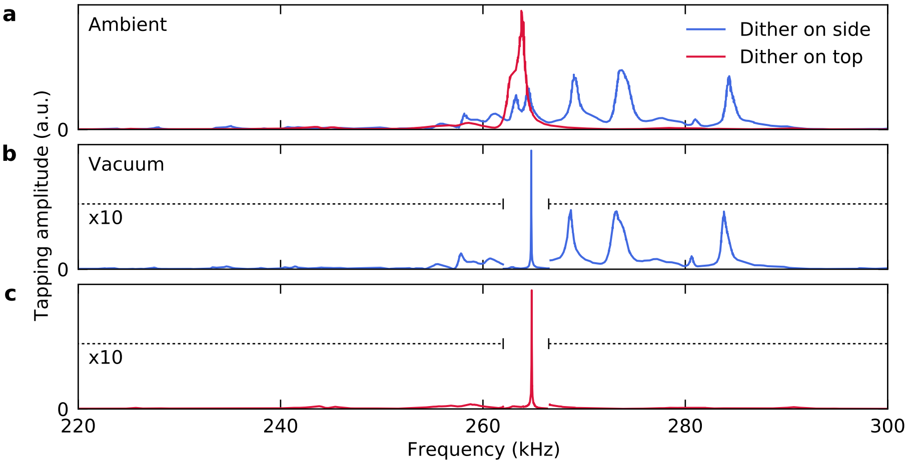

Figure 6.4: Mechanical spectrum of the AFM cantilever. **a** The recorded tapping amplitude as function of excitation frequency in ambient conditions does not exhibit a clear resonance with the dither placed on the side, while placing the dither on top of the holder recovers the cantilever resonance. **b,c** In vacuum (10^{-2} mbar), the main resonance is clearly visible for both configurations, although many additional resonances remain when placing the dither on the side. The same AFM tip was used for all spectra.

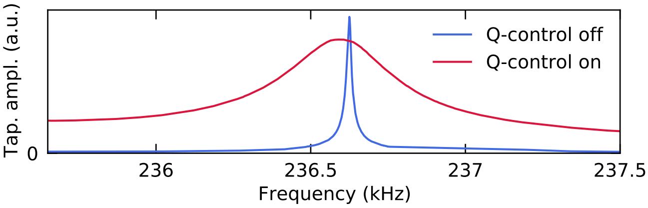

Figure 6.5: Artificially damping the cantilever resonance. By turning on Q-control, we reduce the Q-factor of the cantilever resonance from $Q \approx 18000$ to $Q \approx 790$.

Especially its mechanical spectrum with resonances between 200-300 Hz allows for easy transmission of the cryocooler pulses with a similar spectrum. At the cold plate, just below the inner structure shown in Fig. 6.2, these pulses appear at a repetition rate of 1 Hz with a peak-to-peak amplitude ≈ 10 nm[188].

To further bring down these vibrations, the system is equipped with four springs on which the inner frame is resting, as shown in Fig. 6.2. To estimate the mechanical isolation this provides, we calculate the amplitude transmission function according to a damped harmonic oscillator. Following Ref. 193, for a given frequency f the transmission function is

$$T(f) = \sqrt{\frac{1 + \frac{1}{Q^2}(\frac{f}{f_0})^2}{(1 - (\frac{f}{f_0})^2)^2 + \frac{1}{Q^2}(\frac{f}{f_0})^2}}, \tag{6.1}$$

with f_0 as the effective resonance frequency, and the quality factor Q approximating $T(f_0) \approx Q$.

Figure 6.6 depicts the transmission function for $f_0 = 16$ Hz, corresponding to the

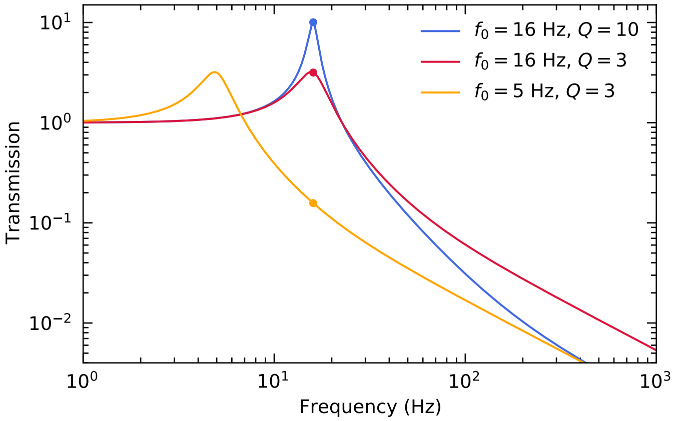

Figure 6.6: Transmission function of a damped harmonic oscillator. Below the spring resonance, a spring acts as a low-pass filter. On resonance any incoming vibrations are amplified by Q times, while above the resonance the transmission reduces by $1/f^2$ in the limit $Q = \infty$. In the limit $Q = 1$, the transmission scales with $1/f$. We can reduce the Q-factor of the configuration on springs by increasing the number of magnets that form part of the Eddy-current damping mechanism. The dots indicate the transmission values at 16 Hz for different configurations.

installed springs, as well as for $f_0 = 5$ Hz. In general, one favours a lower resonance frequency, as it provides stronger damping for higher frequencies, further reducing the influence of the cryocooler pulses on the measurements. However, the current version of the cryo-neaSNOM is not designed for springs with a resonance frequency lower than 16 Hz, as it would render the structure too unstable in the horizontal plane. One could overcome this limitation by switching to an inner frame hanging on springs, providing more than an order of magnitude better vibration isolation when shifting f_0 to 5 Hz. Given the space constraints of the cryo-neaSNOM, such configuration with hanging springs is challenging. Nevertheless, following our suggestion, attocube is designing a configuration with a structure hanging on springs given its high potential.

Another aspect that requires careful consideration is the Q-factor of the structure on springs. As shown in Fig. 6.6, a higher Q-factor provides stronger vibration isolation at higher frequencies, but comes at the cost of higher amplification at the spring resonance. To reduce the Q-factor, the apparatus can be equipped with an Eddy-current damping system. Underneath the structure resting on springs, an aluminium cross floats in an array of small permanent magnets. Any motion of the structure gets induces an electrical current in the aluminium, which in turn dissipates the mechanical energy. By choosing the number of magnets, we can adjust the strength of this passive dissipation mechanism, as illustrated by the reduced Q-factor in Fig. 6.6.

The vibrations that we record in the system are eventually determined by the environmental conditions and the applied damping schemes. Due to the lack of basement space, the cryoSNOM is installed on the second floor at ICFO. Any floor not situated at ground level comes with certain floor resonances, which for our laboratory turns out to be at 16 Hz. This is an unfortunate coincidence with the spring resonance frequency (as discussed above), challenging the performance of our system. Figure 6.7a presents

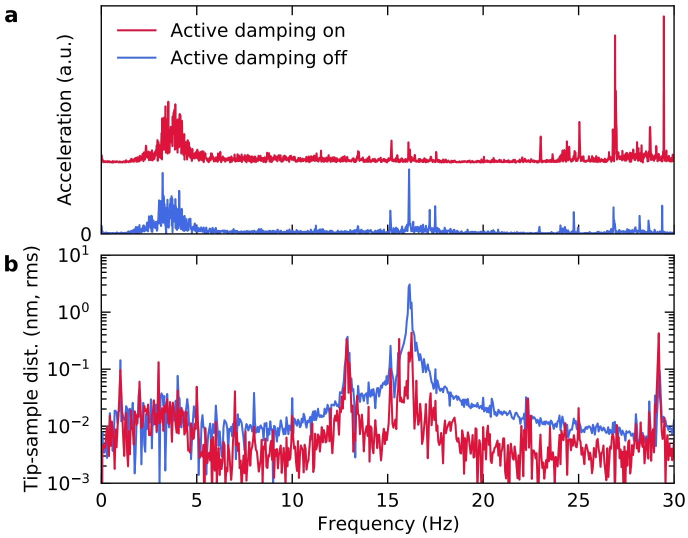

Figure 6.7: Vibration spectra of the cryoSNOM. a Acceleration spectrum measured on the surface of the optical table (on a linear scale). The trace with active damping turned on is offset for clarity. The broad peak centred around 4 Hz corresponds to the table resonance, while the sharp peak at 16 Hz is due to the strong floor resonance. **b** Spectrum of the tip-sample distance measured via contact-mode AFM at $T = 10$ K. The broad resonance at 16 Hz corresponds to the spring resonance, and is excited by the floor resonance. By turning on our active damping system, we are able to strongly reduce the vibrations at 16 Hz on the optical table and inside the cryoSNOM.

the measured vibration spectrum on the surface of the optical table, as recorded with an accelerometer (TableStable VA-2C). A more suitable way to characterize the vibrational noise is to measure the tip-sample distance using contact-mode AFM, shown in Fig. 6.7b. This provides elemental information that is easy to interpret, as compared to the noise in tapping amplitude. We find that the dominating instability comes from the structure wobbling on springs at 16 Hz, with amplitudes (rms) of several nanometres. We note that the rms values in Fig. 6.7b and Fig. 6.8 are defined as the square root of the power spectrum, such that a peak in the amplitude spectrum with magnitude 1 corresponds to an oscillation in time with peak-to-peak amplitude $2\sqrt{2}$.

To diminish the strong mechanical vibrations at 16 Hz, we considered several solutions. This includes a structure hanging on springs with a lower resonance frequency, the installation of a tuned-mass damper to damp the floor resonance and the installation of an actively damped platform on which the complete system is placed. However, since these proposals have practical drawbacks or would require too much time, we designed and built our own active damping system, which turns out to be rather effective at counteracting the most severe vibrations.

The idea of our active damping system naturally follows from Newton's third law: action = −reaction. It consists of a 30 kg mass placed on three piezoceramic actuators (PI Ceramic), shown in Fig. 6.1. By applying a voltage to these actuators, they lift the masses on top of them, while at the same time pushing the optical table down. By placing two of such moving masses in line with the vacuum chamber and driving them with the appropriate oscillating voltage, we can counteract the vibrations on the side of the optical table where it matters. The 16 Hz vibration, measured on the optical table, has a typical acceleration of ≈ 200 µm/s^2 $= 20$ µg and displacement of ≈ 20 nm. Some simple considerations show that typical piezoceramic actuators are very capable of generating sufficiently large forces, provided we avoid operation near their resonance frequency ~ 1500 Hz (including masses on top). We choose rather flat actuators (10x10x2 mm^3) avoid damaging them when placing the masses on top, and use an amplifier meant for driving a high capacitive load (Piezosystem Jena 30V300). An accelerometer (TableStable VA-2C) picks up the vibrations on the floor, which we pass through multiple digital filters (Red Pitaya STEMlab 125-14) acting as a strong bandpass filter centred at 16 Hz. At the same time, we fine-tune the gain and phase of the outgoing signal for optimum cancellation of the vibrations on the optical table. This configuration allows counteracting vibrations only at one specific frequency, due to the strong phase dispersion with frequency of the output signal. A consequence is that some resonances between $25 - 30$ Hz are actually being amplified, as seen in Fig. 6.7a. However, since the springs provide adequate damping at those frequencies, this does not pose any problem.

After trying out various configurations of the damping scheme, we chose to use limited Eddy-current damping. In this way, we benefit from stronger vibration isolation at higher frequencies, while the active damping scheme still effectively reduces the vibrations at 16 Hz.

6.4. Performance of the cryo-neaSNOM at ICFO

To evaluate the performance of our cryoSNOM, we collect noise spectra of the topography and near-field amplitude and phase, shown in Figure 6.8. To obtain these spectra we park the AFM tip at a fixed location on our sample and record the topography and near-field signals for a period of about 10 seconds at a readout rate of 300 Hz, and subsequently take their Fourier transforms. In addition to the spectra, we calculate the rms noise value for the typical integration time of 10 ms used in our experiments, as shown inside the figure panels. We note that these amplitude rms values are defined by an integral $\sqrt{\int_0^{f_{\text{int}}} P_{\text{den}}(f)\text{d}f}$ of the power spectral density P_{den} for a given integration time $1/f_{\text{int}}$. The measured topographic noise can be described by a $1/f$ background with a spike at 16 Hz (Fig. 6.8a). Since there are no harmonics of 16 Hz in the topographic noise, we deduce that the structure on springs follows a harmonic motion. By turning on the active damping mechanism, we bring the rms value down to ~ 200 pm, which is only slightly larger than the typical topographic roughness of hBN substrates[4].

To understand the noise spectrum of the near-field signal, we should realize that not only the tip-sample noise influences this, but also the motion of the structure on springs relative to the optical table strongly affects this. Any rotation of the structure influences the position of the focal point of the parabolic mirror and induces aberrations, both of which change the near-field hotspot at the apex of the AFM tip. This is seen in Fig. 6.8b, showing peaks at harmonics of 16 Hz in the optical signal, which indicates a non-linearity occurring in this process. The presence of these harmonics tells us that the oscillating structure modulates the optical signal in an asymmetric fashion. Since a simple Gaussian beam should lead to an even response, this indicates an imperfection in focussing the light that leads to aberrations.

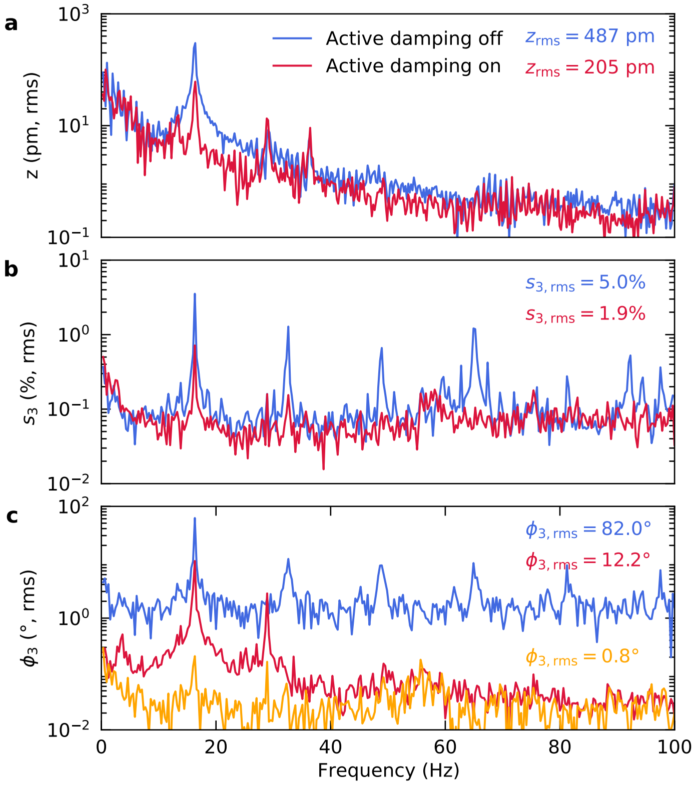

Figure 6.8: Performance figures of the cryo-neaSNOM at ICFO. **a** Topographic noise spectrum consists of a $1/f$ background noise with prominent peak at 16 Hz. **b** Noise-to-signal spectrum of the near-field amplitude shows a rather flat response with multiple peaks at harmonics of 16 Hz when the active damping is turned off. **c** Noise spectrum of the near-field phase shows a considerable improvement once the active damping is turned on. Further reduction of noise is achieved by post-processing the data with a phase-correction algorithm developed by neaspec. All data in this figure were acquired with the system in vacuum (10^{-2} mbar) at room temperature. Only for the topographic noise, the cryocooler was temporarily turned on. The near-field noise spectra were obtain at a wavelength of 10.2 μm with a power of 4 mW. The rms values shown in the panels correspond to a bandwidth of 100 Hz, equivalent to an integration time of 10 ms.

On the other hand, any translation of the structure on springs only influences the measured near-field phase signal. Since the laser beam remains parallel to the axis of the parabolic mirror under a translation, it only induces an expansion or contraction of the arm length of the interferometer, which we measure as a change in the optical phase (Fig. 2.5). From the strong phase noise as plotted in Fig. 6.8c, we can actually estimate the extent of the translation of the structure parallel to the laser beam. Assuming that all the phase noise at 16 Hz can be attributed to this translation, it would convert to an rms amplitude of ~ 1 μm in the case without active damping. This is brought to levels that are more acceptable by switching on the active damping, reducing this figure by almost an order of magnitude. The final step of phase noise reduction is done using a patented algorithm by neaspec, which effectively uses the far-field information to compensate for the near-field phase noise induced by a translational motion of the structure on springs. This algorithm is able to reduce the rms noise value to below 1°, setting the cryo-neaSNOM on par with the room temperature neaSNOM.

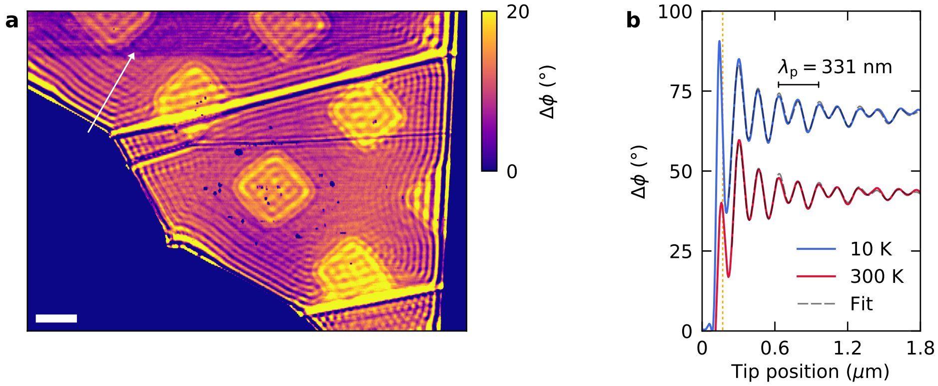

Figure 6.9: Inauguration scan measuring hBN-phonons at 10 K. a Near-field phase contrast of an isotopically pure hBN flake placed on top of a square grid. The fringes running parallel to the edges and height steps of the flake correspond to hyperbolic phonon-polaritons. The excitation energy is 182 meV and the scale bar is 800 nm. **b** Line cut along the white arrow in panel **a**. The oscillations in the near-field phase signal are formed by edge-launched phonons (λ_p period) and tip-launched phonons ($\lambda_p/2$ period), both of which we include in the fit. The dotted orange line corresponds to the edge position of hBN. The near-field signal corresponds to the third harmonic of the tapping frequency of the tip.

We finally demonstrate the performance of our cryoSNOM on an actual sample consisting of a flake of isotopically pure hBN. This purified form of hBN hosts hyperbolic phonon polaritons with a longer lifetime than occurring in naturally abundant hBN crystals[194]. Figure 6.9 depicts the recorded optical near-field contrast, measured at a temperature of about 10 K. We observe a plenty of fringes running across the flake, which we can interpret in a similar fashion as the plasmon polaritons discussed in Sec. 2.4. Fig. 6.9 shows a line cut, and by applying the same analysis as before, we can extract a phonon wavelength of 331 nm and a decay length of 2.3 μm. This results in an inverse damping ratio $\gamma^{-1} = 43.5 \pm 1.7$, which is considerably larger than $\gamma^{-1} = 32.5 \pm 1.2$ found at room temperature. Recent work attributes this to reduced acoustic phonon scattering[195].

7. Imaging broken inversion symmetry in magic-angle twisted bilayer graphene

In this Chapter, we study magic-angle twisted bilayer graphene closely aligned to the underlying hBN substrate. By means of cryogenic photovoltage nanoscopy, we reveal a structure of large-scale spatial modulations in the photovoltage maps. Guided by electronic transport measurements, we interpret it as a manifestation of a second-order superlattice formed by the underlying moiré lattices, which provides a direct view of the broken inversion symmetry in our sample.

Superlattices are formed when superposing two lattices at a small twist angle, or when they have a slight lattice mismatch. While this was a known effect occurring in rotated graphite sheets[196], it was first demonstrated in two-dimensional materials using twisted graphene layers[21] and graphene aligned to hBN[197,198]. Such moiré lattice leads to an underlying periodic potential which has been predicted to create additional Dirac points[199,200], as indeed observed soon after the realization of an hBN-graphene superlattice[201]. This leads to interesting phenomena, such as a recursive energy spectrum under the application of an external magnetic field, known as the Hofstadter's butterfly[10–12]. More recently, after the discovery of superconductivity in magic-angle twisted bilayer graphene (MATBG), a new field emerged leading to the observation of superconducting, topological and correlated phases in MATBG and its relatives[18,22–31].

The process of forming a superlattice can repeat itself when two superlattices form a second-order superlattice with an even larger periodicity. To allow such large-scale interference pattern, the superlattice periodicities need to be similar. Coincidentally, the superlattices of hBN-graphene and MATBG differ only by a few percent in their periodicities, which are close to 14 nm. Thus, when the twist angles between hBN and graphene layers are tuned correctly, such second-order superlattice should emerge. When this happens, MATBG will be subject periodic potentials with a different periodicity: those that are generated by the hBN-graphene superlattice and the second-order superlattice. In turn, this breaks the inversion symmetry in MATBG. This is of great interest, as broken inversion symmetry, in combination with broken time-reversal symmetry, facilitates the emergence of ferromagnetism in MATBG[202,203]. In transport experiments, this is manifested by the anomalous Hall effect[25,26,204], which, unexpectedly, was also observed in non-aligned hBN MATBG[205]. In the latter case, strong Coulomb interactions are held responsible for the required inversion symmetry breaking, which suggests that the hBN-alignment enhances the interaction strength in MATBG.

To the best of our knowledge, a second-order superlattice consisting of MATBG has not yet been observed in real-space. Thus far, only transport signatures confirmed the close alignment of MATBG to hBN[25,26], while others studied the second-order superlattice formed by graphene aligned to two hBN sheets[206–208]. Here, we present a combination of cryogenic transport and near-field photovoltage measurements, which we believe manifest a real-space observation of the second-order superlattice in MATBG aligned to hBN, providing a direct view of the broken inversion symmetry in MATBG.

7.1. MATBG device with graphene and hBN closely aligned

In this work, we used a TBG device made by Petr Stepanov following the usual fabrication steps outlined in Sec. 2.1. The device consists of TBG encapsulated in 16 nm bottom hBN and 10 nm top hBN flakes, altogether placed on top of a graphite flake, serving as local gate. During the stacking procedure, the graphene flake is cut with an AFM tip, with the intention to prevent additional strain building up in the tear-and-stack process used otherwise[51,54,209]. To minimize the number of bubbles in the stack, we pick up each flake at a temperature within 100 − 110 °C[100,101]. In the final step, when dropping the stack on the target substrate with alignment markers, we repeat the drop-down step at least once to further squeeze out any bubbles. Figure 7.1a shows an AFM scan of the resulting

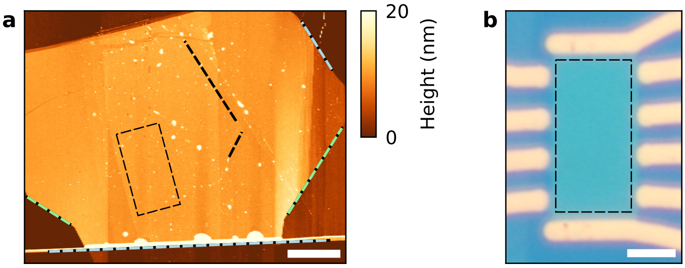

Figure 7.1: Close alignment of graphene and hBN sheets in our device. **a** AFM image of our stack with the relative alignment of the upper graphene sheet (black), top hBN flake (blue) and bottom hBN layer (green). We extract angles of $\approx 0.5°$ ($5.0°$) between the crystallographic axes of the top (bottom) hBN sheet and upper graphene layer. The rectangle marks the region where the Hall-bar is patterned and the scale bar is 8 µm. **b** Optical image of our device after nano-fabrication, patterned in a Hall-bar shape. The electrical contacts are gold-coloured, and the scale bar is 4 µm.

stack. We choose the cleanest area of the stack to pattern our device in a Hall-bar shape (Fig. 7.1b).

We can obtain an estimate of the relative alignment of the graphene and hBN sheets by comparing their crystallographic axes. Each flake features multiple straight edges in the AFM scan, which correspond either to the zigzag or armchair direction. Based on two such edges for each flake, we find that the upper graphene sheet is misaligned to the top (bottom) hBN flake by $\approx 0.5°$ ($5.0°$). Since we cannot distinguish between zigzag and armchair directions, there is a probability of 50% that the layers are actually in close alignment, rather than being rotated by $\sim 30°$. Raman spectroscopy can give decisive answer to this ambiguity[210]. We note that the relative orientations between the flakes can change slightly during the subsequent nano-fabrication steps. However, the following measurements indicate this did not happen.

7.2. Electronic transport signatures of two coexisting superlattices

We first characterize our device with transport measurements performed at temperatures T starting at 5 K and above, shown in Figure 7.2a. A Hall measurement at a magnetic field of ≈ 1 T provides the calibration of the carrier density $n(V_\mathrm{G})$ to the applied gate voltage V_G. We measure the longitudinal four-probe resistance between the four side contacts in the lower part of our device and identify a series of resistive states. In addition to the usual resistance maximum at charge-neutrality, we find three smaller peaks and a peak marked by the black arrow, which are all are equidistant to each other. Furthermore, we identify a nearby peak at slightly higher carrier density, marked by the red arrow. This maximum seems to coincide with a shoulder seen at opposite carrier density. These resistive states disappear upon increasing the temperature.

These transport data suggest that our sample hosts two moiré lattices: one given by graphene aligned to hBN, and another one owing to twisted bilayer graphene (TBG). Such moiré lattices are known to exhibit a resistive state at a particular carrier density

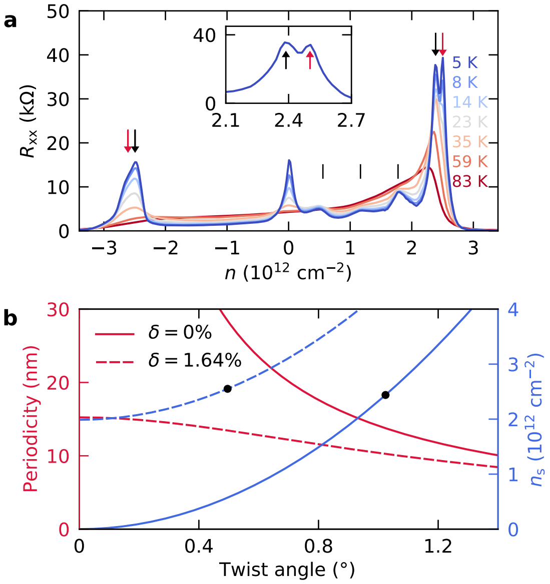

Figure 7.2: Electronic transport signatures of superlattice-induced insulating states. **a** Longitudinal resistance for a range of temperatures, measured between the four side contacts in the lower part of our device. At 5 K we identify multiple resistive states: at charge neutrality, at intermediate filling factors (vertical marks) corresponding to the full-filling state of TBG (black arrows), and an additional peak at slightly higher carrier density attributed to the fulling-filling state of the hBN-graphene superlattice (red arrows, for negative n it appears as a shoulder). Inset: zoom of the two nearby full-filling states. **b** Lattice constant of a moiré lattice (red lines), calculated from Eq. (7.2) for two different values of the lattice mismatch δ. For TBG, $\delta = 0\%$, while we assume a mismatch of 1.64% between the hBN and graphene sheets, limiting the moiré periodicity to ≈ 15 nm at perfect alignment. Blue lines plot the corresponding full-filling carrier density. From this graph, we can relate the two nearby peaks seen in panel **a** to two superlattices: two graphene layers twisted at $\approx 1.02°$ (≈ 13.8 nm periodicity) and graphene on hBN twisted at $\approx 0.5°$ (≈ 13.5 nm periodicity).

associated with the full-fulling state of the superlattice[15,201]. For a superlattice formed by two superposed hexagonal lattices, this full-filling carrier density n_s is given by[201]

$$n_s = \frac{8}{\sqrt{3}\lambda_M^2}, \tag{7.1}$$

where the twist angle θ and lattice mismatch δ define the superlattice periodicity λ_M as

$$\lambda_M = \frac{(1+\delta)a}{\sqrt{2(1+\delta)(1-\cos\theta)+\delta^2}} \tag{7.2}$$

with $a = 0.246$ nm corresponding to the graphene lattice periodicity. Figure 7.2b depicts both functions for zero and finite lattice mismatch. It shows that a larger twist angle reduces the area of the moiré unit cell and increases the density of carriers in the system at the full-filling state, defined by 4 carriers per unit cell. The properties of TBG are reflected by the curves with $\delta = 0\%$, while we model hBN-graphene superlattice with $\delta = 1.64\%$.

This value is slightly lower than the value typically stated in literature, $\delta = 1.8\%$, however, we will see that a small strain in the graphene layer of $\approx 0.1\%$ can account for this difference.

Because the three intermediate resistive states only occur for MATBG samples[22], and since they are equidistant to the resistance peak marked by the black arrow, we identify this maximum as the full-filling state of TBG. We determine the corresponding n_s as half the distance between the peaks at opposite carrier density (black arrows) to account for a slight offset with respect to charge-neutrality. This yields $n_s \approx 2.44 \cdot 10^{12}$ cm^{-2} and from Fig. 7.2b we read out that it corresponds to a twist angle $\theta_{\mathrm{TBG}} \approx 1.02°$ and a moiré periodicity of ≈ 13.8 nm (black dot). As a consequence, we attribute the resistance maximum marked by the red arrow as the full-filling state of the hBN-graphene superlattice, with $n_s \approx 2.55 \cdot 10^{12}$ cm^{-2}. This relates to a twist angle $\theta_{\mathrm{hBN}} \approx 0.50°$ with a superlattice periodicity of ≈ 13.5 nm. Guided by the close hBN-graphene alignment seen in the AFM scan, we excluded the possibility of TBG hosting two regions with a different twist angle. Since we observe resistive states at integer filling factors, and $\theta_{\mathrm{TBG}} \approx 1.02°$, we consider our device to be a magic-angle TBG sample. Future transport measurements at lower temperature could verify the existence of superconductivity in this device.

A consequence of graphene being in close alignment to hBN is the enhanced gap size Δ of graphene at charge neutrality. This is a known effect in single-layer graphene, with a gap of 14 meV probed with photocurrent spectroscopy[211]. A more common approach measures the thermal activation of the gap via $R_{xx} \propto e^{-\Delta/2k_B T}$, which has been determined to be as large as ≈ 25 meV[12,212] for single-layer graphene. In MATBG this gap was found to be ≈ 0.86 meV for a non-aligned sample[24], while a sample with $\theta_{\mathrm{hBN}} \approx 0.6°$ featured a gap of ≈ 5.8 meV[26]. In our sample we extract a thermally activated gap at charge-neutrality of ≈ 3.6 meV, which indeed suggests that graphene is in close alignment to hBN.

7.3. Second-order superlattice probed with near-field photovoltage nanoscopy

We continue our quest by performing cryogenic near-field photovoltage nanoscopy on our sample. This technique has proven to be a sensitive probe of spatial changes in the electronic structure of the material under study (see Chapters 4,8 and Refs. 93,96,155). In brief, it consist of a hotspot of light at the apex of an AFM tip that injects heat into the material with nanoscale precision. In turn, this heat is converted via different pathways to a measurable current or voltage, which can be read out at the contact electrodes. In graphene, the predominating mechanism generating such photovoltage is the photothermoelectric effect (PTE)[123]. Throughout the measurements shown in this Chapter, we illuminate the AFM tip with infrared light with an energy of 116 meV and an average power of ≈ 5 mW. To avoid detecting unwanted far-field photovoltage contributions, we record the signal at the second harmonic of the AFM cantilever frequency. The magnitude of the detected signals are within the range $0.01 - 1$ µV. Details on this method are given in Section 2.5, and Chapter 6 describes the system we use for the measurements presented here.

Figure 7.3 shows spatial images of the recorded photovoltage V_{PV} in our sample at temperatures between 10 K and 70 K with n close to charge-neutrality. We observe a pattern of fringes running across the complete sample with small variations in their

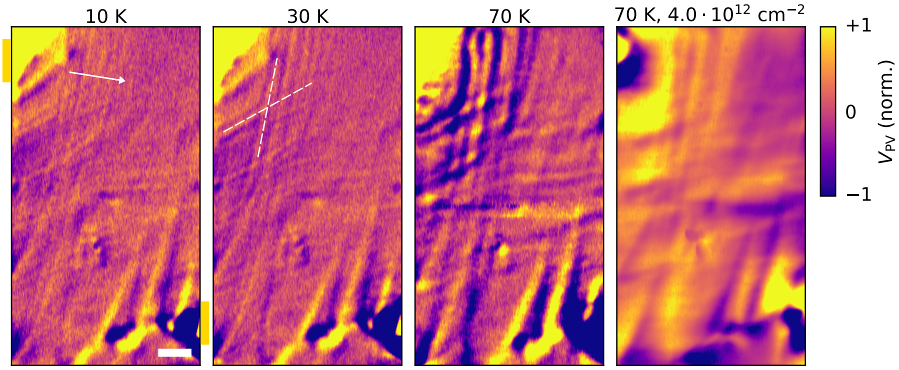

Figure 7.3: Visualizing broken inversion symmetry in magic-angle twisted bilayer graphene. Near-field photovoltage maps of our device at different temperatures within the dashed area marked in Fig. 7.1**b**. We observe fringes with a periodicity $\sim$ 500 nm running across the entirety of the sample along two direction at a relative angle of $\sim 50°$ (two dashed lines). Slight variations in the periodicity and directions occur, notably in the bottom right corner with the periodicity exceeding 1 µm. These features remain unchanged at elevated temperatures, except for an increase in the measured response. All scans are performed with $V_G = 0$ V, thus being close to charge neutrality, except for the rightmost scan, which is taken with the Fermi level within the remote bands. In that scan, we observe a global sign reversal and an increased cooling length that causes fine details seen in the other scans to become obscured. The relative positions of the contacts used to read out the photovoltage are indicated in gold, and the upper contact grounds the device (Fig. 7.1**b**). The excitation energy is 116 meV and the scale bar is 1 µm. We choose the colour map such to emphasize the small modulations in the measured photovoltage. It covers the same range for all scans, except for a 16x larger range in the rightmost scan.

periodicity and direction with position. Qualitatively, this pattern does not alter upon increasing the sample temperature and we only see a gain in magnitude above 30 K. Even at room temperature, we find faint signatures of the same pattern, although with a strongly reduced magnitude (not shown here). We use the other tuning knob, the carrier density, to bring the Fermi level well inside the remote band (right panel). In that case, whilst the average photovoltage response increases by an order of magnitude, we visually identify the same underlying pattern. Since photovoltage nanoscopy is sensitive to gradients of the Seebeck coefficient parallel to the current flow, we simultaneously recorded the generated photovoltage across a different pair of contacts. We find that the fringes light up in different regions, but do not change in their underlying properties (Sec. 7.5). In fact, the presence of Seebeck gradients across the complete sample serves a probe of the global current flows within the sample. Lastly, we performed simultaneously s-SNOM and recorded the optical scattering amplitude and phase. The scattering signals do not reveal any features correlating with the modulations seen in the photovoltage response. As s-SNOM is mostly sensitive to local absorption changes and collective excitations, this suggests that features we probe reflect fine modulations on the local electronic structure, which are more easily picked up with photovoltage nanoscopy[93,125,155].

We can describe the observed pattern in the majority of the sample with two sets of parallel fringes coexisting in two directions. We take a line cut across a set of fringes, shown in Fig. 7.4, and find a common periodicity ≈ 480 nm across the different scans. At 70 K, the profile changes slightly and features a larger-scale modulation at double the periodicity. Nonetheless, the ≈ 480 nm periodicity remains there. Likewise, upon changing the excitation energy within $105-120$ meV we do not observe any change in the measured periodicity. Yet, the periodicity is not constant throughout the sample, as is evident from the bottom-right corner exhibiting modulations exceeding 1 µm in periodicity. The angle between the two sets of fringes is in the upper part of the sample $\sim 50°$, but does change slightly within the sample.

To interpret these data, we will use the following qualitative approach. With the PTE predominating the opto-electronic response in unbiased graphene, we assume that it is the main effect generating the observed photovoltage. The PTE is sensitive to gradients in the Seebeck coefficient, which reflects spatial changes in the underlying electronic structure. Therefore, within this approach, a periodic modulation in the electronic structure manifests itself by a modulated photoresponse at the same periodicity. Even though we cannot exclude that other mechanisms provide additional contributions to the photoresponse, they should equally well preserve any underlying periodicity if they are sensitive to it. Under the assumption of the PTE, we can explain the enhanced photoresponse seen at 70 K with the Fermi level in the remote bands. The higher mobility of the carriers in the remote band increases the cooling length, which leads to an increased photoresponse, while also obscuring fine details seen at lower temperatures. Likewise, when the sample is undoped, thermally excited carriers at 70 K also lead to a slightly increased photoresponse.

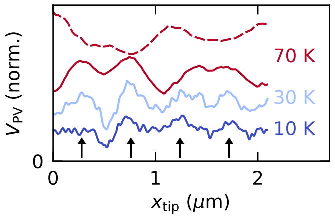

Figure 7.4: Extracting the periodicity of second-order superlattice. Line cut of the photovoltage along the arrow in Fig. 7.3 at three different temperatures. The dashed line corresponds to the scan at finite doping. We extract a common periodicity ≈ 480 nm in the four traces, as indicated by the arrows.

We consider various effects that could cause a periodic spatial modulation of the electronic structure in our sample. For instance, we could imagine the twist angle to be modulated spatially, which would generate a modulated photoresponse according to the model presented in Chapter 8. Scanning magnetometry measurements showed that twist angle variations can exist in the form of domains of similar length scales ($0.1-1$ µm) that host slightly different twist angles[48]. Yet, these twist angle variations do not show the particular structure we observe and, especially, they do not exhibit periodic variations in two direction simultaneously. Another candidate to consider comprises large-scale strain fields, which have been demonstrated to possess a rather strong influence on the local superlattice and electronic structure[40,62,213,214]. However, even in the case of large heterostrain of 1%, the extent of certain directional features remained limited to several TBG moiré unit cells[40]. Therefore, we do not expect strain to directly modify the TBG lattice in an ordered manner across the full device. Alternatively, collective excitations also could give rise to similar features in near-field photovoltage maps[94,95]. However, they should possess a clear dependence on the carrier density and excitation energy, while we find the contrary. Finally, charge puddles near charge-neutrality cause strong spatial modulations in the photovoltage, however, they do not exhibit a distinct periodicity and disappear away from charge-neutrality[93].

As none of these effects account for our observations in transport and photovoltage nanoscopy measurements, we present an alternative interpretation based on the formation of a second-order superlattice induced by the interference of the first-order superlattices. As we will see, all our observations are consistent with this explanation. Therefore, to the best of our knowledge, we believe that we observe for the first time broken inversion symmetry in real space in a MATBG device.

7.4. Formation of second-order superlattice

Our transport measurements suggest that our sample hosts two coexisting superlattices. They are formed by graphene closely aligned to hBN and twisted bilayer graphene, with periodicities of ≈ 13.5 and 13.8 nm, respectively. These two superlattices give rise to a new triangular superlattice with an even larger periodicity, and occurs because the underlying superlattices are closely aligned and have similar periodicities[206–208]. Figure 7.5a shows an example of such second-order superlattice, mimicking the configuration in our sample. An hBN flake (green) has a small lattice mismatch and misalignment with respect to a graphene sheet (red), while a second graphene sheet has only a slight twist (blue). The black triangles provide a guide to the eye to identify the first- and second-order superlattices and show a pronounced change in the relative rotation of the superlattices. This rotation ϕ of a superlattice with respect to the underlying lattices is given by

$$\tan\phi = \frac{\sin\theta}{(1+\delta)-\cos\theta}, \tag{7.3}$$

where δ and θ are the lattice mismatch and twist angle, respectively.

To calculate the periodicity of the second-order superlattice, we represent the real-space lattice (Fig. 7.5a) in reciprocal space. Figure 7.5b shows the lattice vectors $\mathbf{k}$ of the hBN and graphene lattices, from which we take the difference vectors that represent the their first- and second-order superlattices (in red and blue, respectively). The latter features a strongly reduced length and by taking the inverse of its modulus (and accounting for a factor 2π), we find the periodicity $\tilde{\lambda}_\mathrm{M}$ of the second-order superlattice. Figure 7.6a depicts the maximum $\tilde{\lambda}_\mathrm{M}$ along one of the three principal directions for range of θ_hBN and θ_TBG. Since we consider an undistorted triangular lattice, $\tilde{\lambda}_\mathrm{M}$ is equal in each direction. We find a limited window of twist angles where a second-order superlattice emerges, that is, where $\tilde{\lambda}_\mathrm{M} \gg \lambda_\mathrm{M}$. This can be understood in reciprocal space where the superlattice vectors, depending sensitively on δ, θ_hBN and θ_TBG, need to line up precisely with each other. For $\delta = 1.64\%$ and the twist angles extracted from the transport measurements, we find $\tilde{\lambda}_\mathrm{M} \approx 350$ nm, which is slightly lower than the periodicity extracted in the near-field maps.

Whilst this reasonable agreement is encouraging, this minimalistic model of a triangular lattice lacks an explanation for the observation of fringes in only two directions. To account for this, we introduce a small amount of uniaxial heterostrain ϵ to the graphene layers, which is commonly present in these heterostructures[40,62,213]. To this end, we apply the strain tensor $\bar{\epsilon}$ to the graphene lattice vectors[215,216], following $(\bar{I}+\bar{\epsilon})^{-1}\mathbf{k}$, where

$$\bar{\epsilon} = \epsilon \begin{pmatrix} \cos^2\alpha - \rho\sin^2\alpha & (1+\rho)\cos\alpha\sin\alpha \\ (1+\rho)\cos\alpha\sin\alpha & \sin^2\alpha - \rho\cos^2\alpha \end{pmatrix}, \tag{7.4}$$

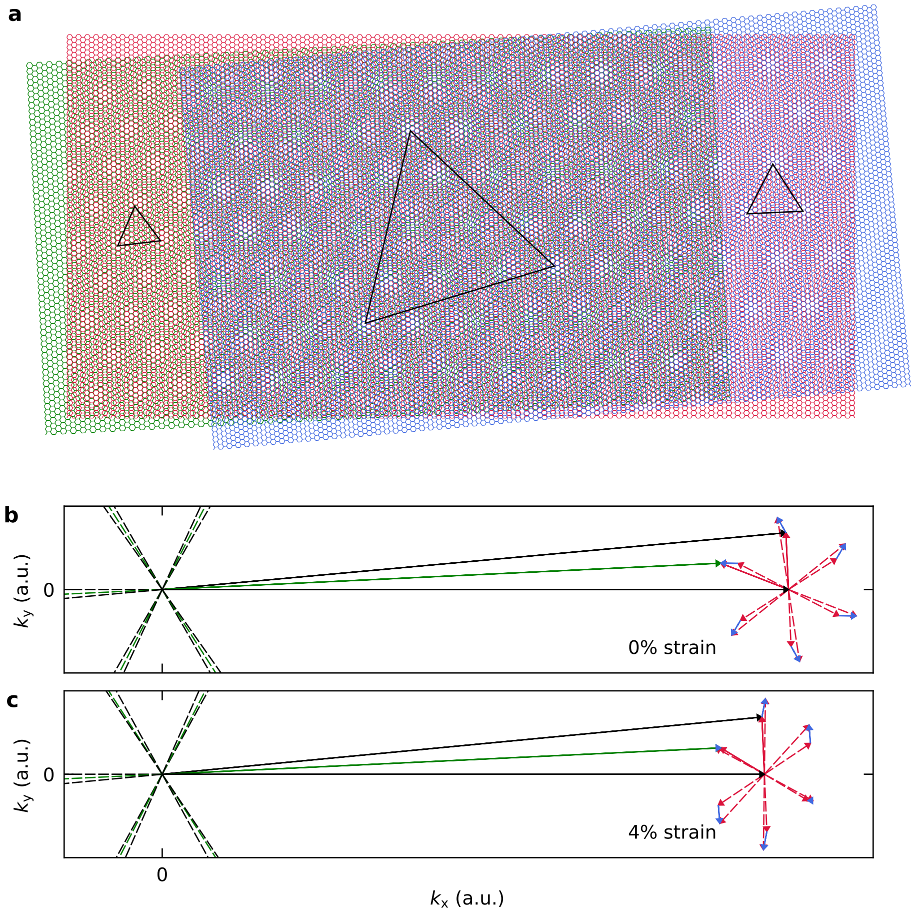

Figure 7.5: Formation of a second-order superlattice. **a** Top view of two twisted graphene layers (red and blue) superposed on an hBN sheet (green). A graphene sheet in close alignment to hBN forms a triangular moiré lattice, likewise do the two twisted graphene sheets (both superlattices emphasized by small triangles). In turn, by superposing these two superlattices a second-order superlattice forms with an even larger periodicity (large triangle). This occurs only for a specific combination of lattice mismatch and twist angles. **b** Second-order superlattice shown in panel **a** represented in reciprocal space. Two black vectors reflect the graphene lattices twisted at $\theta_{\text{TBG}} = 5.2°$, while the green vector corresponds to the hBN lattice with a lattice mismatch of 12% (reducing its reciprocal length) and $\theta_{\text{hBN}} = 2.7°$. The corresponding dashed vectors account for lattice periodicities in other directions (at multiples of 60°). The differences between the mentioned vectors form the first-order superlattices, indicated by two solid red vectors and its equivalents at multiples of 60° (dashed red vectors). The blue vectors constitute the second-order superlattice, defined by the differences of the first-order superlattice vectors. **c** Same data as panel **b** with 4% strain applied to both graphene layers along the zigzag direction. This small amount of strain has a large impact on the magnitudes of the second-order lattice vectors: while two of them only change their direction, the third one becomes marginally small, leading to an amplified lattice constant in that direction.

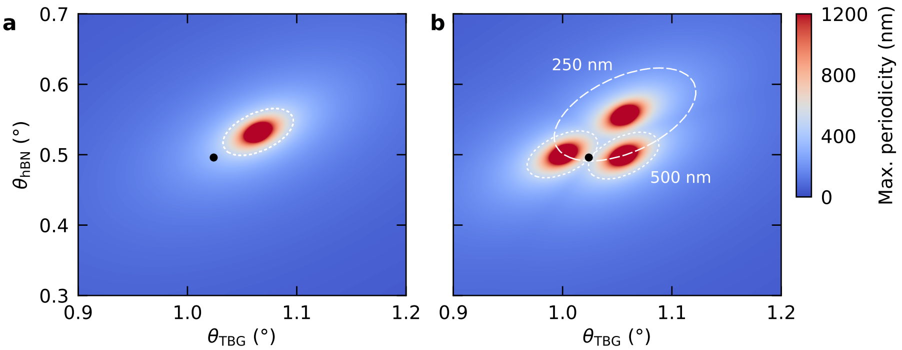

Figure 7.6: Calculated periodicity of second-order superlattice. **a** Lattice periodicity as function of the two twist angles that describe our system. Only for a narrow window of twist angles, a second-order superlattice emerges with macroscopic sizes. For the twist angles in our device, marked by the black dot, the calculated lattice periodicity is slightly below the measured periodicity. **b** Under the application of 0.1% strain along the zigzag direction in both graphene layers, the second-order superlattice becomes anisotropic, as illustrated in Fig. 7.5**c**. We plot the maximum periodicity along any of the second-order superlattice vectors and find three regions wherein a second-order superlattice forms along one of three lattice directions. For the twist angles found in our device (black dot), we can expect second-order superlattices in two directions with a periodicity of $\approx$ 500 nm, and in the third direction $\approx$ 250 nm. In both panels we set the lattice mismatch of hBN to 1.64% with respect to graphene.

in which α is the angle of the principal direction of applied strain with respect to the zigzag direction, and $\rho = 0.165$ is the Poisson ratio of graphene[217]. $\overline{I}$ is the identity matrix. As illustrated in Fig. 7.5c, strain has a large impact on the relatively magnitude and direction of the second-order superlattice vectors. This leads to a deformation of the lattice, such that superlattices act as 'magnifying glasses' of strain[218,219]. With this insight, we repeat the calculation of $\tilde{\lambda}_{\mathrm{M}}$ with 0.1% strain applied to both graphene layers along the zigzag direction. Figure 7.6b reveals three windows where the periodicity peaks along one of the lattice vectors. This means that for any combination of θ_{hBN} and θ_{TBG}, the superlattice periodicities are different in each of the three principal direction (except for the central point between the three windows). For the case of our sample (twist angles indicated by black dot), we can expect $\tilde{\lambda}_{\mathrm{M}} \approx$ 500 nm in two directions, while $\tilde{\lambda}_{\mathrm{M}} \approx$ 250 nm in the third direction. The latter can easily be obscured due to the finite cooling length in our sample, which would explain the presence of photovoltage modulations across two directions. Likewise, the incorporation of strain could explain the observation of a $\approx$ 1 µm periodicity in the bottom-right of the sample, without the presence of fringes in another direction. According to our model, such large periodicity is only possible when the periodicity in the other two directions is strongly reduced.

We note that the result of Fig. 7.6 is sensitive to the imbalance of strain between the graphene layers and to the direction of applied strain. Changing α rotates the three windows wherein second-order superlattices form around their centre by an equivalent rotation. Furthermore, increasing the hBN-graphene lattice mismatch moves these windows towards higher θ_{TBG} and θ_{hBN}. Therefore, we cannot make an exact comparison of the lattice orientation to our data. Nevertheless, and most importantly, our simple model shows qualitative agreement with our observations for a realistic amount of strain and hBN-graphene lattice mismatch. The sensitivity of our model to local variations, combined with our observation of a relatively homogeneous structure in large parts of our sample, suggests that the strain distribution within our sample is rather homogeneous with minimal twist angle variations. A more refined model potentially allows translating the variations in the second-order superlattice structure to a map of the local strain and twist angle of TBG.

7.5. Nano-imaging signatures of nematicity in MATBG

Motivated by the findings above, we acquire additional photovoltage maps at finite carrier densities. Figure 7.6a shows two photovoltage images recorded simultaneously in the upper half of our device, between two different pairs of contact. As the PTE is only sensitive to gradients perpendicular to the projection of the current flow, we need these two distinct contact pairs to obtain a complete picture of the photovoltage contributions. This is evident from the configuration in the right panel, where the current flow lines up with one set of fringes, causing them to disappear. The structure that is revealed for hole-doping is rather similar to the undoped case (Fig. 7.3), except for an increase in the photoresponse.

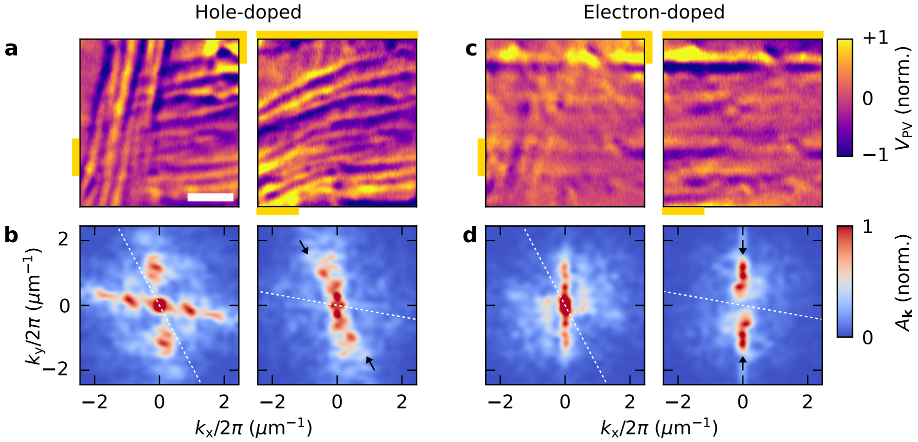

Figure 7.7: Nano-imaging signs of charge-induced nematicity. a Near-field photovoltage images of our sample in a hole-doped state ($n \approx -1.3 \cdot 10^{12}$ cm^{-2}). This is measured in the upper half of the device for two different pairs of contacts, whose relative positions are indicated in gold. By looking at both panels, we identify two sets of fringes running along two directions, similar to those indicated by the dashed lines in Fig. 7.3. The excitation energy is 116 meV and the scale bar is 2 µm. **b** Two-dimensional Fourier transform of the spatial data in panel **a**. These data reveal two orientations of the fringes, separated by $50-80°$. The dashed lines mark the directions along which the photovoltage measurement is insensitive, exemplified by the absence of response in the right panel along the dashed line. **c**,**d** Same data as panels **a**,**b** but with the sample in an electron-doped state ($n \approx 0.8 \cdot 10^{12}$ cm^{-2}). We observe a change in the directions along which the fringes are seen (black arrows in bottom right panels). In particular, the horizontal fringes are only prominently seen for electron-doping, which could be a sign of nematicity.

By converting these real-space maps to their Fourier transform $A_{\mathbf{k}}$, we obtain a better grasp of the geometric properties of the second-order lattice (Fig. 7.6b). A combined look at both Fourier transforms reveals modulations at two angles with a separation of $50-80^{\circ}$, reflecting the two sets of fringes seen in the real-space images. Since the superlattice is not perfectly periodic, peaks occur at different magnitudes of $\mathbf{k}$. However, here we mainly focus on the angles in Fourier space featuring peaks in $A_{\mathbf{k}}$. Intriguingly, this picture is modified drastically when changing from hole- to electron-doping, depicted in Fig. 7.6c,d. One set of spatial modulations seems to have rotated towards the horizontal axes, while leaving the other set intact. Repeated measurements at different carrier densities confirm this behaviour, suggesting it might be induced by the change in carrier type. Above the full-filling carrier density, the data are not conclusive due to the increased cooling length that obscures details in the photovoltage response.

Thus far, we considered the observed structure to be a manifestation of a second-order superlattice. However, since we find a modification with carrier type, this means that either i) the superlattice changes with carrier type or ii) the arrangement of electrons on the underlying superlattice structure changes. The first case can occur when partial lattice relaxation takes place, which involves an energy competition between different types of local lattice arrangements that defines the resulting structure. For instance, in trilayer graphene, the size of ABA versus ABC domains changes as function of carrier density and displacement field[63]. Since this effect is more pronounced when large-scale structural variations occur, such as in minimally twisted graphene structures, it could also play a role in the second-order superlattice considered here. Alternatively, a change in the electronic arrangement on the atomic second-order lattice could manifest itself directly via the electronic detection scheme we use. We speculate that the observed nematic order in transport experiments[55], possibly in combination with strong Coulomb interactions in MABTG, plays a role in facilitating a change in electronic arrangement with carrier type.

7.6. Conclusion

In this Chapter, we presented near-field photovoltage maps of MATBG aligned to hBN, where we observed a semi-periodic modulation covering the entire device. We built a minimalistic model that describes a second-order superlattice formed by the hBN-graphene and TBG moiré lattices. To the best of our knowledge, this provides the first visualization of broken inversion symmetry in MATBG, which has been linked before to emerging ferromagnetic states. Furthermore, our method potentially allows mapping the local twist angle variations and strain profile within the sample[218,219]. These results prove cryogenic near-field photovoltage mapping to be a useful technique for exploring twisted bilayer graphene in future studies.

As this type of second-order lattice has not received much attention thus far, we hope that our findings provide additional guidance for theoretical models aiming to understand the rich set of phenomena occurring in MATBG. In particular, an open question remains on the competition between different superlattice potentials. The fact that we observe signs of correlated states at integer filling factors suggests that the large-scale modulations only provide a weak influence on the magic-angle physics. Yet, the connection of ferromagnetism in MATBG to broken inversion symmetry demonstrates a non-negligible effect of the additional potentials. Therefore, the question rises to what extent each superlattice potential influences the properties of MATBG. Other techniques, such as cryogenic terahertz near-field microscopy, might shed more light on this.

8. Probing twist angle variations in twisted bilayer graphene with photovoltage nanoscopy

In this Chapter, we employ near-field photovoltage nanoscopy to measure twist angle variation in twisted bilayer graphene. We first perform s-SNOM and transport measurements, which serve as a guide to understand the photovoltage maps. We construct a simplified model based on the photothermoelectric effect, which we use the built a map of the local twist angle in our device.

Twist-angle inhomogeneity strongly influences the properties of twisted bilayer graphene (TBG). As the flat-band physics originates from a periodic potential, any spatial disturbance in its periodicity will affect the phase diagram. Therefore, the less disordered a sample it, the richer its physics tend to be. Currently, such disorder seems to be one of the limiting factors for making large progress in the understanding of unresolved phenomena in TBG[80]. Likewise, heterostrain is widely present in TBG and has a direct impact on the energy bandwidth of the flat bands[213]. This reduces the strength of electron-electron correlations, to which multiple phenomena in TBG are tightly linked[22,25,26,28–31,51,53,205]. Thus, techniques that probe the twist angle disorder and map the strain fields are of importance for improving the device fabrication processes.

Probing twist-angle disorder is possible via different techniques. Transport measurements provide a only rough indication of the inhomogeneity, since they measure a global property. Instead, local probes such as STM, TEM and scanning magnetometry can reveal twist angle variations on a much more relevant scale[40,48,62]. Yet, these techniques either involve a more complicated sample fabrication procedure with half-encapculated TBG, are limited in the spatial range, or require highly specialized experimental setups. An alternative approach uses photovoltage nanoscopy, which thus far has only been used in TBG to measure the twist angle at an interface between TBG and single-layer graphene[96].

Here, we employ cryogenic photovoltage nanoscopy to map the local twist angle with a spatial resolution limited by the cooling length of $\sim$ 600 nm. First we show qualitatively that cryogenic s-SNOM can reveal twist angle variations based on the absorption fingerprint of TBG. The information we obtain from this, together with transport measurements, serves as a guide for interpreting our near-field photovoltage measurements. We construct a model based on the photothermoelectric effect and show that this technique, in principle, allows determining the local twist angle with a resolution $\sim 0.01°$, which is on par with scanning magnetometry.

8.1. Probing twist angle variations with s-SNOM

Figure 8.1a shows an optical picture of a TBG device fabricated by Petr Stepanov, with a 10 nm thick bottom hBN. Instead of the tear-and-stack technique mentioned in Sec. 2.1, the graphene flake is cut using an AFM tip. This should reduce unintentional strain induced by tearing the flakes[51,54,209]. However, we will see later that this device exhibits rather large twist angle inhomogeneity. To characterize our device, we first measure the near-field phase contrast using cryogenic s-SNOM, introduced in Chapter 6, at an excitation energy $\hbar\omega = 121$ meV, as depicted in Fig. 8.1b. This measurements, as well as the photovoltage measurements below, are carried out at a temperature $T = 10$ K. We observe smooth changes in the phase contrast, as well as abrupt steps. We can link them to variations in the properties of TBG by recalling that the near-field scattering phase serves as a local probe of the absorption[118].

Absorption in TBG can occur via intraband and interband excitations. However, due to the relative flatness of the bands in TBG, only interband absorption plays a major role at $\hbar\omega = 121$ meV. As discussed in more detail in Sec. A.4, interband absorption is affected by the twist angle and the carrier density. Roughly speaking, interband transitions are strongly reduced when $\hbar\omega$ is smaller than the energy gap between the flat and remote bands within $M - K$ in the superlatttice Brilouin zone. Because the largest joint density

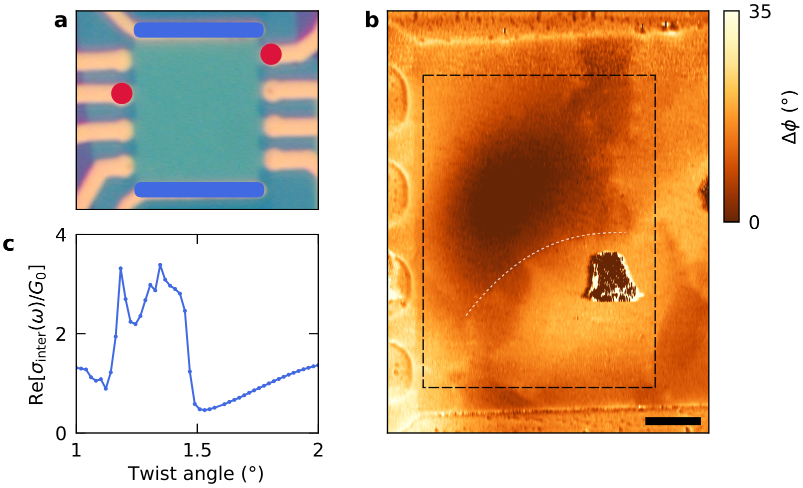

Figure 8.1: Twist angle variations revealed with s-SNOM. **a** Optical image of our device, patterned in a Hall-bar shape. The electrical contacts are gold-coloured, of which the pairs with red and blue marks are used to measure the two-probe resistances shown in Fig. 8.2**a**. **b** Near-field scattering phase image of our device revealing both smooth and sharp variations in the absorption. The illumination energy is 121 meV and the carrier density is $5.3 \cdot 10^{12}$ cm^{-2}, which is approximately equal to $n_{\mathrm{ff}}(\theta = 1.5°)$. The white dotted line marks a sharp interface. The scale bar is 2 μm, and the noisy area near the centre is a measurement artefact. **c** Calculated interband absorption of undoped TBG from Ref. [91] in units of the conductance quantum $G_0 = 2e^2/h$ for a range of twist angles at $\hbar\omega = 121$ meV. As the remote bands shift up in energy with twist angle, absorption is quenched for $\theta \gtrsim 1.5°$.

of states between the flat and remote bands occurs in the $M - K$ part for infrared energies (Fig. 1.2), we only consider them in this qualitative analysis. As the remote bands shift up in energy with increasing twist angle, interband transitions become quenched above a certain twist angle for a given excitation energy. This is reflected in the calculated interband absorption $\mathrm{Re}[\sigma_{\mathrm{inter}}(\omega)]$ for undoped TBG with $\hbar\omega = 121$ meV (Fig. 8.1c). We see a sharp drop of $\mathrm{Re}[\sigma_{\mathrm{inter}}(\omega)]$ near $\theta = 1.5°$, in line with the qualitative description above. Even though the near-field scattering map was taken at a finite carrier density n, this description is not altered much as n is not sufficiently large to induce Pauli blocking of the interband transitions.

With this qualitative picture in mind, we can understand the scattering phase contrast in Fig. 8.1b. The bright regions absorb relatively strongly the infrared light, hence the twist angle is below 1.5°, while the darker regions with reduced absorption correspond to a larger twist angle. A much lower twist angle ($< 1°$) also could lead to a reduced absorption, however, we exclude this option based on the transport measurements below. We will see with photovoltage nanoscopy that the twist angle increases monotonically from the left side of the device towards the interface in the middle of the device. Yet, the absorption shows a minimum at a position where the twist angle is not highest. We can explain this with the calculated absorption (Fig. 8.1c), displaying an increasing absorption for $\theta > 1.5°$. Enhanced band nesting between the bands towards higher twist angle enables more interband transitions within the $K - \Gamma - M$ zone of the superlatttice Brilouin zone.

8.2. Transport signatures of twist angle disorder

We proceed by measuring the two-probe resistance R_{2p} in our device as function of carrier density. Figure 8.2a plots R_{2p} as probed between two different pairs of contacts indicated in Fig. 8.1a. Besides the usual peak at charge neutrality, R_{2p} exhibit multiple peaks at larger carrier densities, which are partially overlapping between the two traces. We attribute them to the insulating states at completely filled/emptied flat bands in TBG, leading to a peak in the resistance at $n = n_s$[15]. This full-filling carrier density n_s is given for any triangular moiré superlattice without lattice mismatch by

$$\begin{aligned} n_s &= \frac{8}{\sqrt{3}\lambda_M^2}, \\ \lambda_M &= \frac{a}{2\sin(\theta/2)} \approx a\theta[\text{rad}], \end{aligned} \tag{8.1}$$

where λ_M is the periodicity of the moiré lattice and $a \approx 0.246$ nm is the lattice constant of single-layer graphene. The fact that we see multiple peaks in the resistance points at the presence of different twist angles in our device. This twist angle disorder also manifests itself by broadening the full-filling resistance peaks. The carrier densities at which the resistance peaks are related to the twist angle via Eq. (8.1) and are shown in Figure 8.2b. This demonstrates that the twist angle varies within our device within $\approx 1.2 - 1.8°$, in agreement with the measured near-field phase contrast (Fig. 8.1).

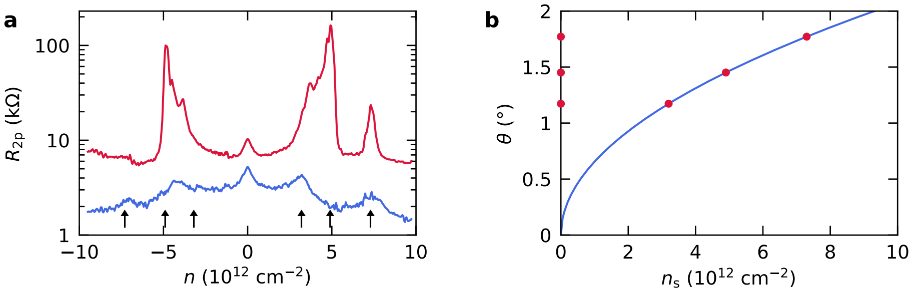

Figure 8.2: Probing twist angle inhomogeneity with transport measurements. a Two-probe resistance between two different pairs of contacts in our device, marked by the coloured contacts in Fig. 8.1**a**. We identify several prominent peaks in the resistance, marked by the arrows. **b** Relation between the twist angle and full-filling carrier density according to Eq. (8.1). The red dots indicate the twist angles corresponding to three resistance peaks in panel **a**.

8.3. Twist angle variations revealed by photovoltage nanoscopy

To attempt probing the twist angle inhomogeneity with a higher precision and on the nanoscale, we resort to photovoltage nanoscopy measurements. This technique is introduced in Sec. 2.5 and we use the cryogenic s-SNOM system discussed in Chapter 6 to perform these measurements. The use of low temperatures is required to avoid thermal

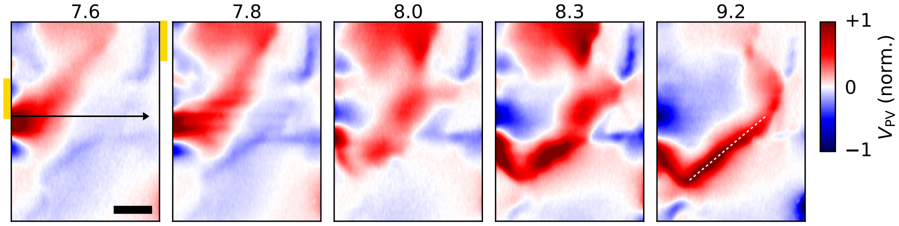

Figure 8.3: Near-field photovoltage response near full-filling carrier density. Measured photovoltage at various carrier densities (in units of 10^{12} cm^{-2}) within the area marked by the dashed rectangle in Fig. 8.1**b**. We use the contacts marked in red in Fig. 8.1**a**, and show their relative locations in gold. The bottom lead grounds the device. The dotted line in the right panel marks an interface with a sharp step in twist angle. The excitation energy is 108 meV and the scale bar is 2 µm. As the photovoltage signal is rather weak in this device, we lock to the first harmonic of the cantilever motion, which could lead to unwanted far-field backgrounds. We verified that this is negligible in these measurements.

smearing of the band occupation and derived quantities such as the Seebeck coefficient. As this property is exactly what provides us a sensitive probe of the local twist angle, we need to minimize mixing the band occupation. Figure 8.3 shows a series of photovoltage maps within the central area of our device. These are taken at carrier densities near $n = 8 \cdot 10^{12}$ cm^{-2}, which is close the highest resistance peak seen in Fig. 8.2b. We can identify the following features: i) near the left contact there is a strong positive photovoltage response for lower carrier density (left panel), ii) for slightly higher carrier density the photovoltage response become stronger towards the centre of the device (middle panel), iii) at an even higher carrier density, the response near the left contact has changed sign, while an interface in the middle of the device lights up with a strong positive photovoltage.

Given these strong spatial variations in the measured photovoltage for increasing carrier density, we measure the photovoltage along the arrow in Fig. 8.3 and systematically sweep the carrier density. This is depicted in Fig. 8.4a and shows several interesting features. To guide us through them, we analyze the response at three different positions indicated by the arrows, with the corresponding line traces shown in Fig. 8.4b. The strongest photovoltage response occurs near the contact (red arrow and trace), with a sign change at $n = 8 \cdot 10^{12}$ cm^{-2}. In addition, there is a prominent sign change at charge neutrality. As we move into the bulk (yellow arrow and trace), the sign reversal near $n = 8 \cdot 10^{12}$ cm^{-2} disappears, and the photovoltage only shows a peak at slightly higher carrier density. Even further inside the sample (blue arrow and trace), we can identify two peaks in the response at $5 \cdot 10^{12}$ cm^{-2} and $9 \cdot 10^{12}$ cm^{-2}, with a negative response between them. We find the same qualitative behaviour for negative carrier densities, except that the response is slightly weaker. A finite cooling length accounts for the spatial broadening of the features.

8.4. Mapping the local twist angle with the photothermoelectric effect

To understand our results, we try to interpret them using the photothermoelectric effect (PTE). This is in graphene-based devices the dominant pathway to generate a photovoltage[123]. As outlined in Sec. 2.5 and Chapter 4, the photovoltage response is driven by spatial gradients in the Seebeck coefficient S. We recall that for metals S is related to the conductivity σ and temperature T via the Mott formula

$$S \propto \frac{T}{\sigma}\frac{\mathrm{d}\sigma}{\mathrm{d}\mu}, \tag{8.2}$$

where μ is the chemical potential. To calculate S of TBG qualitatively, we follow a similar approach used in Ref. 96 and define the resistivity $\rho = 1/\sigma$ as function of carrier density as

$$\rho(n, n_\mathrm{s}) = \frac{\rho_\mathrm{ff}}{1+\left(\frac{n+n_\mathrm{s}}{n_\mathrm{s}^*}\right)^2} + \frac{\rho_\mathrm{cnp}}{1+\left(\frac{n}{n_\mathrm{cnp}^*}\right)^2} + \frac{\rho_\mathrm{ff}}{1+\left(\frac{n-n_\mathrm{s}}{n_\mathrm{s}^*}\right)^2}. \tag{8.3}$$

This simple formula describes qualitatively the main features seen in the resistivity of TBG. One peak at charge neutrality with a magnitude ρ_cnp and broadening due to disorder density n_cnp^*, and likewise two peaks at positive and negative full-filling carrier density n_s. In the latter case, n_cnp^* reflects mainly the broadening of the resistance peak due to thermal activation of the full-filling gap Δ according to $\rho \propto e^{-\Delta/2k_\mathrm{B}T}$. The black dotted line in Fig. 8.4c depicts the profile of $\rho(n)$ for $n_\mathrm{s} = 8 \cdot 10^{12}$ cm^{-2}, which we use in the following analysis. We simplify the model further by assuming that $\mathrm{d}\sigma/\mathrm{d}\mu$ is a constant, despite the sharp changes in $\mu(n)$ near $n = n_\mathrm{s}$. As long as n_s^* is sufficiently small, this simplification does not impact the analysis. Using the Mott formula and $\rho(n, n_\mathrm{s})$ defined above, we calculate S, shown by the red trace in Fig. 8.4c. It shows a typical profile with sign changes coinciding with maxima in the resistivity, along with peaks in the magnitude on either side.

Since photothermoelectric currents are generated by spatial changes in the Seebeck coefficient, we consider three different types of interfaces, as shown in Fig. 8.4c. Because the Seebeck coefficient of gold is relatively small compared to S of TBG[220], the red trace also describes the difference in S between TBG and a gold lead. The yellow trace shows the difference in $S(n, n_\mathrm{s})$ for slightly different values of n_s, which occurs when there is a small spatial gradient of the twist angle. The blue traces illustrates the difference in S for a large change in n_s, occurring for a large step in twist angle.

The similarity between the calculated differences in S and the measured photovoltage response as function of carrier density is striking (Fig. 8.4b,c). This strengthens the assumption that the photoresponse is governed by the PTE. Altogether, under the assumption that the measured photovoltage is solely generated by twist angle disorder, we interpret the data in Fig. 8.4a as follows. Near $x_\mathrm{tip} = 0$ µm the photovoltage is generated by the junction between the gold lead and TBG with $n_\mathrm{s} \approx 8.0 \cdot 10^{12}$ cm^{-2} corresponding to $\theta \approx 1.85°$. Moving further into the bulk, the twist angle increases slightly, leading to a peak in photovoltage at $n = n_\mathrm{s}$ and which moves up slowly with position. Finally, at the blue arrow our device exhibits a step in the twist angle from $\theta \approx 1.88°$ to $\theta \approx 1.67°$, corresponding to $n_\mathrm{s} \approx 8.2 \cdot 10^{12}$ cm^{-2} and $n_\mathrm{s} \approx 6.5 \cdot 10^{12}$ cm^{-2}.

We can take this analysis a step further and make a rough estimation of the twist angle disorder within our device. Guided by the near-field scattering image (Fig. 8.1b), we assume that majority of the area of our device only hosts small gradients in the twist angle. In this case we can deduce the local twist angle from the the carrier density at which the measured photovoltage shows a maximum (yellow traces in Fig. 8.4). To this end, we collect a large series of photovoltage maps like those in Fig. 8.3 for carrier densities

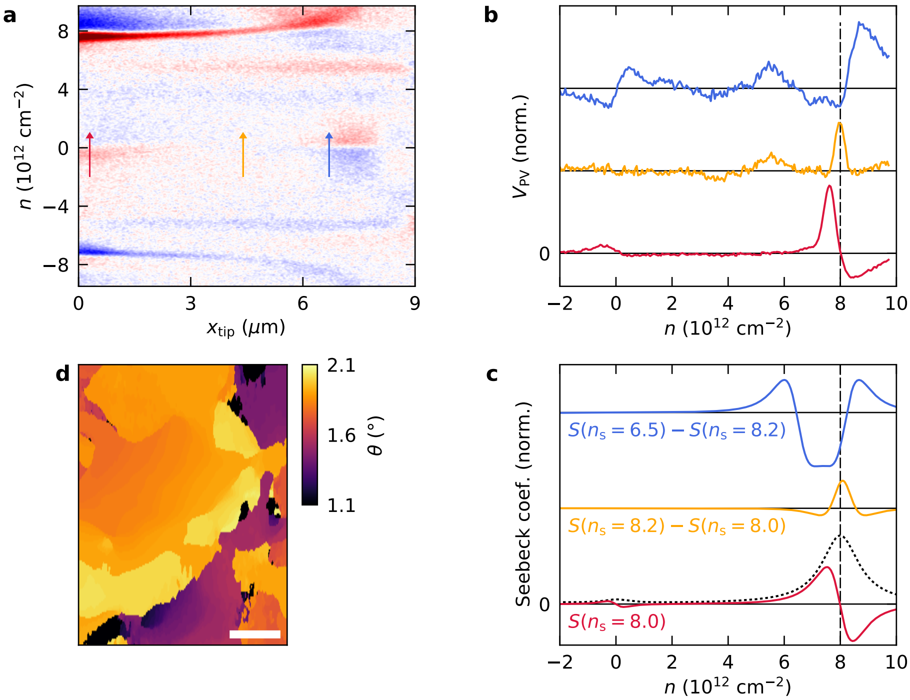

Figure 8.4: Determining the local twist angle from the photovoltage response. **a** Line cut of the near-field photovoltage response along the arrow in Fig. 8.3 for a range of carrier densities, showing a strong response near $n \approx 8 \cdot 10^{12}$ cm^{-2}. **b** Traces of photovoltage response in panel **a** at three different positions marked by the colour-matching arrows. The traces are offset for clarity with the black lines indicating the zero values. The dashed line indicates the sign-change at $n \approx 8 \cdot 10^{12}$ cm^{-2} in the red trace. **c** Calculated Seebeck coefficient according to the Mott equation from the electrical resistivity given by Eq. (8.3) (dotted line) for a given full-filling carrier density n_s (in units of 10^{12} cm^{-2}). The upper two traces show the difference in Seebeck coefficient for different n_s. **d** Map of the twist angle deduced from a series of photovoltage maps at different carrier densities. The area covers the same as in Fig. 8.3 and the rectangle in Fig. 8.1**b**. In the central-left area the twist angle map shows a smooth gradient, while towards the bottom-right a sharp change in twist angle can be seen. The limited number of photovoltage maps used in the analysis causes the appearance of terraces. Scale bar is 2 µm.

between $0.6 \cdot 10^{12}$ cm^{-2} and $9.7 \cdot 10^{12}$ cm^{-2}. By determining the carrier density that gives the maximum photovoltage response at each position, we obtain a map of the twist angle as shown in Fig. 8.4d. It displays a slowly increasing twist angle from the left side towards the middle of the device, upon reaching a sharp junction at which the twist angle drops. We note that the finite cooling length leads to an overestimation of the region with larger twist angle. Advanced algorithms could account for this, but this is beyond the scope of this work.

The accuracy in determining the local twist angle via this method under the aforementioned assumptions is limited by the signal-to-noise ratio of the photovoltage. For small twist angle gradients, the magnitude of the corresponding peak (yellow traces in Fig. 8.4) scales linear with the twist angle gradient as we verified numerically. As long as the gradient is sufficiently large, there is a detectable peak in the photovoltage. The resulting accuracy in determining the local twist angle is then only limited to the step size in carrier density between the spatial maps. In the case presented here, we were able to probe a gradient of approximately 0.003 °/µm (1.82° − 1.80° over 6 µm) with a signal-to-noise ratio of about 10, suggesting that for even smaller gradients the twist angle can be measured locally. To obtain a twist angle resolution of 0.01°, a step size of $8.4 \cdot 10^{10}$ cm^{-2} is required for twist angles near 1.8°.

On the other hand, the spatial resolution is limited by the cooling length of the carriers. By using the interface highlighted in Fig. 8.3, we estimate the cooling length to be $\approx$ 600 nm. Since the flat bands become flatter towards smaller twist angles, the mobility of the carriers also reduces, leading to a lower cooling length. Consequently, the spatial accuracy is enhanced for twist angles near the magic angle.

The overall accuracy of this method can be improved by measuring simultaneously the generated photovoltage between two contacts pairs in perpendicular orientation, analogous to the method used in Chap. 4. In the measurements presented here, where we use only one pair of contacts, there are certain directions where the twist angle gradients line up perpendicular to the current flow; thus, they do not generate any photovoltage. By measuring along two different projections, any twist angle gradient will always generate a photovoltage for at least one projection. However, a proper analysis of the photoresponse from multiple pairs requires calculating the current flows between the different pairs, which can be a difficult task owing to the large resistivity changes near full-filling carrier density.

8.5. Conclusion

To summarize, we presented in this Chapter combined s-SNOM, transport and photovoltage nanoscopy measurements, which allowed us to understand the details of the observed photovoltage response. Based on this, we created a method that allows mapping the twist inhomogeneity in TBG via the photothermoelectric effect in combination with the high sensitivity of the Seebeck coefficient on the local twist angle. It offers an alternative to scanning magnetometry, with both techniques being able to probe the local twist angle to an accuracy better than 0.01°. While our method might feature a slightly lower spatial resolution in the order of 500 nm, its reduced complexity compensates for this. We believe this method will be of use in developing sample fabrication techniques aimed at reducing the twist angle inhomogeneity. Since there might be additional contributions to the photovoltage response at the magic angle, such fabrication techniques should be developed at slightly larger twist angles but can afterwards still be applied at the magic angle.

9. Summary and outlook

We set off this Thesis with the aims i) to understand the optical and optoelectronic properties of twisted bilayer graphene systems and their connection to the fundamental structure of these systems and ii) to establish new techniques to study the exotic states of twisted graphene systems at low temperatures. s-SNOM and photocurrent nanoscopy were chosen as main experimental tools for nanoscale imaging, as outlined in Chapter 2. With them we explored the optical and opto-electronic response of twisted bilayer graphene, ranging from minimally twisted bilayer graphene ($\theta < 0.1°$) to samples near the magic angle ($\theta \approx 1°$). Here, we summarize the main results of this Thesis.

We first described in Chapter 3 the collective excitations that we discovered in TBG near the magic angle. By means of s-SNOM, we found in charge-neutral TBG regions that exhibit periodic oscillations, which we interpreted as interband plasmons. In contrast to intraband plasmons in single-layer graphene, these excitations follow a dispersion relation that starts with a finite energy at zero momentum. By associating the dispersion relation to the optical conductivity, we could link these excitations to the optical transitions between the flat and remote bands. The enhanced strength of the associated peak in the optical conductivity provides a hint that band nesting in TBG is stronger than assumed thus far. This points at a reduced interlayer coupling in the AA-stacked regions, which could originate from enhanced screening due to electron-electron interactions.

After this, we investigated in Chapter 4 the optoelectronic response of minimally twisted bilayer graphene using photocurrent nanoscopy. This uncovered a complex photocurrent pattern that is sensitive to the orientation of the contact electrodes. We linked these periodic patterns to the underlying domain wall network where the electronic properties change sharply. Supported by simulations, we showed that the observed photocurrent is generated by the photothermoelectric effect in combination with the sharp dips in the Seebeck coefficient at the domain walls. Our results also revealed how hyperbolic phonon polaritons are able to pass underneath domain walls, causing an apparent local reduction in the generated photocurrent.

A major challenge in s-SNOM experiments is independent control of the carrier density and transverse displacement field. In Chapter 5 we show that this can be overcome by employing WSe_2 as an infrared-transparent top gate. Using this semiconducting gate electrode, we can tune the plasmon wavelength of bilayer graphene without obstructing the near-field access. The measured plasmon wavelength serves as a local probe of the carrier density, which allowed us to extract the gating efficiency of the trilayer WSe_2 top gate. We found that the gate voltage needs to overcome a certain threshold related to the band gap in order to induce carriers in bilayer graphene. This is captured in a model that uses a combination of geometric capacitances and the the quantum capacitance of WSe_2.

Another central challenge in the field of near-field optical experiments is to perform them in cryogenic conditions. In Chapter 6 we discussed the development of a cryogenic s-SNOM based on a commercial system. To allow reliable operation, several improvements were made concerning the AFM operation and vibration isolation of the system. In particular, we devised an active damping system to reduce the floor vibrations coupled to the system. At a current base temperature of 10 K, we found rms noise values of the scattering amplitude and phase of $\approx 2\%$ and $\approx 1^\circ$ respectively, in par with room-temperature s-SNOM systems.

We made use of the latter system and performed cryogenic photovoltage nanoscopy on MATBG. In Chapter 7 our measurements revealed a large-scale semi-periodic structure across the entire sample, which we interpreted as a manifestation of a second-order superlattice. This is formed by MATBG and graphene closely aligned to hBN, which we described with a model incorporating a realistic amount of strain in the graphene layers. These results constitute a direct visualization of broken inversion symmetry, which is a key requirement for ferromagnetic states in MATBG.

In Chapter 8 we applied cryogenic photovoltage nanoscopy to study a TBG sample with larger twist angle variations. We found a photoresponse that strongly varies with position and carrier density. Combined with s-SNOM and transport measurements, we were able to unravel the photoresponse using the photothermoelectric effect. Our model defines a method to map the twist angle with TBG samples with a resolution on par with scanning magnetometry.

From a broader perspective, the results on TBG near the magic angle show that optical nano-imaging allows spatial probing of interaction effects at the nanoscale, which can potentially elucidate the contribution of collective excitations to many-body ground states[143]. We also emphasize that propagating plasmons with strong wavelength suppression, and without the need for additional doping, are of use for strong light-matter interactions[221], quantum plasmonics[222] or the creation of metamaterials and nano-photonic devices. Furthermore, we hope that our observation of a second-order superlattice provides guidance in developing theoretical models aiming to study different pathways that assist strong electron-electron interactions in breaking inversion symmetry.

Likewise, our work on mTBG demonstrates that sub-diffraction photocurrent spectroscopy is an exceptional tool for uncovering the optoelectronic properties of moiré superlattices. Local probing at length scales of the superlattice provides deeper insight into the microscopic mechanisms that govern the photoresponse and the exact role of the moiré lattice. With the photoresponse of semiconductor heterostructures being at the heart of modern optoelectronics[223,224], knowledge on the nanoscale is essential for future optoelectronic devices based on twisted bilayer graphene. This technique also proves to be useful from the perspective of structural characterization, as it allows mapping the twist angle distribution in TBG, as well as the influence of strain fields.

The two technological advancements we presented here further unlocks the scientific potential of near-field microscopy. The value of cryogenic s-SNOM systems was proven in recent experiments with temperatures down to 25 K[112,185,195,225,226], wherein the reduced temperature enabled access to interesting phases of matter and their transitions, and enhanced lifetimes of collective excitations. Much excitement is anticipated when the temperature can be reduced further to the vicinity of the correlated states of TBG (1-10 K). This, in combination with terahertz excitation frequencies[227] and independent control over carrier density and displacement field, paves the way for future experiments on exotic states in 2D materials thus far untouched by nano-optics[18,22,28,29,31,55,81–83,90,92,157,158].

A. Appendices to Chapter 3

A.1. Low-temperature transport characterization to determine the twist angle

Daniel Rodan and Yuan Cao from the MIT group characterized the transport properties of the near-magic angle devices described in Chapter 3 in a dilution refrigerator, with a base temperature of ≈ 70 mK, which is equipped with a superconducting magnet generating a magnetic field perpendicular to the TBG electron gas. All the transport data are acquired using standard low-frequency lock-in techniques with discrete and distributed cryogenic low-pass filters removing thermal noise from the biasing and measurement lines[228]. We bias the device with a fixed current of 10 nA and measure the pre-amplified four-probe voltages using SR830 lock-in amplifiers that were synchronized to a frequency in the range $1 - 20$ Hz.

We extract the twist angle and CNP from cryogenic magnetotransport measurements (Fig. A.1)[15,22]. For small twist angles $1° < \theta < 3°$, the band gaps between the nearly-flat bands and the nearest conduction and valence bands cause strongly insulating states

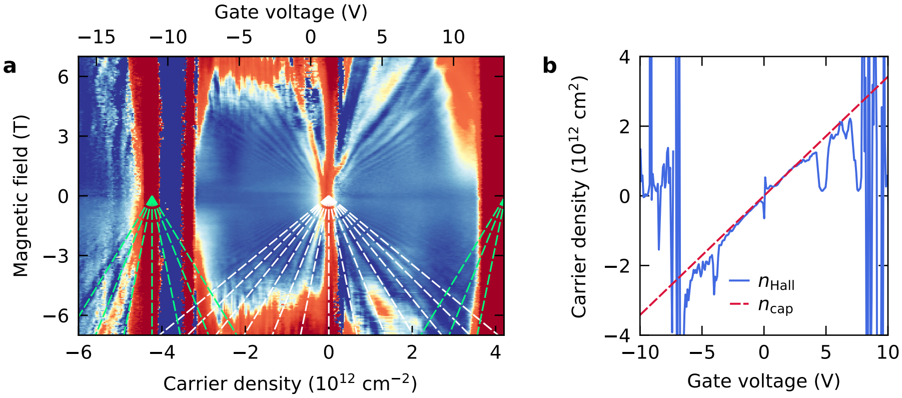

Figure A.1: Determination of the twist angle using cryogenic transport measurements. **a** Longitudinal resistance showing the Landau levels originating from the CNP (white dashed lines) and from the insulating states at full filling (green dashed lines, centred at $n_s = \pm 4.24 \cdot 10^{12}$ cm^{-2}). These transport measurements were performed at ≈ 70 mK. **b** The carrier density $n_{\text{Hall}} = \frac{B}{-eR_{xy}}$ measured from the Hall resistance R_{xy} at a magnetic field $B = 1$ T (blue curve), which agrees well with the carrier density n_{cap} calculated from the slopes of the Landau levels (red curve). The extracted capacity between the sample and the bottom gate, taking into account the measured bottom hBN thickness of 47 nm, corresponds to an out-of-plane static dielectric constant of the hBN $\epsilon_z(\omega = 0) = 2.91$.

in transport measurements at characteristic carrier densities of $\pm n_\mathrm{s}$[15,22,34]. This density corresponds to the inverse of the superlattice unit cell, and by taking the double spin and valley degeneracy into account we determine the average twist angle as

$$\theta[\mathrm{rad}] \approx \sqrt{\frac{\sqrt{3}a^2}{8} n_\mathrm{s}}, \tag{A.1}$$

with $a = 0.246$ nm being the lattice constant of graphene. We determine n_s by extrapolating the Landau levels measured at high magnetic fields around these insulating states, down to zero magnetic field (Fig. A.1a). This yields $\theta = 1.35°$ with an uncertainty of 0.02°. As part of this procedure, we calibrate the carrier density to the applied gate voltage by fitting the slope of the Landau levels around the CNP, which appear at $n = \nu B/\phi_0$, with filling factors $\nu = \pm 4, 8, 12, \ldots$, where $\phi_0 = h/e$ is the magnetic flux quantum. As a crosscheck we also extracted the electronic density from Hall measurement near the CNP. As shown in Fig. A.1b, this second procedure yields a result that agrees well with the density obtained from the slopes of the Landau levels.

A.2. Correlation between optical activity and topography

In some cases, we found a correlation between the optically active regions in near-magic angle samples presented in Chapter 3 and fine features in the sample topography, as measured simultaneously using atomic force microscopy. Fig. A.2 provides examples of this correlation and shows the presence of height steps of about 0.4 nm. These coincide with the boundaries of the optically active regions, which correspond to the higher areas. In addition, the small bubbles of a few nanometres thick, which are common for these van der Waals heterostructures, coincide in some cases with the boundaries of the optically active regions, or are located at the centre of regions where no collective excitations were measured. Besides that, we note that in the core of one device we did not observe the collective modes, while being superconducting at low temperatures and not having been

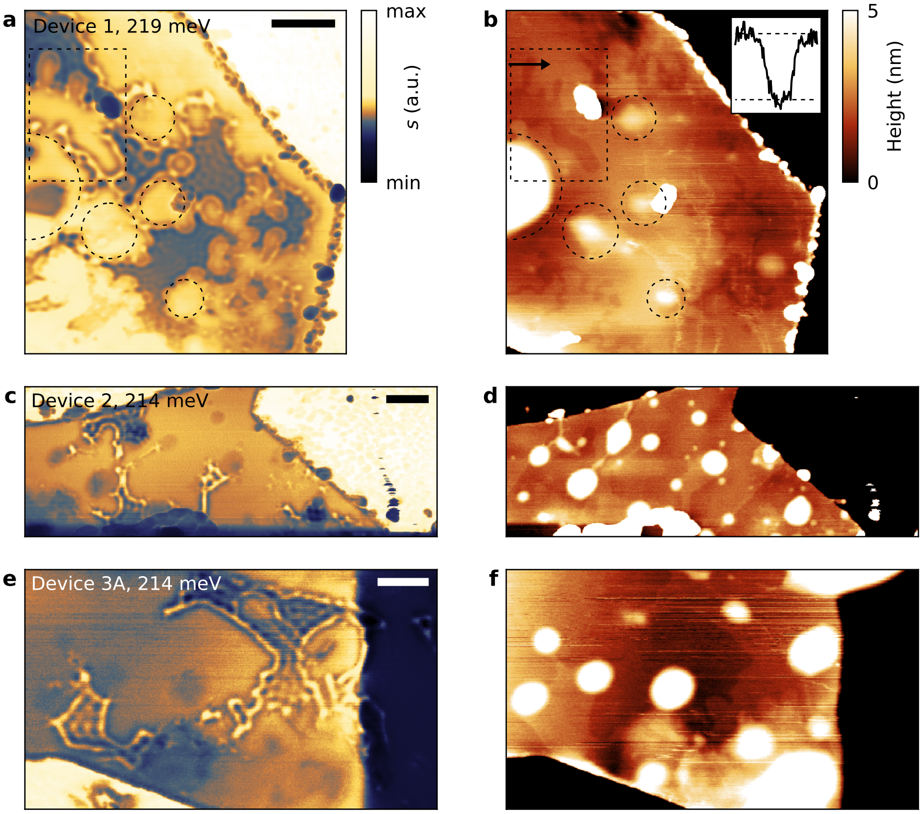

Figure A.2: Correlation between optical activity and topography in near-magic angle TBG. a Near-field image of the device shown in Chapter 3, with the corresponding AFM data shown in panel **b**. The rectangular area (dashed line) encloses several boundaries of optically active regions, which have a height step of several Å (inset shows line cut along the black arrow with the dashed lines 3.5 Å spaced apart). The dashed circles mark small bubbles within the 2D heterostructure surrounded by regions with collective excitations. **c**-**f**. Same as in **a**-**b** but for two other devices. All scale bars are 500 nm.

touched by contact-mode AFM. This illustrates that being close to magic angle itself is not the only requirement for the formation of interband plasmons.

We have observed areas of collective excitations appearing and disappearing in response to the tapping- and contact-mode atomic force microscopy measurements (Fig. A.3). These changes go along with small, but critical changes in the sample topography. Although it is difficult to deduce precisely which local parameters are changing (such as twist angle, interlayer distance and coupling), it demonstrates that this system is rather sensitive to external forces[61].

These observations point to the crucial role strain plays in the formation of these regions. This goes along with variations of the twist angle and interlayer coupling as commonly found in TBG samples[15,31,39,48], and directly affects the properties of the plasmonic modes. As can be seen from Fig. 3.1b, the boundaries of the optically active areas are typically formed by sequences of arcs with radii ≈ 120 − 200 nm. This shape may stem from

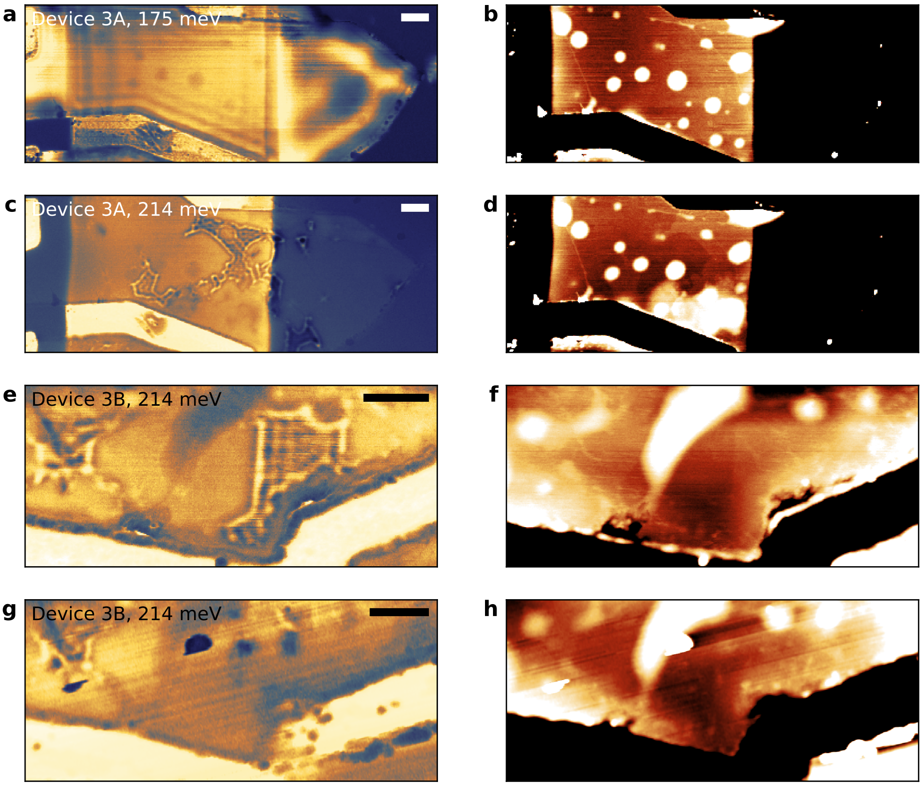

Figure A.3: Changes in optically active areas induced by AFM. **a** Near-field image and corresponding topography (panel **b**) before a structural change occurred during an s-SNOM measurement with the AFM operated in tapping-mode. The fringes parallel to the sample edges are hBN phonon-polaritons. After this change, the topography shows a few alterations and the collective excitations appear (**c**-**d**). **e**-**f**. Collective excitations in twisted double bilayer graphene before a second AFM-brooming session, which disappeared afterwards (**g**-**h**). All scale bars are 500 nm and the colour scales are the same as in Fig. A.2 (except in panels **f** and **h**, where it spans 10 nm).

a boundary between two structural phases, such as twist angles near and far from magic angle as seen in SQUID measurements[48]. This goes along with an energy-per-area for each structural phase, together with an energy-per-length for the interface. Since individual layers in van der Waals heterostructures can rotate with relative ease, it is possible that the AFM-brooming procedure 'locks' regions into particular twist angles. Considering this, together with the mentioned energy densities, the interfaces might attain shapes that appear rather irregular. We discuss the sensitivity of propagating interband plasmons to twist-angle variations in Sec. A.4.

A.3. Details of the extraction of optical conductivity of TBG

In the local approximation for the optical conductivity[138], the longitudinal dielectric function is given by

$$\epsilon(q,\omega) = 1 + \frac{iq^2 V_{q,\omega}}{\omega}\sigma(\omega). \tag{A.2}$$

Here, $\sigma(\omega)$ is the local, frequency-dependent conductivity and $V_{q,\omega}$ is the electron-electron (e-e) interaction potential. Note that $\sigma(\omega)$ is a scalar because the system has a vertical C_3 symmetry axis. The e-e interaction potential relates a charge density fluctuation $\rho(q,\omega)$ in the electron gas to the electric potential $\phi(q,\omega)$ it induces through

$$\phi(q,\omega) = V_{q,\omega}\rho(q,\omega). \tag{A.3}$$

For the type of structure used in our experiments, the e-e interaction potential can be calculated following Ref. 126. This yields

$$V_{q,\omega} = \frac{2\pi}{q\tilde{\epsilon}(\omega)} F(q,\omega), \tag{A.4}$$

where $\tilde{\epsilon}(\omega) = \sqrt{\epsilon_{\mathrm{x,y}}(\omega)\epsilon_{\mathrm{z}}(\omega)}$ is the average permittivity of hBN, $\eta = \sqrt{\epsilon_{\mathrm{x,y}}(\omega)/\epsilon_{\mathrm{z}}(\omega)}$ is its anisotropy factor, and

$$F(q,\omega) = \frac{[(\tilde{\epsilon}(\omega)+1) + (\tilde{\epsilon}(\omega)-1)e^{-2q\eta(\omega)t_2}](1-e^{-2q\eta(\omega)t_1})}{(\tilde{\epsilon}(\omega)+1) + (\tilde{\epsilon}(\omega)-1)e^{-2q\eta(\omega)(t_1+t_2)}}, \tag{A.5}$$

t_1 and t_2 being the bottom and top hBN thickness, respectively. We remind the reader that hBN is an uniaxial crystal with the optical axis $\hat{\mathbf{z}}$ perpendicular to the plane of the flake. An oscillator model describes its dielectric tensor

$$\epsilon_i(\omega) = \epsilon_i(\infty) + \frac{s_i \hbar^2\omega_i^2}{\hbar^2\omega_i^2 - i\hbar^2\gamma_i\omega - \hbar^2\omega^2}, \tag{A.6}$$

with parameters given in Ref. 152 and reported for completeness in Table A.1.

The mode penetrates for a characteristic length $L_z = [q\eta(\omega)]^{-1}$ in the hBN slab, in the vertical direction. To couple efficiently to the AFM tip, the thickness of the top hBN layer t_2 has to be smaller than L_z. Note that close to the upper edge of the higher Reststrahlen band of hBN, at $\hbar\omega \approx 200$ meV, L_z diverges due to the vanishing of ϵ_z.

In determining the imaginary part of the optical conductivity σ_2 from $\sigma(\omega) = \frac{i\omega}{q^2 V_{q,\omega}}$, we only use the real part q_1 of the measured wavevector. To verify that neglecting the imaginary part q_2 does not affect the extracted parameters of the optical conductivity to a large degree, we repeated the fitting procedure used in Fig. 3.3c with $q = q_1 + iq_1/\gamma_\mathrm{p}^{-1}$, where $\gamma_\mathrm{p}^{-1} = q_1/q_2$ is the inverse damping ratio[87]. We find that the introduced damping reduces $\hbar\Omega_\mathrm{exp}$ by only $\approx 2\%$ at $\gamma_\mathrm{p}^{-1} = 5$, which corresponds to the lower bound on γ_p^{-1} extracted from our data.

	$\epsilon_i(\infty)$	s_i	$\hbar\omega_i$ (meV)	$\hbar\gamma_i$ (meV)
$i = \mathrm{x,y}$	4.9	2.001	168.6	0.87
$i = \mathrm{z}$	2.95	0.5262	94.2	0.25

Table A.1.: Parameters of the model of the hBN permittivity.

A.4. Calculation of optical properties of TBG

Here we provide additional plots of the band structure, optical conductivity, and loss function as calculated for different values of the twist angle θ and filling factor ν. The band structure energies $\epsilon_{\mathbf{k},\nu}$ and its wave functions of the single-particle Bloch problem are calculated according to the model in Ref. 38, while the optical conductivity is computed according to the Kubo formula[91] (details provided in Supplementary Note 10 in Ref. 134).

In Fig. A.4 we visualize the impact of the twist angle on the results of our calculations. Upon increasing the twist angle, the interband resonance shifts monotonically to higher energies. The resonance is sharpest and closest to the experimental data discussed in Chapter 3 when the angle is close to the independently measured value $\theta = 1.35°$ despite the absence of any fitting parameter in the theory. These calculations show that a small deviation (0.05°) from the experimentally measured $\theta = 1.35°$ has a modest impact on the resonance energy (compare Figs. A.4d-e and Figs. 3.6c-d). However, due to the relatively flat dispersion, such a small twist-angle variation can have a rather profound effect on the plasmon propagation. Conservation of plasmon energy and momentum is crucial for propagation from the AFM tip to a reflecting interface and backwards[229]. For typical excitation energies used in this work, a change in angle of 0.05° corresponds to a change in plasmon momentum of 10-20 $\mu\mathrm{m}^{-1}$, thus severely blocking propagation. Therefore, we hypothesize that the regions where we observe collective excitations are very homogeneous in twist angle, which might be brought in this state by the AFM-brooming procedure applied to our samples as discussed in Section 2.1 and Appendix A.2.

Figure A.5 shows the effect of changing the carrier density on the optical properties of TBG. Since this model does not include e-e interactions, the bands do not shift in energy upon changing the carrier density, hence only the relative strength of the interband transitions varies. For example, when changing the Fermi level from inside the flat bands (Fig. A.5a-c) to slightly above the single-particle gap (Fig. A.5d-f), the lower interband transition (in orange) quenches due to Pauli blocking, while another transition with slightly lower energy gains in strength. Increasing the carrier density even further beyond the full-filling condition allows transitions at lower energies to become dominant (Fig. A.5g-i).

Despite the pronounced changes in optical conductivity with increasing carrier density (Fig. A.5b,e,h), there are only minor changes in the loss function for different filling factors (Fig. A.5c,f,i). We can understand these differences in a twofold manner. Firstly, a reduction in spectral weight causes a reduction of the group velocity, which is apparent as a change in slope of the resonance (compare Fig. A.5c,f). Secondly, the relative change in spectral weight of the various transitions causes resonances at a different energy to dominate (compare Fig. A.5c,i). Ongoing studies reveal that there are modifications of the band structure upon changing the carrier density once e-e interactions are included[73,91], which is beyond the scope of this thesis.

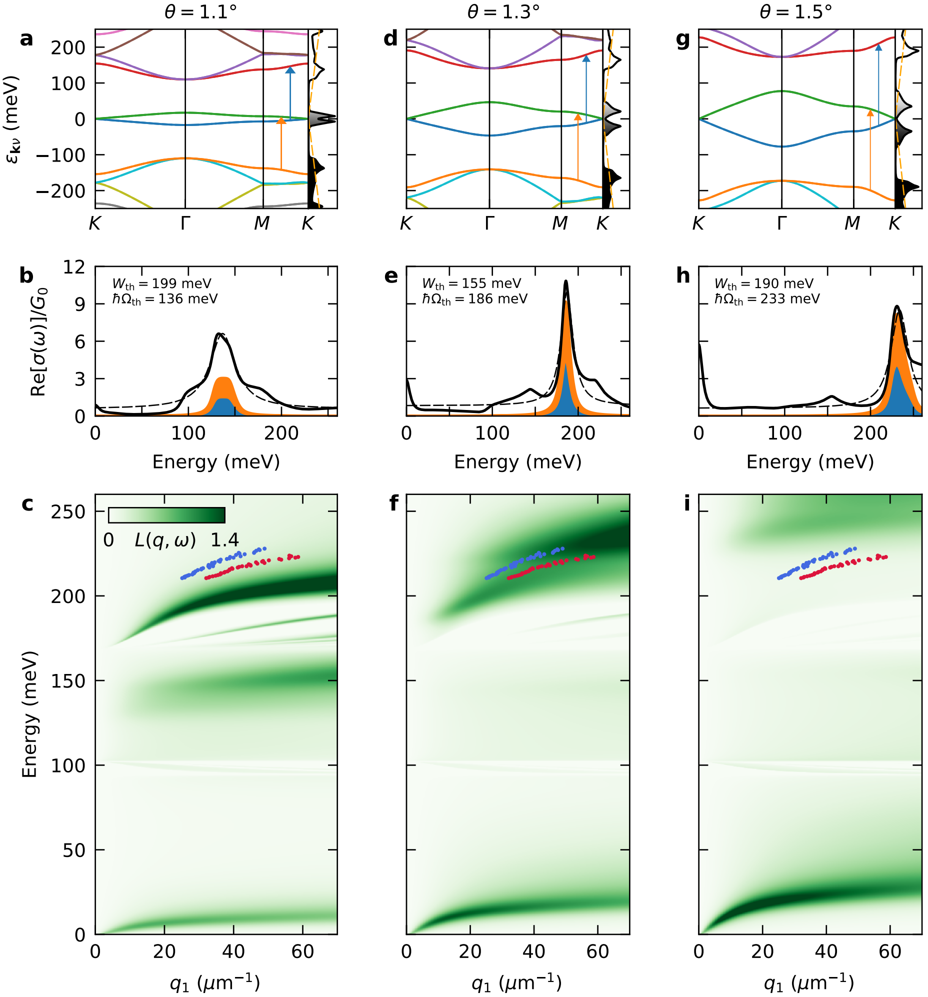

Figure A.4: Impact of twist angle on electronic bands, conductivity, and loss function. **a** Band structure of TBG calculated according to the model in Ref. 38 with $u_0 = 0$ (CS-CM) and $\theta = 1.1°$. Colour coding is the same as in Fig. 3.6**a**. The data points are those extracted from our device with $\theta = 1.35°$ (Fig. 3.3**b**). **b** Optical conductivity derived from the band structure in panel **a**. Colour coding is the same as in Fig. 3.6**b**. **c** Loss function derived from the band structure in panel **a**. Panels **d**-**f** and **g**-**i** are the same as **a**-**c** for $\theta = 1.3°$ and for $\theta = 1.5°$ respectively.

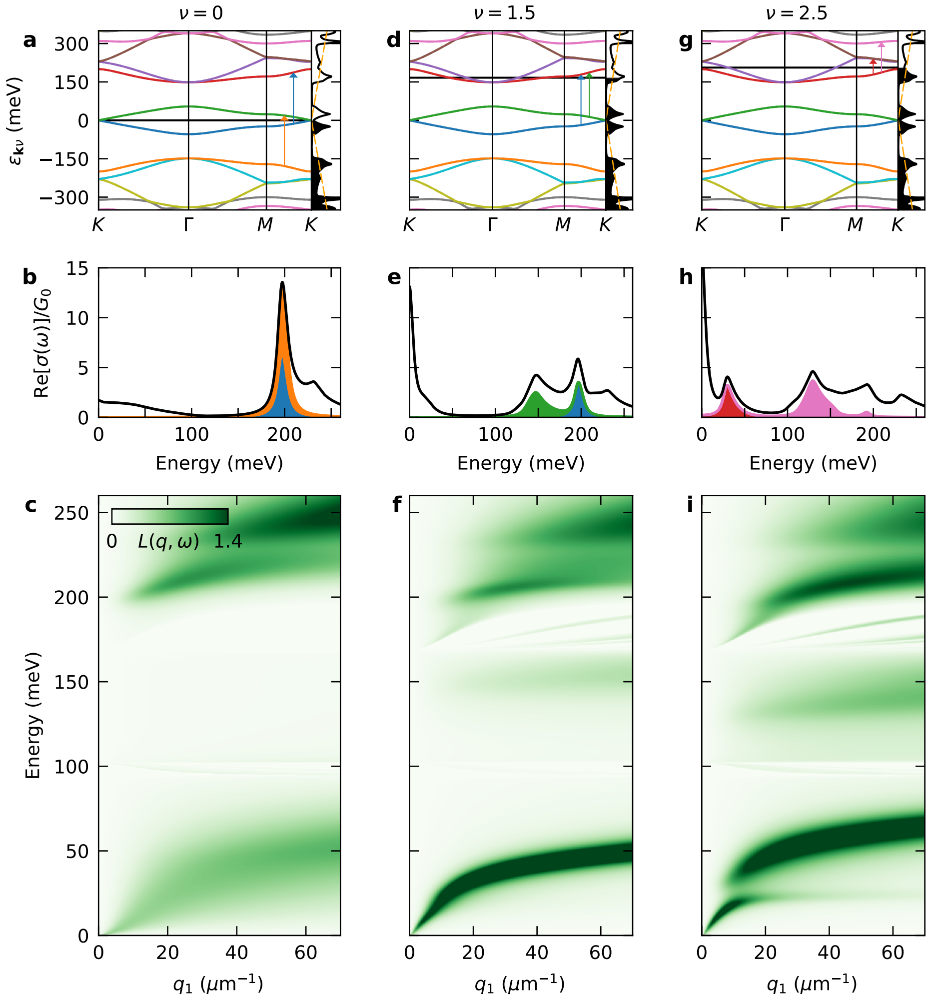

Figure A.5: Optical conductivity and loss function for different filling factors. a Band structure of undoped TBG ($\nu = 0$) calculated according to the model in Ref. 38 with $u_0 = 0$ (CS-CM), $\theta = 1.35°$ and $T = 10$ K. Colour coding is the same as in Fig. 3.6**a**, and the black horizontal line marks the chemical potential. **b** Optical conductivity derived from the band structure in panel **a**. Colour coding is the same as in Fig. 3.6**b**. **c** Loss function derived from the band structure in panel **a**. Panels **d**-**f** and **g**-**i** are the same as **a**-**c** with the chemical potential either slightly or far above the single-particle gap respectively, corresponding to a filling factor of $\nu = 1.5$ and $\nu = 2.5$. In these cases other interband transitions dominate, as indicated with the coloured arrows and shaded areas.

B. Appendices to Chapter 4

B.1. Carrier density calibration through graphene plasmons

In field-effect transistor geometries, the carrier density *n* induced by an applied gate voltage is generally well described by a simple capacitance model. Even so, Hall-effect measurements are usually a pre-requisite in proper characterization of *n* in any conducting system and allows one to make a calibration of the *n* induced by the applied gate voltage V_G. In

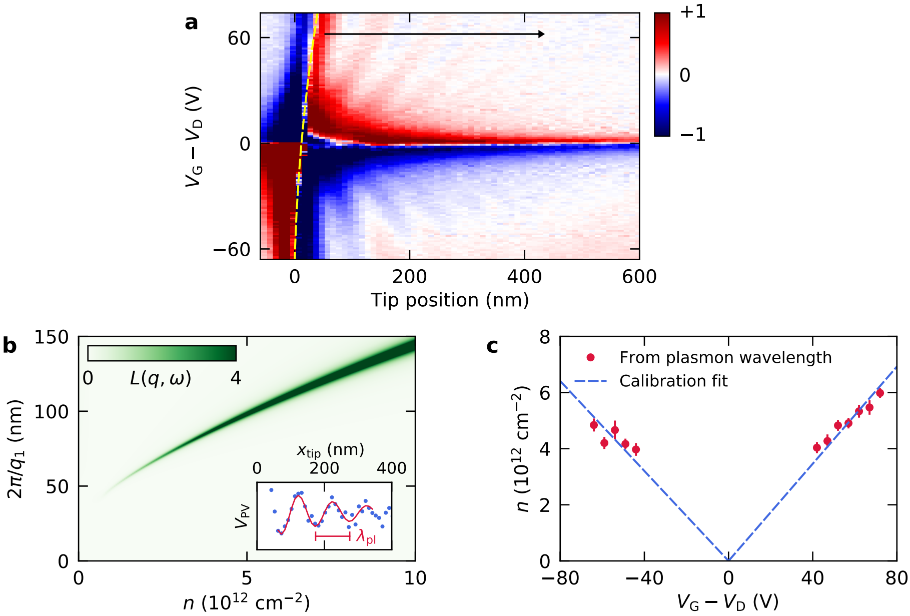

Figure B.1: Estimation of the induced carrier density for an applied gate voltage. a Normalized derivative along the tip position of the measured photovoltage in single-layer graphene near a contact for a range of gate voltages. The contact (extending up to the yellow dashed line) serves as a launcher for plasmon-polaritons in SLG, observed as periodic oscillations in the plot. The excitation energy is 117 meV. **b** Calculated loss function of SLG in our sample at an excitation energy of 117 meV for various carrier densities. The green line corresponds to the plasmon resonance, which changes its wavelength $\lambda_p = 2\pi/q_1$ with carrier density. Inset: measured photovoltage along the arrow in panel **a**, together with a fit (red line) to extract λ_p. **c** Extracted carrier density for various gate voltages based on the data of panel **a** and the calculated dispersion relation shown in panel **b**. The blue dashed lines are linear fits on either side of the CNP, giving an estimation of the induced carrier density at lower gate voltages. The errorbars represent the $\pm 1\sigma$ standard deviation.

some devices, however, measurement geometries are not well suited for Hall measurements. To accurately determine the induced n in such devices, we instead perform a calibration by measuring the plasmon-polariton dispersion in a single-layer graphene (SLG) region. Infrared plasmon-polaritons have been studied extensively in graphene, and their dispersions are well known[87,126,127]. By studying the near-field photocurrent close to a pn-junction, we directly image graphene plasmons, measure their wavelength, and determine the doping level n that such an excitation corresponds to. Moreover, tuning the gate-voltage tunes the plasmon wavelength, which allows us to make a calibration of $n(V_\mathrm{G})$. Fig. B.1a plots a map of the measured photovoltage (we plot the derivative with respect to x_tip to make features clearer) as a function of gate voltage and tip position x_tip, where the x-axis corresponds to a spatial line scan made near one of the Au measurement contacts of our device (purple dot in Fig. 4.1b). The Au-SLG interface is marked by the dashed line in Fig. B.1a. In line with the photothermoelectric effect, the photovoltage changes sign when the gate is tuned through the charge neutrality point of graphene. On top of this, we can also see a set of fringes that become wider spaced at higher gate voltages. They arise from thermoelectric detection[126,127] of the interfering plasmon-polaritons in graphene. To extract the plasmon wavelengths, we follow a method similar to the one described in Sec. 2.4, and involves fitting a polynomial background combined with a sinusoidal function (inset of Fig. B.1b). The corresponding n for the measured plasmon wavelength is then determined from the plasmon dispersion relation (Fig. B.1b) calculated in our sample at the excitation energy used in our measurement (117 meV)[95]. With this method, we obtain the density calibration plotted in Fig. B.1c. It shows a linear behaviour with gate-voltage as expected. We note that n is slightly higher than what is typically expected for the dielectric thickness of our capacitor, which we attribute to photodoping[170] caused by the constant far-field infrared illumination that is unavoidable in our s-SNOM experiments.

B.2. Photoresponse in other mTBG devices/regions

The behaviour reported in Chapter 4 was found to be generic to our other measured mTBG devices. To illustrate this, we plot measured photocurrent maps of another mTBG device (Fig. B.2a). Although slightly more anisotropic, the triangular patterns of the moiré lattice intrinsic to mTBG can be seen and are similar to those measured in the contact configuration used in Fig. 4.3a. We find the same qualitative behaviour including sign changes across certain domain walls, in line with what is expected from the PTE (Fig. 4.5), and the double-step feature at domain wall interfaces (dotted lines in Fig. B.2a).

The measurements presented in Chapter 4 were focused on mTBG with moiré structures of size $\sim$ 500 nm. However, we also observed structures with smaller periodicities. Figure B.2b plots the measured photocurrent of the device presented in Chapter 4, but in the mTBG region on the bottom side of the single-layer graphene region. Again, we find the same periodic patterns in the photocurrent as observed in larger structures. Whilst the seemingly square lattice we observe in Fig. B.2b is not representative of the moiré lattice in mTBG, we recover the triangular lattice (shaded domains) by incorporating the same directional effect as to that reported in the main text (Fig. 4.3a).

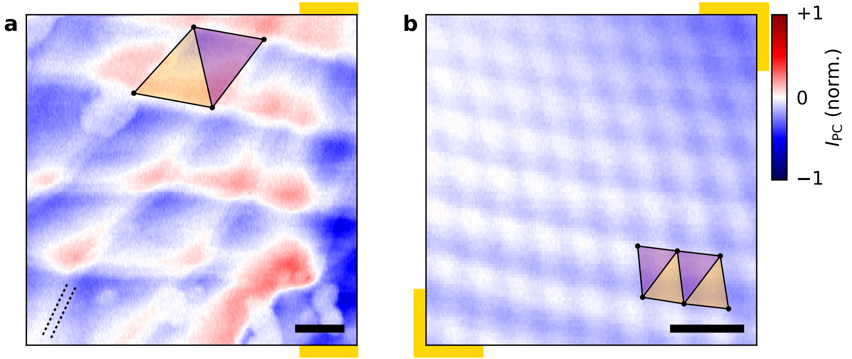

Figure B.2: Near-field photocurrent images in other mTBG devices. **a** Photocurrent image taken in one of our other devices at $E = 117$ meV near charge-neutrality. The profile is qualitatively the same as in Fig. 4.3a, due to a similar arrangement of domain walls with respect to the current path lines between measurement contacts. **b** Photocurrent image of a higher-density network with moiré domains as small as $\sim$ 100 nm, measured at $E = 188$ meV near charge-neutrality. In both panels the yellow/purple triangles indicate the location of AB/BA domains, and the gold patches give a rough indication of the source/drain contacts. Scale bar is 200 nm in both panels.

B.3. Photothermoelectric effect in two dimensions

Our description of the photothermoelectric effect (PTE) is based on two local linear response equations. The first reads

$$\mathbf{J}(\mathbf{r}) = -\sigma(\mathbf{r})\nabla V(\mathbf{r}) - \sigma(\mathbf{r})S(\mathbf{r})\nabla\delta T(\mathbf{r}), \tag{B.1}$$

where $\mathbf{J}(\mathbf{r})$ is the electric current density, $\sigma(\mathbf{r})$ is the local, direct-current (DC) conductivity, $V(\mathbf{r})$ the electric potential, $S(\mathbf{r})$ the Seebeck coefficient, and $\delta T(\mathbf{r}) \equiv T(\mathbf{r}) - T_0$ is the temperature deviation from the substrate temperature T_0, which we assume to be constant. The first term is simply the local form of Ohms law, while the second represents the Seebeck effect, that is, an electric current driven by a temperature gradient.

The second equation involves the heat current density $\mathbf{q}(\mathbf{r})$ and is given by

$$\mathbf{q}(\mathbf{r}) = -\kappa(\mathbf{r})\nabla\delta T(\mathbf{r}) + \Pi(\mathbf{r})\mathbf{J}(\mathbf{r}), \tag{B.2}$$

where $\kappa(\mathbf{r})$ is the thermal conductivity and $\Pi(\mathbf{r}) = T(\mathbf{r})S(\mathbf{r}) \approx T_0S(\mathbf{r})$ is the Peltier coefficient. The first term describes the normal heat conduction (Fourier law) while the second describes the heat current generated by a flowing electric current, known as the Peltier effect.

At steady state, the following continuity equations for the two currents hold

$$\begin{aligned} &\nabla\mathbf{J}(\mathbf{r}) = 0, \\ &\nabla\mathbf{q}(\mathbf{r}) = -g(\mathbf{r})\delta T(\mathbf{r}) + Q(\mathbf{r}). \end{aligned} \tag{B.3}$$

The first equation simply expresses charge conservation, while the second represents heat dissipation to the substrate (first term, $g(\mathbf{r})$ being the thermal coupling to the substrate) or heat generation by light absorption (second term) as described in the main text.

Taking the divergence of Eq. (B.2) and using Eq. (B.3) yields the temperature diffusion equation

$$-\nabla[\kappa(\mathbf{r})\nabla\delta T(\mathbf{r})] + g(\mathbf{r})\delta T(\mathbf{r}) = Q(\mathbf{r}) - T_0\nabla S(\mathbf{r})\mathbf{J}(\mathbf{r}), \tag{B.4}$$

where we can distinguish two source terms: the external heat introduced into the system $Q(\mathbf{r})$ and the heat generated by a flow of electric current via the Peltier effect. Note that the heat generated through the Joule effect by the steady current $\mathbf{J}(\mathbf{r})$ is neglected since it is quadratic in $\mathbf{J}(\mathbf{r})$, and hence quadratic in the absorbed power. If we assume that both κ and g are spatially homogeneous, Eq. (B.4) simplifies to

$$-\nabla^2\delta T(\mathbf{r}) + L_{\text{cool}}^{-2}\delta T(\mathbf{r}) = \frac{1}{\kappa}[Q(\mathbf{r}) - T_0\nabla S(\mathbf{r})\cdot\mathbf{J}(\mathbf{r})], \tag{B.5}$$

where $L_{\text{cool}} \equiv \sqrt{\kappa/g}$ is the cooling length that determines how far the heat can travel in the sample before being lost to the substrate because of out-of-plane conduction.

Equations (B.1-B.5) can be combined into a linear system of Partial Differential Equations (PDEs) in the form

$$-\nabla\left[\begin{pmatrix} \sigma(\mathbf{r}) & T_0\sigma(\mathbf{r})S(\mathbf{r}) \\ T_0\sigma(\mathbf{r})S(\mathbf{r}) & T_0^2\sigma(\mathbf{r})S^2(\mathbf{r}) + T_0\kappa(\mathbf{r}) \end{pmatrix}\begin{pmatrix} \nabla V(\mathbf{r}) \\ T_0^{-1}\nabla\delta T(\mathbf{r}) \end{pmatrix}\right] + \begin{pmatrix} 0 \\ g(\mathbf{r})\delta T(\mathbf{r}) \end{pmatrix} = \begin{pmatrix} 0 \\ Q(\mathbf{r}) \end{pmatrix}. \tag{B.6}$$

Here we put the equations in a form that makes explicit the symmetry of the coefficient matrix due to Onsager relations.

At the m-th contact the voltage has a constant value $V(\mathbf{r}) = V_m$, while the current flowing in it is given as $I_m = \int_{\mathrm{contact}\,m} \mathbf{J}(\mathbf{r}) \cdot \hat{\mathbf{n}} ds$, with $\hat{\mathbf{n}}$ being the outward normal unit vector (we consider positive currents those leaving the device).

In our experiment $V_1 = 0$ and $I_2 = I_3 = 0$ (Fig. 4.6a provides contact numbering). These conditions, together with the boundary conditions on the temperature field $\delta T(\mathbf{r}) = 0$ in the contacts, and $\mathbf{q}(\mathbf{r}) \cdot \hat{\mathbf{n}} = 0$ on the rest of the boundary, specify uniquely the solution[147] of the problem (B.6) given the heat source $Q(\mathbf{r})$.

Solving Eq. (B.6) numerically via finite element method (FEM) allows calculating $V_2[Q]$ and $V_3[Q]$ from the solution. Because of the linearity of the problem it is in principle possible to solve the system (B.6) for a point source located at $\mathbf{r}_0$, defined by $Q_{\mathrm{point}}(\mathbf{r}, \mathbf{r}_0) = \delta(\mathbf{r} - \mathbf{r}_0)$, and obtain the results for a generic source in the form

$$V_{2/3}[Q] = \int d\mathbf{r}_0 \mathcal{R}^{(2/3)}_{\mathrm{PTE}}(\mathbf{r}_0) Q(\mathbf{r}_0), \tag{B.7}$$

where the photovoltage responsivities $\mathcal{R}^{(m)}_{\mathrm{PTE}}(\mathbf{r}_0)$ are obtained by evaluating V_m on the solution corresponding to the point source $Q_{\mathrm{point}}(\mathbf{r}, \mathbf{r}_0)$. This approach is numerically intense, since it requires calculating the solution of Eq. (B.6) one time for every position at which we want to know the responsivities. We can instead make use of the elegant reciprocity principle[147,148] to solve for the responsivities in one shot.

This reciprocity principle affirms, for our experimental configuration, that $\mathcal{R}^{(2)}_{\mathrm{PTE}}(\mathbf{r}_0)$ is equal to the normalized temperature field $\delta T(\mathbf{r})/I_0 T_0$ obtained by solving Eq. (B.6) with $V_1 = 0$, $I_2 = I_0$, and $I_3 = 0$, while $\mathcal{R}^{(3)}_{\mathrm{PTE}}(\mathbf{r}_0)$ is equal to the temperature field obtained by solving Eq. (B.6) with $V_1 = 0$, $I_2 = 0$, and $I_3 = I_0$. Solving these two PDE problems with the FEM code[147] we obtained the responsivity maps shown in the main text. We note that this picture is modified in presence of resonant response (in either the sample or the substrate). In this case $Q(\mathbf{r}, \mathbf{r}_{\mathrm{tip}})$ can spread considerably away from the tip[127] giving rise to additional features.

In the following, we describe the details of the parameters that we feed into the simulations. First, based on sample characterization via AFM/s-SNOM/Raman/photocurrent measurements, we define the sample geometry with specific regions consisting of SLG, and other regions of mTBG (Fig. 4.6a). Next, using the scattering data as a guide (Fig. 4.1c), we draw the network of domains in the region of interest, as reflected by Fig. 4.6b. Using this geometry, we generate a sample mesh with a variable cell size, with those closest to the domain walls having the smallest edge size of about 1.5 nm.

We define at each cell of the mesh the input parameters as follows:

- In mTBG we consider the domain wall to be of the shear-type[33]. This means that we should take the xx-component of the conductivity and Seebeck tensors[56] as defined in Appendix B.4. We evaluate the Seebeck coefficient S_{xx} and and DC conductivity $\sigma_{\mathrm{xx}}(\omega = 0)$ at $T_0 = 300$ K with an energy broadening $\eta = 10$ meV corresponding to a scattering time of ≈ 400 fs.

- In SLG, we use the Mott formula $S(\mu) = -\frac{\pi^2 k_B^2 T}{3e}\frac{1}{\sigma}\frac{d\sigma}{d\mu}$, with $\sigma \propto 1 + \frac{n(\mu)}{n^*}$ as the DC conductivity, $\mu = \hbar\nu\sqrt{\pi n}$, and $n^* = 8 \cdot 10^{10}$ cm^{-2} as the impurity density determined for our device – in agreement with what is expected for graphene on hexagonal-boron nitride[4]. To simulate accurately the influence of SLG in the potential landscape, the conductivity serving as input for the simulation is set to 1.5× the value of AB-stacked BLG, which is a typical for hBN-encapsulated SLG/BLG devices[13].

- The thermal conductivity κ is given at each point using the Wiedemann-Franz law, $\kappa = \frac{\pi^2 k_B^2 T}{3e^2}\sigma$, using the electronic conductivities as defined above.

- The thermal coupling to the substrate is in large part governed via coupling of hot electrons to hBN phonons[230] with a coupling coefficient $g \approx 5 \cdot 10^4$ WK^{-1}m^{-2}. We take this value for the mTBG and SLG regions, leading to a cooling length $L_{\text{cool}} \approx 270$ nm in mTBG. This compares well with the experimental cooling length extracted in mTBG (Appendix B.5).

The FEM simulations of the PTE response of the device were performed using an open-source, homemade, python package (available at gitlab.com/itorre/diffusive_solver)[147] based on the FEniCS library[231], that allows the solution of coupled diffusion equations systems in realistic sample geometries.

B.4. Calculation of thermoelectric transport coefficients in mTBG

The strategy to calculate the relevant thermodynamic quantities of mTBG in the vicinity of domain walls, including the DC conductivity tensor $\sigma_{\alpha\beta}(\omega)$ and the Seebeck tensor $S_{\alpha\beta}$, is outlined in three steps. First, we calculate the band structure for different stacking configurations of bilayer graphene ranging from AB-stacking, to the saddle-point (SP) configuration, and to the BA-stacking. Each of these configurations corresponds to a different displacement vector describing the relative lateral displacement between the two graphene layers, as depicted in Fig. B.3 of a shear-type domain wall. Second, once the band structures are known, we calculate $\sigma_{\alpha\beta}(\omega)$ and $S_{\alpha\beta}$ for each of the stacking configurations. Finally, we define the spatial profile of the displacement vector in mTBG, yielding the spatial profile of $\sigma_{\alpha\beta}(\omega)$ and $S_{\alpha\beta}$.

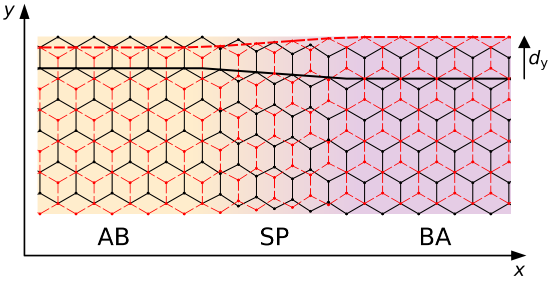

Figure B.3: Local stacking configuration for a shear-type domain wall. The displacement d_y increases by a_0 when translating from an AB region to a BA region, while crossing the saddle-point configuration.

Band structure for bilayer graphene

We calculate the electronic band structure of bilayer graphene with an arbitrary displacement between the two layers. Using the model in Ref. 56, we define the displacement vector $d_y\mathbf{e}_y$ along the y-direction. With d_y defined in units of nearest-neighbour distance $a_0 = 0.142$ nm, $d_y = 1, 1.5, 2$ correspond to AB, SP, BA stacking configurations respectively.

For each stacking configuration between the AB and BA sites, we consider an infinite lattice of that configuration, and solve the eigenvalue problem

$$\mathcal{H}(\mathbf{k})u_\nu(\mathbf{k}) = \epsilon_\nu(\mathbf{k})u_\nu(\mathbf{k}), \tag{B.8}$$

with the effective 4 × 4 Hamiltonian matrix given by

$$\mathcal{H}(\mathbf{k}) = \begin{pmatrix} H_0^+ & U^\dagger \\ U & H_0^- \end{pmatrix}, \tag{B.9}$$

in which H_0 is the Hamiltonian of single-layer graphene (SLG), and U describes the interaction potential between the two layers

$$\begin{aligned} H_0^{\pm} &= \begin{pmatrix} \pm\mathit{\Delta}/2 & \hbar v(\xi k_{\mathrm{x}} + i k_{\mathrm{y}}) \\ \hbar v(\xi k_{\mathrm{x}} - i k_{\mathrm{y}}) & \mp\mathit{\Delta}/2 \end{pmatrix}, \\ U &= \tfrac{\gamma_1}{3}\left(1 + 2\left[\begin{pmatrix} \cos(\frac{2\pi}{3} d_{\mathrm{y}}) & \cos(\frac{2\pi}{3}(d_{\mathrm{y}}+1)) \\ \cos(\frac{2\pi}{3}(d_{\mathrm{y}}-1)) & \cos(\frac{2\pi}{3} d_{\mathrm{y}}) \end{pmatrix}\right]\right). \end{aligned} \tag{B.10}$$

Here $\mathit{\Delta}$ is the interlayer potential energy at each of the two layers, $v \approx 1 \cdot 10^6$ m/s is the band velocity of SLG, $\xi = \pm 1$ selects between the K and K' valley and $\gamma_1 \approx 0.4$ eV is the interlayer coupling. Since we change the carrier density in mTBG solely with one gate, the chemical potential μ is always positioned outside the band gap induced by the out-of-plane displacement field. Therefore, any corrections to this model due to interface states[43,44] are beyond the scope of this work.

In our model we assume the applied back gate voltage fixes the carrier density n everywhere in our mTBG device, and that the chemical potential $\mu(d_{\mathrm{y}}, n)$ varies spatially due to the varying density of states found for different stacking configurations present in the moiré lattice of mTBG. To calculate the chemical potential, we first fix the interlayer potential through a simple capacitance model for bilayer graphene above a backgate. In this model $n(\mathit{\Delta}) = \frac{\epsilon_0}{e^2 d_0}\mathit{\Delta}$, where $d_0 = 0.34$ nm corresponds to the vacuum distance between two layers. Knowing the density of states for every stacking configuration and calculated interlayer potential, we then build a spatial profile of the spatially varying chemical potential in our devices $\mu(d_{\mathrm{y}}, n)$.

Calculation of the Seebeck and conductivity tensors

Following the same definitions as in Ref. 91, we calculate for each stacking configuration the Seebeck tensor $S_{\alpha\beta}$ and the optical conductivity $\sigma_{\alpha\beta}(\omega)$. These tensors relate respectively the heat and current responses in the α direction under an applied electric field in the β direction. The Seebeck tensor is defined under the Relaxation Time Approximation as

$$S_{\alpha\beta} = -\frac{1}{eT}\frac{\mathcal{W}^{(1)}_{\alpha\beta}}{\mathcal{W}^{(0)}_{\alpha\beta}}, \tag{B.11}$$

with

$$\mathcal{W}^{(p)}_{\alpha\beta} \equiv -\pi g \sum_{\nu} \int \frac{\mathrm{d}^2\mathbf{k}}{(2\pi)^2} f'_{\mathbf{k}\nu} \cdot (\epsilon_{\mathbf{k}\nu} - \mu)^p \langle u_{\mathbf{k}\nu}|\partial_{k_\alpha}\mathcal{H}(\mathbf{k})|u_{\mathbf{k}\nu}\rangle\langle u_{\mathbf{k}\nu}|\partial_{k_\beta}\mathcal{H}(\mathbf{k})|u_{\mathbf{k}\nu}\rangle. \tag{B.12}$$

Here, $g = 4$ corresponds to the fourfold valley/spin degeneracy, f' is the derivative of the Fermi-Dirac distribution f. Furthermore, ν counts over the four bands and ∂_{k_j} is the momentum derivative in the direction j. For the electrical conductivity we used the Kubo formula[91] with an energy broadening $\eta = 10$ meV.

Band structure calculations of shifted graphene bilayers and the extraction of the corresponding physical properties were carried out using an open-source python package (available at gitlab.com/itorre/bandstructure-calculation), which allows the computation of the spectrum and of optical and thermoelectric properties of simple electronic band-structure models.

Profile of the displacement vector

Previous work[33] has experimentally determined the profile of the displacement vector $d_{\mathrm{y}}(x_{\mathrm{d}})$ for a distance x_{d} to the middle of a domain wall. This profile can be described as

$$d_{\mathrm{y}}(x_{\mathrm{d}}) = 1 + \frac{2}{\pi}\arctan(e^{\pi x_{\mathrm{d}}/L_{\mathrm{DW}}}) \tag{B.13}$$

with $L_{\mathrm{DW}} = 6.2$ nm encoding the width of a shear domain wall, and $L_{\mathrm{DW}} = 10.1$ nm corresponding to the width of the energetically less-favoured tensile domain wall.

By combining the definitions in this Appendix, we obtain a spatial map of $\sigma_{\alpha\beta}(\omega)$ and $S_{\alpha\beta}$ in a network of domain walls, by evaluating at each position the distance x_{d} to the nearest domain.

B.5. Cooling length in our mTBG devices

The photoresponse generated by the photothermoelectric effect is driven by local temperature gradients generated in the electron gas in the vicinity of inhomogeneities in the Seebeck coefficient, which decay over a characteristic length scale from the source. Microscopically, this corresponds to the distance over which initial photoexcited carriers equilibrate with the lattice and is referred to as the cooling length L_{cool}. In the PTE, a photocurrent can be generated as long as photoexcitation occurs within a typical distance L_{cool} from any junction that exhibits gradients in the Seebeck coefficient. In Bernal stacked bilayer graphene, the cooling length has been measured to be around 250 nm[123]. This is why in our mTBG samples the spatial photocurrent profile is so complex, because thermal gradients generated by photoexcitation in the middle of moiré domains can reach different surrounding junctions, which add linearly and contribute to the globally measured photoresponse. As mentioned in Chapter 4, our samples tend to have extrinsic junctions in the form of stacking faults that also generate photocurrent and, in the case that they are located a distance L_{cool} from the superlattice region, would contribute a background signal to the photoresponse measured in our moiré domains. They could explain, for example, the constant negative photoresponse observed in the moiré domains at high doping levels (Fig. 4.4a and Fig. 4.7a). To rule out such contributions and allow correct interpretation of the photoresponse from moiré domains alone, we studied how the photoresponse from stacking faults behaves and measure L_{cool} in our devices.

Figure B.4a plots an extended photocurrent map of the device presented in Chapter 4 (Fig. 4.7a) at a carrier density $n \sim 4 \cdot 10^{12}$ cm^{-2}, that includes the single-layer graphene (SLG) region. The map clearly shows photocurrent hot spots on one side of the device originating from SLG-mTBG interface (marked by green dotted line), and on the other side from cracks/stacking faults (black dotted line). In between these interfaces we observe the anomalous negative photoresponse in the moiré domains. However, the photocurrent

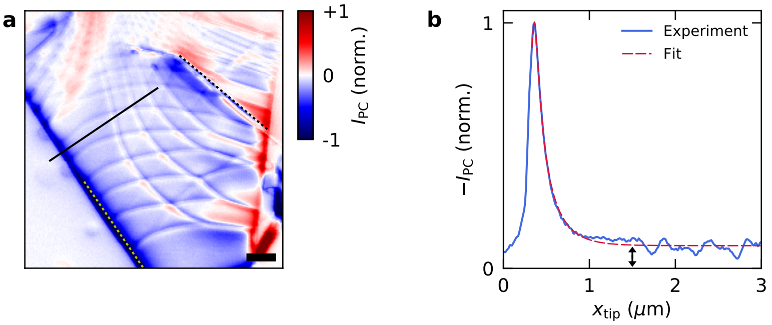

Figure B.4: Extraction of cooling length in mTBG. a Extended photocurrent map of Fig. 4.7**a** ($E = 117$ meV, $n \sim 4 \cdot 10^{12}$ cm^{-2}). The yellow dotted line marks partially marks the interface between SLG on the left side and mTBG on the right side, while the black dotted line marks a crack/stacking fault in our device. Scale bar is 500 nm. **b** Line trace of the photocurrent taken along the black line in panel **a**. The peak in photocurrent marks the position of the SLG-mTBG interface. A fit of the photocurrent profile yields a cooling length of 240 nm, and a background offset whose magnitude is a fraction ~ 0.1 of the photocurrent generated from the SLG-mTBG interface.

hotspots can be seen to decay around 1 μm into the sample, suggesting another possible origin to the photoresponse observed in the moiré domains. To evaluate this, we extracted L_{cool} from the SLG-mTBG interface. Figure B.4b plots a line trace taken across the SLG-mTBG interface that extends a few microns into the mTBG region. Since the photocurrent profile is locally invariant under translations along the SLG-mTBG interface, we use the 1D version of our model of the PTE (Eq. (2.5)). This simplifies the analysis, as the photocurrent on either side of the interface is simply proportional to increase in electron temperature δT (ignoring the domain walls further away) caused by local heating. That said, we should consider that heat spreads radially away from the excitation position, according to the following profile[93]

$$\delta T(x) \propto K_0(\sqrt{((x - x_{\text{tip}})^2 + L_{\text{tip}}^2)}/L_{\text{cool}}), \tag{B.14}$$

where K_0 is the modified Bessel function of the second kind, L_{tip} corrects for the finite radius of the AFM tip, and L_{cool} is the cooling length.

Importantly, we find Eq. (B.14) alone does not describe our experimental data (Fig.B.4b). Instead, a constant offset is needed in our fit of Eq. (B.14) (arrow in Fig.B.4b) to describe the decay of photocurrent from the SLG-mTBG interface. From the decay of the photocurrent we extract $L_{\text{cool}} = 240$ nm. This behaviour, in addition to the constant off-set needed to describe out experimental data, shows that photocurrent generation from the SLG-mTBG is not responsible for the anomalous photocurrent observed at high doping in our devices (Fig. 4.7a).

B.6. Photocurrent effects beyond the photothermoelectric effect

All the experimental evidence discussed in Chapter 4 points towards an explanation of the observed photoresponse data based on the PTE. Indeed, the FEM simulations that include only this effect are in good agreement with experimental data and small discrepancies can be explained by a more complicated Seebeck coefficient profile as suggested by the simplified model in Supplementary Note 7 in Ref. 125. However, even if the general picture is well described by PTE, we cannot completely exclude that other effects contribute small additional corrections.

Here, we comment briefly on two other possible mechanisms of photoresponse generation, namely the photogalvanic effect and the photovoltaic effect. The photogalvanic effect generates a photocurrent thanks to the intrinsic second-order response of the material to the incident electric field that gives rise to a DC current density $\mathbf{j})\mathrm{PG}(\mathbf{r}, \mathbf{r}_{\mathrm{tip}}) \propto |\mathbf{E}(\mathbf{r}, \mathbf{r}_{\mathrm{tip}}, \omega_{\mathrm{ph}})|^2$. Such a response is symmetry-forbidden for homogeneous materials (for unpolarized light) but can play a role in the presence of strong electronic density gradients or strain.

This modifies our Equation (B.1) into

$$\mathbf{J}(\mathbf{r}) = -\sigma(\mathbf{r})\nabla V(\mathbf{r}) - \sigma(\mathbf{r})S(\mathbf{r})\nabla\delta T(\mathbf{r}) + \mathbf{j})\mathrm{PG}(\mathbf{r}, \mathbf{r}_{\mathrm{tip}}), \tag{B.15}$$

adding another source term.

We can write a relation similar to Eq. B.3 for the PGE that reads

$$V_{\mathrm{PGM}}^{(m)} = \int d\mathbf{r} \mathcal{R}_{\mathrm{PGM}}^{(m)}(\mathbf{r}) \cdot \mathbf{j})\mathrm{PG}(\mathbf{r}, \mathbf{r}_{\mathrm{tip}}). \tag{B.16}$$

Again, $\mathcal{R}_{\mathrm{PGM}}^{(m)}(\mathbf{r})$ can be calculated by solving the thermoelectric transport equations using FEM and taking advantage of the Shockley-Ramo theorem[147–149]. In fact, $\mathcal{R}_{\mathrm{PGM}}^{(m)}(\mathbf{r})$ is proportional to the gradient of the potential that would be present in the system in absence of sources and biasing the *m*-th contact with a constant current. Qualitatively, $\mathcal{R}_{\mathrm{PGM}}^{(m)}(\mathbf{r})$ is a smooth vector field flowing mainly in the direction connecting the contacts at which photocurrent is measured. Importantly, the cooling length weakly affects it. As a consequence, we expect PG features (if any) to be sharper with respect to PTE features that are smoothed on the length scale L_{cool}.

We note also that the photovoltaic effect can also play a role in the photoresponse of systems with more than one energy band. Including this effect in our model would require studying a system of three coupled equations including the imbalance density (electron density + holes density) and current. While this is outside the scope of this thesis, we tend to exclude this explanation since photovoltaic contributions should display a threshold behaviour as a function of the photon energy that is not observed in our experimental data.

B.7. Heating from hyperbolic phonon polaritons near domain walls

When the excitation energy lies within the one of the Reststrahlen bands of hBN the optical response is dominated by the hyperbolic phonon polaritons (HPP) of the hBN. The wavevectors of the possible eigenmodes in an hBN slab are given by $q_n(\omega) = q_0(\omega) + n\Delta q(\omega)$, with q_0 representing the wavevector of the zeroth-order mode typically observed in s-SNOM experiments[113,153], followed by equidistant modes separated by Δq, n being an integer. The presence of bilayer graphene minimally affects this spectrum, the main consequence being an additional damping of the modes due to graphene absorption, as we checked numerically using transfer-matrix method[87].

The AFM tip launches in general a linear combination of these modes (like a ray). Ignoring losses and considering for the sake of simplicity a 1D problem ($q_y = 0$), this combination can be written as a Bloch wave $E_x(x,z) = e^{iq_0(x-x_{\text{tip}})}u(x-x_{\text{tip}}, z)$, where u is a periodic function of x with periodicity $\lambda_{\text{ray}} \equiv 2\pi/\Delta q$. The periodicity follows from the constant spacing in momentum space of the modes. Taking into account the y-dimension and losses will introduce a geometrical $1/\sqrt{r}$ attenuation and an exponential damping but will not alter the general picture.

An important question is whether it is more correct to compare the distance d (as determined in Fig. 4.7c) with $2\pi/q_0$ (representing the fundamental eigenmode) or with $2\pi/\Delta q$ (representing the ray-like mode). When measuring an interference pattern from reflected HPPs[79,113,153], it is correct to use $2\pi/q_0$ since the phase $e^{iq_0(x-x_{\text{tip}})}$ is the most important factor in determining the interference. However, our photocurrent generation mechanism is based on the amount of heat that is locally injected into the bilayer graphene. As heating is an incoherent mechanism, it is only sensitive to the intensity pattern encoded in $u(x-x_{\text{tip}})$ while being insensitive to the phase.

In particular, the periodicity of $u(x-x_{\text{tip}})$ creates copies of the field hotspot generated by the tip at distances multiples of λ_{ray}. When one of these copies (the first one) comes close to the domain wall (on the opposite side with respect to the tip), it generates a photocurrent that partially counteracts the one created by the original tip hotspot, leading to a reduction of the signal. Therefore, we fitted d (Fig. 4.7d) with $d(\omega) = a\lambda_{\text{ray}}(\omega)$.

The length λ_{ray} has an intuitive geometrical interpretation in terms of rays travelling at a fixed angle θ_{BN} with respect to the anisotropic z-axis of the hBN[152]. This allows us to express the in-plane phonon-ray wavelength as $\lambda_{\text{ray}} = 2t \cdot \tan(\theta_{\text{BN}})$ where t is the total thickness of the hBN layers, and $\theta_{\text{BM}} = \tan^{-1}\left[\text{Re}\left(\frac{i\sqrt{\epsilon_{x,y}}}{\sqrt{\epsilon_z}}\right)\right]$ determined by the dielectric function ϵ of hBN (in all the calculations we used the model of the hBN dielectric function from Ref. 152).

Interference between the HPPs launched by the tip and waves reflected from the domain wall could in principle modify the heating pattern by producing a reflected Bloch wave $R \cdot e^{-iq_0 x}\tilde{u}(x,z)$, with $\tilde{u}(x,z)$ in general not equal to $u(x,z)$. Such reflected wave could add a component of the injected power with spatial frequency $2q_0$. We expect, however, this effect to be a minor correction with respect to the intensity modulation encoded in $u(x-x_{\text{tip}})$ inside the Reststrahlen band. As we checked numerically[87], the spectrum of HPPs is almost unaffected even when we remove completely the graphene sheet. This means that even a large modification of the optical response of graphene is not likely to strongly reflect waves. Note that this does not conflict with the observation of reflection of

HPPs at domain walls reported in scattering near field experiments[79]. Since the contrast in scattering experiments is only due to interference with the reflected waves even a small reflected wave ($|R| \ll 1$) can produce measurable effects.

The situation is different outside the Reststrahlen band when the periodic structure due to $u(x - x_{\text{tip}})$ is not present anymore and interference between launched and reflected waves can lead to the formation of interferences fringes. Previous s-SNOM studies have shown bright features due to reflected polaritons by domain walls[41,135]. Therefore, we believe that the fringes observed in our data outside the Reststrahlen band of hBN (Fig. 4.2, Fig. 4.4a and Fig. 4.7a) are the result of plasmon polaritons reflection.

C. Appendices to Chapter 5

C.1. Carrier density in bilayer graphene as function of top and bottom gate voltages

Here we derive a minimal model, based on electrostatics and equilibrium of electrochemical potential, to calculate the density of carriers in bilayer graphene (BLG) as a function of top and bottom gate voltages. The main source of deviation from a purely electrostatic behaviour is the quantum capacitance of the semiconducting WSe_2. As this becomes very small when the chemical potential is pushed inside the gap due to the vanishing density of states, it dominates over all the other capacities (summed in series).

In this simplified model we consider both BLG and few-layer WSe_2 as perfect two-dimensional materials neglecting the electrostatic potential drop between the different layers. To be consistent with this assumption we also neglect the modification of the band structure of BLG due to the presence of an out-of-plane field and the corresponding opening of a gap.

Electrostatics

We start by solving the Poisson equation in our structure. Neglecting edge effects this reads

$$-\partial_z[\epsilon_0\epsilon_\perp(z)\partial_z\phi(z)] = \rho(z), \tag{C.1}$$

where $\phi(z)$ is the electrostatic potential as a function of the out-of-plane coordinate z, $\rho(z)$ is the density of charges not bound in dielectrics, $\epsilon_0 \approx 8.85\cdot10^{-12}$ F/m is the vacuum permittivity, and $\epsilon_\perp(z)$ is the relative dielectric permittivity of the structure. This is given by

$$\epsilon_\perp(z) = \begin{cases} \epsilon_{\mathrm{SiO_2}} \approx 4.1 & -t_1 - t_2 < z < -t_2 \\ \epsilon_{\mathrm{hBN}\perp} \approx 3.5 & -t_2 < z < t_3, \end{cases} \tag{C.2}$$

with the permittivities taken from Refs. 232 and 152, and the thicknesses indicated by Fig. C.1. Since no free charge is hosted in the dielectrics, we can write the charge density as

$$\rho(z) = \rho_{\mathrm{WSe_2}}\delta(z - t_3) + \rho_{\mathrm{BLG}}\delta(z) + \rho_{\mathrm{Si}}\delta(z + t_1 + t_2). \tag{C.3}$$

Note that in writing Eq. (C.3) we neglected the charge density that can build up at the hBN-SiO_2 interface due to photodoping[170]. This contribution is difficult to quantify and only results in a rigid shift of the charge neutrality point of BLG.

Because the device is overall charge-neutral, the three surface charge densities sum to zero

$$\rho_{\mathrm{WSe_2}} + \rho_{\mathrm{BLG}} + \rho_{\mathrm{Si}} = 0. \tag{C.4}$$

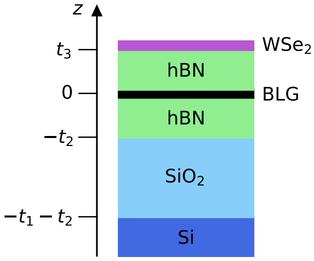

Figure C.1: Schematic of the cross-section of our device. The origin of the z-coordinate is taken at the position of BLG layer. The thicknesses of the layers are $t_1 = 285$ nm, $t_2 = 25$ nm, and $t_3 = 4$ nm (not drawn to scale).

Under the condition of vanishing electric field for $z > t_3$ and $z < -t_1 - t_2$, Eq. (C.1) can be solved yielding a continuous, piecewise linear function

$$\phi(z) = \begin{cases} \phi_{\mathrm{WSe_2}} \frac{z}{t_3} + \phi_{\mathrm{BLG}} \frac{z-t_3}{-t_3} & 0 < z < t_3 \\ \phi_{\mathrm{BLG}} \frac{z+t_2}{t_2} + \phi_{\mathrm{I}} \frac{z}{-t_2} & -t_2 < z < 0 \\ \phi_{\mathrm{I}} \frac{z+t_2+t_1}{t_1} + \phi_{\mathrm{Si}} \frac{z+t_2}{-t_1} & -t_1 - t_2 < z < -t_2, \end{cases} \tag{C.5}$$

where the values of the electrostatic potential at the interfaces are given by

$$\phi_{\mathrm{WSe_2}} = \frac{\rho_{\mathrm{WSe_2}}}{C_{\mathrm{T}}} \tag{C.6}$$

$$\phi_{\mathrm{BLG}} = 0 \tag{C.7}$$

$$\phi_{\mathrm{I}} = \frac{\rho_{\mathrm{Si}} t_2}{\epsilon_0 \epsilon_{\mathrm{hBN}\perp}} \tag{C.8}$$

$$\phi_{\mathrm{Si}} = \frac{\rho_{\mathrm{Si}}}{C_{\mathrm{B}}}. \tag{C.9}$$

Here, we specified the overall additive constant by requiring the electrostatic potential to vanish at the position of the BLG layer, while the two capacities are given by $C_{\mathrm{T}} = \epsilon_0 \epsilon_{\mathrm{hBN}\perp}/t_3 \approx 7.7\ \mathrm{mF/m^2}$ and $C_{\mathrm{B}} = [(\epsilon_0 \epsilon_{\mathrm{hBN}\perp}/t_2)^{-1} + (\epsilon_0 \epsilon_{\mathrm{SiO_2}}/t_1)^{-1}]^{-1} \approx 0.12\ \mathrm{mF/m^2}$.

Quantum capacitances

The equilibrium conditions between the different layers are expressed in terms of the electrochemical potential φ. For each layer, this is defined as

$$-e\varphi_\alpha = -e\phi_\alpha + \mu_\alpha, \tag{C.10}$$

where e is the unit charge, $\alpha = \mathrm{WSe_2}, \mathrm{BLG}, \mathrm{Si}$ and μ_α is the chemical potential measured from the vacuum level. To solve this set of equations, we need a relation between the charge density and the chemical potential in each layer.

In silicon, owing to the large density of states, we can neglect the shift in chemical potential due to the induced charge density. Therefore, the chemical potential stays at a fixed value given by the negative of the work function of silicon W_{Si}, in other words,

$$\mu_{\mathrm{Si}} \approx -W_{\mathrm{Si}}. \tag{C.11}$$

In BLG the charge density can be expressed as

$$\rho_{\mathrm{BLG}} = -e(n_{\mathrm{BLG}} - \bar{n}_{\mathrm{BLG}}), \tag{C.12}$$

where n_{BLG} is the density of mobile carriers (electrons−holes) that determines the measured plasmon dispersion and $e\bar{n}_{\mathrm{BLG}}$ is the residual charge density that is left in BLG when the Fermi level is at the Dirac point due to impurity doping. In the following, bars will denote quantities related to the isolated materials. Approximating the first valence and conduction bands of BLG in the vicinity of the Dirac point by parabolic bands yields an energy-independent density of states[156] given by $g = 2m^*/(\pi\hbar^2)$ with $m^* \approx 0.046\ m_{\mathrm{e}}$, m_{e} being the bare electron mass, and taking a fourfold spin/valley degeneracy into account. This allows us to calculate n_{BLG} as function of μ_{BLG} at temperature T as

$$n_{\mathrm{BLG}}(\mu_{\mathrm{BLG}}) = g\left[I(\mu_{\mathrm{BLG}} - E_{\mathrm{D}}, k_{\mathrm{B}}T) - I(-\mu_{\mathrm{BLG}} + E_{\mathrm{D}}, k_{\mathrm{B}}T)\right] = g(\mu_{\mathrm{BLG}} - E_{\mathrm{D}}), \tag{C.13}$$

where $E_{\mathrm{D}} \approx -4.5$ eV is the energy of the Dirac point of BLG measured from the vacuum level, k_{B} is the Boltzmann constant, and

$$I(\mu, k_{\mathrm{B}}T) = \int_0^{\infty} \frac{\mathrm{d}E}{1 + e^{(E-\mu)/(k_{\mathrm{B}}T)}} = k_{\mathrm{B}}T \ln\left(1 + e^{\frac{\mu}{k_{\mathrm{B}}T}}\right) \underset{T\to 0}{\approx} \theta(\mu)\mu. \tag{C.14}$$

Imposing that BLG is electrically neutral when the chemical potential equals the negative of the work function of isolated BLG, $\bar{W}_{\mathrm{BLG}}$, we obtain

$$-eg(-\bar{W}_{\mathrm{BLG}} - E_{\mathrm{D}}) + e\bar{n}_{\mathrm{BLG}} = 0, \tag{C.15}$$

that we can use to eliminate E_{D} in Eq. (C.13). Solving for the chemical potential gives

$$\mu_{\mathrm{BLG}} = -\bar{W}_{\mathrm{BLG}} + \frac{e^2}{C_{\mathrm{Q}}}(n_{\mathrm{BLG}} - \bar{n}_{\mathrm{BLG}}), \tag{C.16}$$

where $C_{\mathrm{Q}} = e^2 g \approx 62\ \mathrm{mF/m^2}$ is the quantum capacitance of BLG.

Similarly, in $\mathrm{WSe_2}$ we can write the charge density as

$$\rho_{\mathrm{WSe_2}} = -e(n_{\mathrm{WSe_2}} - e\bar{n}_{\mathrm{WSe_2}}), \tag{C.17}$$

where $n_{\mathrm{WSe_2}}$ is the number of mobile carriers in the bands and $e\bar{n}_{\mathrm{WSe_2}}$ is a residual charge density due to doping. Again, by approximating the relevant bands with an effective mass we get constant densities of states in the conduction and valence bands $g_{\mathrm{c/v}}$, and the carrier density as function of $\mu_{\mathrm{WSe_2}}$ can be calculated according to

$$n_{\mathrm{WSe_2}}(\mu_{\mathrm{WSe_2}}) = g_{\mathrm{c}} I(\mu_{\mathrm{WSe_2}} - E_{\mathrm{c}}, k_{\mathrm{B}}T) - g_{\mathrm{v}} I(E_{\mathrm{v}} - \mu_{\mathrm{WSe_2}}, k_{\mathrm{B}}T), \tag{C.18}$$

where $E_{\mathrm{c/v}}$ are the edges of the conduction/valence band edges measured from the vacuum level. Imposing charge neutrality when the chemical potential equals minus the work function of isolated $\mathrm{WSe_2}$ gives

$$\bar{n}_{\mathrm{WSe_2}} = g_{\mathrm{c}} I(-\bar{W}_{\mathrm{WSe_2}} - E_{\mathrm{c}}, k_{\mathrm{B}}T) - g_{\mathrm{v}} I(E_{\mathrm{v}} + \bar{W}_{\mathrm{WSe_2}}, k_{\mathrm{B}}T). \tag{C.19}$$

In the following we will express the chemical potential of $\mathrm{WSe_2}$ in terms of a deviation $\Delta\bar{\mu}_{\mathrm{WSe_2}}$ from its value in pristine $\mathrm{WSe_2}$, in other words

$$\mu_{\mathrm{WSe_2}} = -\bar{W}_{\mathrm{WSe_2}} + \Delta\bar{\mu}_{\mathrm{WSe_2}}. \tag{C.20}$$

Equilibrium of electrochemical potential

The voltage source connected at the bottom gate fixes the electrochemical potential difference between BLG and silicon to be

$$\varphi_{\mathrm{Si}} - \varphi_{\mathrm{BLG}} = V_{\mathrm{B}}, \tag{C.21}$$

and by substituting Eqs. (C.9,C.7,C.11,C.16) we can extract the silicon surface charge density

$$\rho_{\mathrm{Si}} = C_{\mathrm{B}} \left(V_{\mathrm{B}} - \bar{V}_{\mathrm{B}} - e\frac{n_{\mathrm{BLG}} - \bar{n}_{\mathrm{BLG}}}{C_{\mathrm{Q}}} \right), \tag{C.22}$$

where $\bar{V}_{\mathrm{B}} = (W_{\mathrm{Si}} - \bar{W}_{\mathrm{BLG}})/e$.

In a similar way we can write for the top-gate voltage

$$\varphi_{\mathrm{WSe}_2} - \varphi_{\mathrm{BLG}} = V_{\mathrm{T}}, \tag{C.23}$$

and, substituting Eqs. (C.6,C.7,C.16,C.20), solve for the WSe_2 charge density

$$\rho_{\mathrm{WSe}_2} = C_{\mathrm{T}} \left(V_{\mathrm{T}} - \bar{V}_{\mathrm{T}} + \frac{\Delta\bar{\mu}_{\mathrm{WSe}_2}}{e} - e\frac{n_{\mathrm{BLG}} - \bar{n}_{\mathrm{BLG}}}{C_{\mathrm{Q}}} \right). \tag{C.24}$$

Here, $\bar{V}_{\mathrm{T}} = (\bar{W}_{\mathrm{WSe}_2} - \bar{W}_{\mathrm{BLG}})/e$.

Substituting Eqs. (C.12,C.22,C.24) into the charge neutrality condition given by Eq. (C.4) yields

$$\left(1 + \frac{C_{\mathrm{T}}}{C_{\mathrm{Q}}} + \frac{C_{\mathrm{B}}}{C_{\mathrm{Q}}}\right) e(n_{\mathrm{BLG}} - \bar{n}_{\mathrm{BLG}}) = C_{\mathrm{T}}(V_{\mathrm{T}} - \bar{V}_{\mathrm{T}}) + C_{\mathrm{B}}(V_{\mathrm{B}} - \bar{V}_{\mathrm{B}}) + \frac{C_{\mathrm{T}}}{e}\Delta\bar{\mu}_{\mathrm{WSe}_2}, \tag{C.25}$$

which, together with the equation obtained by eliminating ρ_{WSe_2} from Eqs. (C.17) and (C.24),

$$-en_{\mathrm{WSe}_2}[-\bar{W}_{\mathrm{WSe}_2} + \Delta\bar{\mu}_{\mathrm{WSe}_2}] + e\bar{n}_{\mathrm{WSe}_2} = C_{\mathrm{T}} \left(V_{\mathrm{T}} - \bar{V}_{\mathrm{T}} + \frac{\Delta\bar{\mu}_{\mathrm{WSe}_2}}{e} - e\frac{n_{\mathrm{BLG}} - \bar{n}_{\mathrm{BLG}}}{C_{\mathrm{Q}}} \right), \tag{C.26}$$

constitutes a system of two non-linear equations in the two variables n_{BLG} and $\Delta\bar{\mu}_{\mathrm{WSe}_2}$ that can be solved numerically.

However, before solving these equations we exploit the fact that $C_{\mathrm{Q}} \gg C_{\mathrm{T}}, C_{\mathrm{B}}$ and take the limit $C_{\mathrm{Q}} \to \infty$. This gives

$$e(n_{\mathrm{BLG}} - \bar{n}_{\mathrm{BLG}}) = C_{\mathrm{T}}(V_{\mathrm{T}} - \bar{V}_{\mathrm{T}}) + C_{\mathrm{B}}(V_{\mathrm{B}} - \bar{V}_{\mathrm{B}}) + \frac{C_{\mathrm{T}}}{e}\Delta\bar{\mu}_{\mathrm{WSe}_2}, \tag{C.27}$$

$$-en_{\mathrm{WSe}_2}(-\bar{W}_{\mathrm{WSe}_2} + \Delta\bar{\mu}_{\mathrm{WSe}_2}) + e\bar{n}_{\mathrm{WSe}_2} = C_{\mathrm{T}} \left(V_{\mathrm{T}} - \bar{V}_{\mathrm{T}} + \frac{\Delta\bar{\mu}_{\mathrm{WSe}_2}}{e} \right). \tag{C.28}$$

Note that in this approximation the latter equation does not depend on V_{B}.

To simplify the analysis of experimental results the zero bias situation ($V_{\mathrm{B}} = V_{\mathrm{T}} = 0$) is useful as a reference in our equations instead of the flat vacuum level situation ($V_{\mathrm{B}} = \bar{V}_{\mathrm{B}}$, $V_{\mathrm{T}} = \bar{V}_{\mathrm{T}}$). This can be done by defining $\Delta\bar{\mu}^0_{\mathrm{WSe}_2}$ as the solution of

$$-en_{\mathrm{WSe}_2}(-\bar{W}_{\mathrm{WSe}_2} + \Delta\bar{\mu}^0_{\mathrm{WSe}_2}) + e\bar{n}_{\mathrm{WSe}_2} = C_{\mathrm{T}} \left(-\bar{V}_{\mathrm{T}} + \frac{\Delta\bar{\mu}^0_{\mathrm{WSe}_2}}{e} \right). \tag{C.29}$$

Subtracting Eq. (C.29) from Eq. (C.28), and defining $W^0_{\mathrm{WSe_2}} = \bar{W}_{\mathrm{WSe_2}} - \Delta\bar{\mu}^0_{\mathrm{WSe_2}}$, and $\Delta\mu_{\mathrm{WSe_2}} = \Delta\bar{\mu}_{\mathrm{WSe_2}} - \Delta\mu^0_{\mathrm{WSe_2}}$, gives our final equation that defines the chemical potential shift $\Delta\mu_{\mathrm{WSe_2}}$

$$\boxed{n_{\mathrm{WSe_2}}(\Delta\mu_{\mathrm{WSe_2}} - W^0_{\mathrm{WSe_2}}) - n_{\mathrm{WSe_2}}(-W^0_{\mathrm{WSe_2}}) = -\frac{C_\mathrm{T}}{e}\left(V_\mathrm{T} + \frac{\Delta\mu_{\mathrm{WSe_2}}}{e}\right).} \tag{C.30}$$

The result can then be fed into

$$\boxed{n_{\mathrm{BLG}} = \frac{C_\mathrm{B}(V_\mathrm{B} - V_\mathrm{D})}{e} + \frac{C_\mathrm{T} V_\mathrm{T}}{e} + \frac{C_\mathrm{T}\Delta\mu_{\mathrm{WSe_2}}(V_\mathrm{T})}{e^2},} \tag{C.31}$$

that is derived from Eq. (C.27) by defining $-C_\mathrm{B} V_\mathrm{D}/e = \bar{n}_{\mathrm{BLG}} - C_\mathrm{B}\bar{V}_\mathrm{B}/e - C_\mathrm{T}\bar{V}_\mathrm{T}/e + C_\mathrm{T}\Delta\mu^0_{\mathrm{WSe_2}}/e^2$. Here $n^0_{\mathrm{BLG}} = -C_\mathrm{B} V_\mathrm{D}/e$ is the residual carrier density in BLG when $V_\mathrm{B} = V_\mathrm{T} = 0$, effectively accounting for the offset in the Dirac point V_D due to for instance photodoping.

Solution of Eqs. (C.30,C.31)

To solve Eq. (C.30) for $\Delta\mu_{\mathrm{WSe_2}}$ as a function of V_T requires in general the use of a numerical root finding method. However, it is instructive to look at the zero-temperature limit where an analytical solution can be derived. Making use of Eq. (C.14) the left hand side of Eq. (C.30) simplifies, at zero temperature, to

$$n_{\mathrm{WSe_2}}(\Delta\mu_{\mathrm{WSe_2}} - W^0_{\mathrm{WSe_2}}) - n_{\mathrm{WSe_2}}(-W^0_{\mathrm{WSe_2}}) = \begin{cases} g_\mathrm{v}(\Delta\mu_{\mathrm{WSe_2}} + eV_\mathrm{v}) & \Delta\mu_{\mathrm{WSe_2}} < -eV_\mathrm{v} \\ 0 & -eV_\mathrm{v} \leq \Delta\mu_{\mathrm{WSe_2}} \leq -eV_\mathrm{c} \\ g_\mathrm{c}(\Delta\mu_{\mathrm{WSe_2}} + eV_\mathrm{c}) & \Delta\mu_{\mathrm{WSe_2}} > -eV_\mathrm{c}, \end{cases} \tag{C.32}$$

where $V_\mathrm{c} = -(E_\mathrm{c} + W^0_{\mathrm{WSe_2}})/e$ and $V_\mathrm{v} = -(E_\mathrm{v} + W^0_{\mathrm{WSe_2}})/e$. This expression is plotted in Figure C.2a as dashed line together with the right-hand side of Eq. (C.30) calculated for three different values of V_T.

The solution of Eq. (C.30) in the zero-temperature limit can be obtained by the intersection of these two curves and gives a piecewise linear function

$$\Delta\mu_{\mathrm{WSe_2}}(V_\mathrm{T}) = \begin{cases} \frac{-eV_\mathrm{c} - eV_\mathrm{T}\frac{C_\mathrm{T}}{e^2 g_\mathrm{c}}}{1 + \frac{C_\mathrm{T}}{e^2 g_\mathrm{c}}} \approx -eV_\mathrm{c} & V_\mathrm{T} < V_\mathrm{c} \\ -eV_\mathrm{T} & V_\mathrm{c} \leq V_\mathrm{T} \leq V_\mathrm{v} \\ \frac{-eV_\mathrm{v} - eV_\mathrm{T}\frac{C_\mathrm{T}}{e^2 g_\mathrm{v}}}{1 + \frac{C_\mathrm{T}}{e^2 g_\mathrm{v}}} \approx -eV_\mathrm{v} & V_\mathrm{T} > V_\mathrm{v}, \end{cases} \tag{C.33}$$

where we made use of $e^2 g_{\mathrm{v,v}} \gg C_\mathrm{T}$. Figure C.2a also displays the finite-temperature curve showing that at finite temperature the solution is always closer to zero than the zero-temperature one.

Based on this, we can compare in Fig. C.2b the full numerical result at finite temperature with the analytical, zero-temperature approximation. We see that both solutions agree qualitatively, showing a linear behaviour for values of the top-gate voltage inside the $\mathrm{WSe_2}$ gap and saturation at the conduction and valence band edges. However, finite temperature effects substantially reduce the value of $\Delta\mu_{\mathrm{WSe_2}}$ near the band edges.

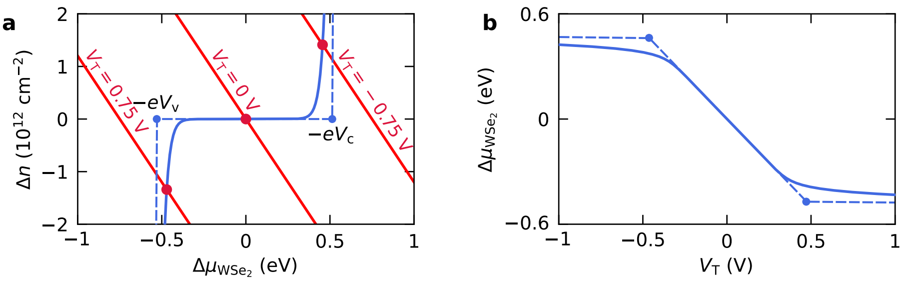

Figure C.2: Graphical solution of Eq. (C.30). **a** The dashed/solid blue curve represents the left hand side of Eq. (C.30) evaluated at zero/room temperature, while the red lines represent the the right hand side of Eq. (C.30) for three different values of V_T. **b** The solid line displays $\Delta\mu_{WSe_2}$ as a function of V_T calculated by solving numerically Eq. (C.30), while the dashed line corresponds to the zero-temperature solution given by Eq. (C.33). Both plots make use of the fit parameters as extracted in Fig. C.3.

Finally, from Eq. (C.31) we can calculate the shift in carrier density Δn produced by the application of V_T. Again, in the zero temperature limit, this gives

$$\Delta n_{BLG} = n_{BLG} - \frac{C_B(V_B - V_D)}{e} = \frac{C_T}{e} \times \begin{cases} V_T - V_c & V_T < V_c \\ 0 & V_v \leq V_T \leq V_v \\ V_T - V_V & V_T > V_v. \end{cases} \tag{C.34}$$

We compare the analytical solution with the full numerical solution and experimental data in Figure C.3, based on the parameters as determined by a fit of our data with the full numerical solution. In this fit, V_v and V_c are free parameters, while we fix $g_v = g_c = 5.2$ eV^{-1}nm^{-2} and $C_T = 7.7$ mF/m^2. This density of states of WSe$_2$ is estimated based on the effective mass $\approx 1.2 m_e$ measured in trilayer WSe$_2$[175] and is similar to the calculated value for monolayer WSe$_2$[233]. The fit result is only affected to a large extent when $g_{c/v}$ changes by an order of magnitude or more and, therefore, a small deviation from its actual value is irrelevant to our analysis. We finally note that leaving the top gate capacitance as free parameter leads to a slight underestimation of the band gap in WSe$_2$.

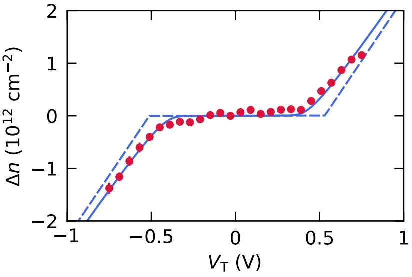

Figure C.3: Carrier density induced by the application of a top-gate voltage. The experimental data is fit to our model according to Eq. (C.30), as shown by the solid line. Making use of the same fit parameters, the dashed curve shows the zero-temperature solution as in Eq. (C.33).

Publications

Large parts of this Thesis are based on the following publications:

Ch. 3 N.C.H. Hesp[†], I. Torre[†], D. Rodan-Legrain[†], P. Novelli[†], Y. Cao, S. Carr, S. Fang, P. Stepanov, D. Barcons Ruiz, H. Herzig Sheinfux, K. Watanabe, T. Taniguchi, D.K. Efetov, E. Kaxiras, P. Jarillo-Herrero, M. Polini, F.H.L. Koppens. Observation of interband collective excitations in twisted bilayer graphene. *Nature Physics* (2021).

Ch. 4 N.C.H. Hesp, I. Torre, D. Barcons Ruiz, H. Herzig Sheinfux, K. Watanabe, T. Taniguchi, R. Krishna Kumar, F.H.L. Koppens. Nano-imaging photoresponse in a moiré unit cell of minimally twisted bilayer graphene. *Nature Communications* **12**, 1640 (2021).

Ch. 5 N.C.H. Hesp, I. Torre, K. Watanabe, T. Taniguchi, F.H.L. Koppens. WSe_2 as transparent top gate for near-field experiments. In preparation.

Ch. 7 N.C.H. Hesp[†], P. Stepanov[†], S. Batlle, K. Watanabe, T. Taniguchi, F.H.L. Koppens. Imaging broken inversion symmetry in magic-angle twisted bilayer graphene. In preparation.

Ch. 8 N.C.H. Hesp, P. Stepanov, S. Batlle, D. Rodan-Legrain, I. Torre, H. Agarwal, R. Krishna Kumar, K. Watanabe, T. Taniguchi, P. Jarillo-Herrero, F.H.L. Koppens. Probing twist angle variations in twisted bilayer graphene with photocurrent nanoscopy. In preparation.

Other publications by the author:

- H. Herzig Sheinfux, L. Orsini, M. Jung, I. Torre, M. Ceccanti, R. Maniyara, D. Barcons Ruiz, A. Hötger, S. Castilla, N.C.H. Hesp, E. Janzen, A. Holleitner, V. Pruneri, J.H. Edgar, G. Shvets, F.H.L. Koppens. Multimodal reflection and bound in the continuum modes in indirectly-patterned hyperbolic cavities. In preparation.
- A. Block, A. Principi, N.C.H. Hesp, A.W. Cummings, M. Liebel1, K. Watanabe, T.Taniguchi, S. Roche, F.H.L. Koppens, N.F. van Hulst, K. Tielrooij. Observation of giant and tunable thermal diffusivity of a Dirac fluid at room temperature. *Nature Nanotechnology* (2021).
- K. Tielrooij[†], N.C.H. Hesp[†], A. Principi, M.B. Lundeberg, E.A.A. Pogna, L. Banszerus, Z. Mics, M. Massicotte, P. Schmidt, D. Davydovskaya, D.G. Purdie, I. Goykhman, G. Soavi, A. Lombardo, K. Watanabe, T. Taniguchi, M. Bonn, D. Turchinovich, C. Stampfer, A.C. Ferrari, G. Cerullo, M. Polini, F.H.L. Koppens. Out-of-plane heat transfer in van der Waals stacks through electron–hyperbolic phonon coupling. *Nature Nanotechnology* **13**, 41–46 (2018).
- A. Principi, M.B. Lundeberg, N.C.H. Hesp, K. Tielrooij, F.H.L. Koppens, M. Polini. Super-Planckian Electron Cooling in a van der Waals Stack. *Physical Review Letters* **118**, 126804 (2017).

[†] These authors contributed equally.

Bibliography

[1] Novoselov, K. S. et al. Two-dimensional gas of massless Dirac fermions in graphene. *Nature* **438**, 197–200 (2005).

[2] Geim, A. K. & Novoselov, K. S. The rise of graphene. *Nature Materials* **6**, 183–191 (2007).

[3] Geim, A. K. & Grigorieva, I. V. Van der Waals heterostructures. *Nature* **499**, 419–425 (2013).

[4] Dean, C. R. et al. Boron nitride substrates for high-quality graphene electronics. *Nature Nanotechnology* **5**, 722–726 (2010).

[5] Manzeli, S., Ovchinnikov, D., Pasquier, D., Yazyev, O. V. & Kis, A. 2D transition metal dichalcogenides. *Nature Reviews Materials* **2**, 17033 (2017).

[6] Yu, Y. et al. High-temperature superconductivity in monolayer $Bi_2Sr_2CaCu_2O_8$. *Nature* **575**, 156–163 (2019).

[7] Huang, B. et al. Layer-dependent ferromagnetism in a van der Waals crystal down to the monolayer limit. *Nature* **546**, 270–273 (2017).

[8] Mayorov, A. S. et al. Micrometer-Scale Ballistic Transport in Encapsulated Graphene at Room Temperature. *Nano Letters* **11**, 2396–2399 (2011).

[9] Wang, L. et al. One-Dimensional Electrical Contact to a Two-Dimensional Material. *Science* **342**, 614–617 (2013).

[10] Ponomarenko, L. a. et al. Cloning of Dirac fermions in graphene superlattices. *Nature* **497**, 594–597 (2013).

[11] Dean, C. R. et al. Hofstadter's butterfly and the fractal quantum Hall effect in moiré superlattices. *Nature* **497**, 598–602 (2013).

[12] Hunt, B. et al. Massive Dirac Fermions and Hofstadter Butterfly in a van der Waals Heterostructure. *Science* **340**, 1427–1430 (2013).

[13] Bandurin, D. A. et al. Negative local resistance caused by viscous electron backflow in graphene. *Science* **351**, 1055–1058 (2016).

[14] Crossno, J. et al. Observation of the Dirac fluid and the breakdown of the Wiedemann-Franz law in graphene. *Science* **351**, 1058–1061 (2016).

[15] Cao, Y. et al. Superlattice-Induced Insulating States and Valley-Protected Orbits in Twisted Bilayer Graphene. *Physical Review Letters* **117**, 116804 (2016).

[16] Kim, K. et al. van der Waals Heterostructures with High Accuracy Rotational Alignment. *Nano Letters* **16**, 1989–1995 (2016).

[17] Bistritzer, R. & MacDonald, A. H. Moiré bands in twisted double-layer graphene. *Proceedings of the National Academy of Sciences* **108**, 12233–12237 (2011).

[18] Cao, Y. et al. Unconventional superconductivity in magic-angle graphene superlattices. *Nature* **556**, 43–50 (2018).

[19] Lopes dos Santos, J. M. B., Peres, N. M. R. & Castro Neto, A. H. Graphene Bilayer with a Twist: Electronic Structure. *Physical Review Letters* **99**, 256802 (2007).

[20] Suárez Morell, E., Correa, J. D., Vargas, P., Pacheco, M. & Barticevic, Z. Flat bands in slightly twisted bilayer graphene: Tight-binding calculations. *Physical Review B* **82**, 121407 (2010).

[21] Li, G. et al. Observation of Van Hove singularities in twisted graphene layers. *Nature Physics* **6**, 109–113 (2010).

[22] Cao, Y. et al. Correlated insulator behaviour at half-filling in magic-angle graphene superlattices. *Nature* **556**, 80–84 (2018).

[23] Yankowitz, M. et al. Tuning superconductivity in twisted bilayer graphene. *Science* **363**, 1059–1064 (2019).

[24] Lu, X. et al. Superconductors, orbital magnets and correlated states in magic-angle bilayer graphene. *Nature* **574**, 653–657 (2019).

[25] Sharpe, A. L. et al. Emergent ferromagnetism near three-quarters filling in twisted bilayer graphene. *Science* **365**, 605–608 (2019).

[26] Serlin, M. et al. Intrinsic quantized anomalous Hall effect in a moiré heterostructure. *Science* **367**, 900–903 (2020).

[27] Tomarken, S. L. et al. Electronic Compressibility of Magic-Angle Graphene Superlattices. *Physical Review Letters* **123**, 046601 (2019).

[28] Choi, Y. et al. Electronic correlations in twisted bilayer graphene near the magic angle. *Nature Physics* **15**, 1174–1180 (2019).

[29] Kerelsky, A. et al. Maximized electron interactions at the magic angle in twisted bilayer graphene. *Nature* **572**, 95–100 (2019).

[30] Xie, Y. et al. Spectroscopic signatures of many-body correlations in magic-angle twisted bilayer graphene. *Nature* **572**, 101–105 (2019).

[31] Jiang, Y. et al. Charge order and broken rotational symmetry in magic-angle twisted bilayer graphene. *Nature* **573**, 91–95 (2019).

[32] Lopes dos Santos, J. M. B., Peres, N. M. R. & Castro Neto, A. H. Continuum model of the twisted graphene bilayer. *Physical Review B* **86**, 155449 (2012).

[33] Alden, J. S. et al. Strain solitons and topological defects in bilayer graphene. *Proceedings of the National Academy of Sciences* **110**, 11256–11260 (2013).

[34] Nam, N. N. T. & Koshino, M. Lattice relaxation and energy band modulation in twisted bilayer graphene. *Physical Review B* **96**, 075311 (2017).

[35] San-Jose, P., González, J. & Guinea, F. Non-Abelian Gauge Potentials in Graphene Bilayers. *Physical Review Letters* **108**, 216802 (2012).

[36] Guinea, F. & Walet, N. R. Electrostatic effects, band distortions, and superconductivity in twisted graphene bilayers. *Proceedings of the National Academy of Sciences* **115**, 13174–13179 (2018).

[37] Tarnopolsky, G., Kruchkov, A. J. & Vishwanath, A. Origin of Magic Angles in Twisted Bilayer Graphene. *Physical Review Letters* **122**, 106405 (2019).

[38] Koshino, M. et al. Maximally Localized Wannier Orbitals and the Extended Hubbard Model for Twisted Bilayer Graphene. *Physical Review X* **8**, 031087 (2018).

[39] Yoo, H. et al. Atomic and electronic reconstruction at the van der Waals interface in twisted bilayer graphene. *Nature Materials* **18**, 448–453 (2019).

[40] Kazmierczak, N. P. et al. Strain fields in twisted bilayer graphene. *Nature Materials* **20**, 956–963 (2021).

[41] Jiang, L. et al. Soliton-dependent plasmon reflection at bilayer graphene domain walls. *Nature Materials* **15**, 840–844 (2016).

[42] Huang, S. et al. Topologically Protected Helical States in Minimally Twisted Bilayer Graphene. *Physical Review Letters* **121**, 037702 (2018).

[43] Ju, L. et al. Topological valley transport at bilayer graphene domain walls. *Nature* **520**, 650–655 (2015).

[44] Yin, L.-J., Jiang, H., Qiao, J.-B. & He, L. Direct imaging of topological edge states at a bilayer graphene domain wall. *Nature Communications* **7**, 11760 (2016).

[45] Rickhaus, P. et al. Transport Through a Network of Topological Channels in Twisted Bilayer Graphene. *Nano Letters* **18**, 6725–6730 (2018).

[46] McGilly, L. J. et al. Visualization of moiré superlattices. *Nature Nanotechnology* **15**, 580–584 (2020).

[47] Krishna Kumar, R. et al. High-temperature quantum oscillations caused by recurring Bloch states in graphene superlattices. *Science* **357**, 181–184 (2017).

[48] Uri, A. et al. Mapping the twist-angle disorder and Landau levels in magic-angle graphene. *Nature* **581**, 47–52 (2020).

[49] Zondiner, U. et al. Cascade of phase transitions and Dirac revivals in magic-angle graphene. *Nature* **582**, 203–208 (2020).

[50] Rozen, A. et al. Entropic evidence for a Pomeranchuk effect in magic-angle graphene. *Nature* **592**, 214–219 (2021).

[51] Stepanov, P. et al. Untying the insulating and superconducting orders in magic-angle graphene. *Nature* **583**, 375–378 (2020).

[52] Arora, H. S. et al. Superconductivity in metallic twisted bilayer graphene stabilized by WSe_2. *Nature* **583**, 379–384 (2020).

[53] Liu, X. et al. Tuning electron correlation in magic-angle twisted bilayer graphene using Coulomb screening. *Science* **371**, 1261–1265 (2021).

[54] Saito, Y., Ge, J., Watanabe, K., Taniguchi, T. & Young, A. F. Independent superconductors and correlated insulators in twisted bilayer graphene. *Nature Physics* **16**, 926–930 (2020).

[55] Cao, Y. et al. Nematicity and competing orders in superconducting magic-angle graphene. *Science* **372**, 264–271 (2021).

[56] Koshino, M. Electronic transmission through AB-BA domain boundary in bilayer graphene. *Physical Review B* **88**, 115409 (2013).

[57] Xu, S. G. et al. Giant oscillations in a triangular network of one-dimensional states in marginally twisted graphene. *Nature Communications* **10**, 3–7 (2019).

[58] Jiang, L., Wang, S., Zhao, S., Crommie, M. & Wang, F. Soliton-Dependent Electronic Transport across Bilayer Graphene Domain Wall. *Nano Letters* **20**, 5936–5942 (2020).

[59] Wang, L. et al. Evidence for a fractional fractal quantum Hall effect in graphene superlattices. *Science* **350**, 1231–1234 (2015).

[60] Wang, D. et al. Thermally Induced Graphene Rotation on Hexagonal Boron Nitride. *Physical Review Letters* **116**, 126101 (2016).

[61] Ribeiro-Palau, R. et al. Twistable electronics with dynamically rotatable heterostructures. *Science* **361**, 690–693 (2018).

[62] Benschop, T. et al. Measuring local moiré lattice heterogeneity of twisted bilayer graphene. *Physical Review Research* **3**, 013153 (2021).

[63] Li, H. et al. Global Control of Stacking-Order Phase Transition by Doping and Electric Field in Few-Layer Graphene. *Nano Letters* **20**, 3106–3112 (2020).

[64] Halbertal, D. et al. Moiré metrology of energy landscapes in van der Waals heterostructures. *Nature Communications* **12**, 242 (2021).

[65] Shabani, S. et al. Deep moiré potentials in twisted transition metal dichalcogenide bilayers. *Nature Physics* **17**, 720–725 (2021).

[66] Zheng, Z. et al. Unconventional ferroelectricity in moiré heterostructures. *Nature* **588**, 71–76 (2020).

[67] Yasuda, K., Wang, X., Watanabe, K., Taniguchi, T. & Jarillo-Herrero, P. Stacking-engineered ferroelectricity in bilayer boron nitride. *Science* **372**, 1458–1462 (2021).

[68] Vizner Stern, M. et al. Interfacial ferroelectricity by van der Waals sliding. *Science* **372**, 1462–1466 (2021).

[69] Woods, C. R. et al. Charge-polarized interfacial superlattices in marginally twisted hexagonal boron nitride. *Nature Communications* **12**, 347 (2021).

[70] Yin, J. et al. Selectively enhanced photocurrent generation in twisted bilayer graphene with van Hove singularity. *Nature Communications* **7**, 10699 (2016).

[71] Deng, B. et al. Strong mid-infrared photoresponse in small-twist-angle bilayer graphene. *Nature Photonics* **14**, 549–553 (2020).

[72] Moon, P. & Koshino, M. Optical absorption in twisted bilayer graphene. *Physical Review B* **87**, 205404 (2013).

[73] Kang, J., Bernevig, B. A. & Vafek, O. Cascades between light and heavy fermions in the normal state of magic angle twisted bilayer graphene. *arXiv:2104.01145* (2021).

[74] Kim, C.-J. et al. Chiral atomically thin films. *Nature Nanotechnology* **11**, 520–524 (2016).

[75] Stauber, T., Low, T. & Gómez-Santos, G. Chiral Response of Twisted Bilayer Graphene. *Physical Review Letters* **120**, 046801 (2018).

[76] Ni, G. X. et al. Plasmons in graphene moiré superlattices. *Nature Materials* **14**, 1217–1222 (2015).

[77] Hu, F. et al. Real-Space Imaging of the Tailored Plasmons in Twisted Bilayer Graphene. *Physical Review Letters* **119**, 247402 (2017).

[78] Sunku, S. S. et al. Photonic crystals for nano-light in moiré graphene superlattices. *Science* **362**, 1153–1156 (2018).

[79] Luo, Y. et al. In situ nanoscale imaging of moiré superlattices in twisted van der Waals heterostructures. *Nature Communications* **11**, 4209 (2020).

[80] Andrei, E. Y. & MacDonald, A. H. Graphene bilayers with a twist. *Nature Materials* **19**, 1265–1275 (2020).

[81] Park, J. M., Cao, Y., Watanabe, K., Taniguchi, T. & Jarillo-Herrero, P. Tunable strongly coupled superconductivity in magic-angle twisted trilayer graphene. *Nature* **590**, 249–255 (2021).

[82] Hao, Z. et al. Electric field–tunable superconductivity in alternating-twist magic-angle trilayer graphene. *Science* **371**, 1133–1138 (2021).

[83] Hasdeo, E. H. & Song, J. C. W. Long-Lived Domain Wall Plasmons in Gapped Bilayer Graphene. *Nano Letters* **17**, 7252–7257 (2017).

[84] Brey, L., Stauber, T., Slipchenko, T. & Martín-Moreno, L. Plasmonic Dirac Cone in Twisted Bilayer Graphene. *Physical Review Letters* **125**, 256804 (2020).

[85] Basov, D. N., Fogler, M. M. & Garcia de Abajo, F. J. Polaritons in van der Waals materials. *Science* **354** (2016).

[86] Low, T. et al. Polaritons in layered two-dimensional materials. *Nature Materials* **16**, 182–194 (2017).

[87] Woessner, A. et al. Highly confined low-loss plasmons in graphene–boron nitride heterostructures. *Nature Materials* **14**, 421–425 (2015).

[88] Tomadin, A., Guinea, F. & Polini, M. Generation and morphing of plasmons in graphene superlattices. *Physical Review B* **90**, 161406 (2014).

[89] Stauber, T. & Kohler, H. Quasi-Flat Plasmonic Bands in Twisted Bilayer Graphene. *Nano Letters* **16**, 6844–6849 (2016).

[90] Lewandowski, C. & Levitov, L. Intrinsically undamped plasmon modes in narrow electron bands. *Proceedings of the National Academy of Sciences* **116**, 20869–20874 (2019).

[91] Novelli, P., Torre, I., Koppens, F. H. L., Taddei, F. & Polini, M. Optical and plasmonic properties of twisted bilayer graphene: Impact of interlayer tunneling asymmetry and ground-state charge inhomogeneity. *Physical Review B* **102**, 125403 (2020).

[92] Fahimniya, A., Lewandowski, C. & Levitov, L. Dipole-active collective excitations in moiré flat bands. *arXiv:2011.02982* (2020).

[93] Woessner, A. et al. Near-field photocurrent nanoscopy on bare and encapsulated graphene. *Nature Communications* **7**, 10783 (2016).

[94] Lundeberg, M. B. et al. Thermoelectric detection and imaging of propagating graphene plasmons. *Nature Materials* **16**, 204–207 (2017).

[95] Woessner, A. et al. Electrical detection of hyperbolic phonon-polaritons in heterostructures of graphene and boron nitride. *npj 2D Materials and Applications* **1**, 25 (2017).

[96] Sunku, S. S. et al. Nano-photocurrent Mapping of Local Electronic Structure in Twisted Bilayer Graphene. *Nano Letters* **20**, 2958–2964 (2020).

[97] Song, J. C. W. & Gabor, N. M. Electron quantum metamaterials in van der Waals heterostructures. *Nature Nanotechnology* **13**, 986–993 (2018).

[98] Weston, A. et al. Atomic reconstruction in twisted bilayers of transition metal dichalcogenides. *Nature Nanotechnology* **15**, 592–597 (2020).

[99] Zomer, P. J., Guimarães, M. H. D., Brant, J. C., Tombros, N. & van Wees, B. J. Fast pick up technique for high quality heterostructures of bilayer graphene and hexagonal boron nitride. *Applied Physics Letters* **105**, 013101 (2014).

[100] Pizzocchero, F. et al. The hot pick-up technique for batch assembly of van der Waals heterostructures. *Nature Communications* **7**, 11894 (2016).

[101] Purdie, D. G. et al. Cleaning interfaces in layered materials heterostructures. *Nature Communications* **9**, 5387 (2018).

[102] Goossens, A. M. et al. Mechanical cleaning of graphene. *Applied Physics Letters* **100**, 073110 (2012).

[103] Rosenberger, M. R. et al. Nano-Squeegee for the Creation of Clean 2D Material Interfaces. *ACS Applied Materials and Interfaces* **10**, 10379–10387 (2018).

[104] Huber, A. J., Keilmann, F., Wittborn, J., Aizpurua, J. & Hillenbrand, R. Terahertz Near-Field Nanoscopy of Mobile Carriers in Single Semiconductor Nanodevices. *Nano Letters* **8**, 3766–3770 (2008).

[105] Fei, Z. et al. Infrared nanoscopy of dirac plasmons at the graphene-SiO_2 interface. *Nano Letters* **11**, 4701–4705 (2011).

[106] Zenhausern, F., O'Boyle, M. P. & Wickramasinghe, H. K. Apertureless near-field optical microscope. *Applied Physics Letters* **65**, 1623–1625 (1994).

[107] Bachelot, R., Gleyzes, P. & Boccara, A. Apertureless near field optical microscopy by local perturbation of a diffraction spot. *Ultramicroscopy* **61**, 111–116 (1995).

[108] Hillenbrand, R. & Keilmann, F. Complex Optical Constants on a Subwavelength Scale. *Physical Review Letters* **85**, 3029–3032 (2000).

[109] Hillenbrand, R., Taubner, T. & Keilmann, F. Phonon-enhanced light–matter interaction at the nanometre scale. *Nature* **418**, 159–162 (2002).

[110] Chen, J. et al. Optical nano-imaging of gate-tunable graphene plasmons. *Nature* **487**, 77–81 (2012).

[111] Fei, Z. et al. Gate-tuning of graphene plasmons revealed by infrared nano-imaging. *Nature* **487**, 82–85 (2012).

[112] Ni, G. X. et al. Fundamental limits to graphene plasmonics. *Nature* **557**, 530–533 (2018).

[113] Dai, S. et al. Tunable Phonon Polaritons in Atomically Thin van der Waals Crystals of Boron Nitride. *Science* **343**, 1125–1129 (2014).

[114] Woessner, A. Exploring flatland nano-optics with graphene plasmons. Ph.D. thesis, Universitat Politècnica de Catalunya (2017).

[115] Keilmann, F. & Hillenbrand, R. Near-field microscopy by elastic light scattering from a tip. *Philosophical Transactions of the Royal Society A: Mathematical, Physical and Engineering Sciences* **362**, 787–805 (2004).

[116] Knoll, B. & Keilmann, F. Enhanced dielectric contrast in scattering-type scanning near-field optical microscopy. *Optics Communications* **182**, 321–328 (2000).

[117] Ocelic, N., Huber, A. & Hillenbrand, R. Pseudoheterodyne detection for background-free near-field spectroscopy. *Applied Physics Letters* **89**, 101124 (2006).

[118] Govyadinov, A. A., Amenabar, I., Huth, F., Carney, P. S. & Hillenbrand, R. Quantitative Measurement of Local Infrared Absorption and Dielectric Function with Tip-Enhanced Near-Field Microscopy. *The Journal of Physical Chemistry Letters* **4**, 1526–1531 (2013).

[119] Govyadinov, A. A. et al. Recovery of permittivity and depth from near-field data as a step toward infrared nanotomography. *ACS Nano* **8**, 6911–6921 (2014).

[120] Schmidt, P. et al. Nano-imaging of intersubband transitions in van der Waals quantum wells. *Nature Nanotechnology* **13**, 1035–1041 (2018).

[121] McLeod, A. S. et al. Model for quantitative tip-enhanced spectroscopy and the extraction of nanoscale-resolved optical constants. *Physical Review B - Condensed Matter and Materials Physics* **90**, 1–17 (2014).

[122] Chen, X. et al. Hybrid Machine Learning for Scanning Near-field Optical Spectroscopy. *arXiv:2105.10551* (2021).

[123] Gabor, N. M. et al. Hot Carrier-Assisted Intrinsic Photoresponse in Graphene. *Science* **334**, 648–652 (2011).

[124] Song, J. C. W., Rudner, M. S., Marcus, C. M. & Levitov, L. S. Hot Carrier Transport and Photocurrent Response in Graphene. *Nano Letters* **11**, 4688–4692 (2011).

[125] Hesp, N. C. H. et al. Nano-imaging photoresponse in a moiré unit cell of minimally twisted bilayer graphene. *Nature Communications* **12**, 1640 (2021).

[126] Alonso-González, P. et al. Acoustic terahertz graphene plasmons revealed by photocurrent nanoscopy. *Nature Nanotechnology* **12**, 31–35 (2017).

[127] Lundeberg, M. B. et al. Tuning quantum nonlocal effects in graphene plasmonics. *Science* **357**, 187–191 (2017).

[128] Tabert, C. J. & Nicol, E. J. Optical conductivity of twisted bilayer graphene. *Physical Review B* **87**, 121402 (2013).

[129] Stauber, T., San-Jose, P. & Brey, L. Optical conductivity, Drude weight and plasmons in twisted graphene bilayers. *New Journal of Physics* **15**, 113050 (2013).

[130] Das Sarma, S. & Li, Q. Intrinsic plasmons in two-dimensional Dirac materials. *Physical Review B* **87**, 235418 (2013).

[131] Ou, J.-Y. et al. Ultraviolet and visible range plasmonics in the topological insulator $\mathrm{Bi}_{1.5}\mathrm{Sb}_{0.5}\mathrm{Te}_{1.8}\mathrm{Se}_{1.2}$. *Nature Communications* **5**, 5139 (2014).

[132] Dubrovkin, A. M. et al. Visible Range Plasmonic Modes on Topological Insulator Nanostructures. *Advanced Optical Materials* **5**, 1600768 (2017).

[133] Fetter, A. L. Edge magnetoplasmons in a two-dimensional electron fluid confined to a half-plane. *Physical Review B* **33**, 3717–3723 (1986).

[134] Hesp, N. C. H. et al. Observation of interband collective excitations in twisted bilayer graphene. *Nature Physics* (2021).

[135] Jiang, B.-Y. et al. Plasmon Reflections by Topological Electronic Boundaries in Bilayer Graphene. *Nano Letters* **17**, 7080–7085 (2017).

[136] Chen, J. et al. Strong Plasmon Reflection at Nanometer-Size Gaps in Monolayer Graphene on SiC. *Nano Letters* **13**, 6210–6215 (2013).

[137] Avouris, P., Heinz, T. F. & Low, T. (eds.) 2D Materials (Cambridge University Press, Cambridge, 2017).

[138] Giuliani, G. & Vignale, G. Quantum Theory of the Electron Liquid (Cambridge University Press, Cambridge, 2005).

[139] Cai, Y., Zhang, L., Zeng, Q., Cheng, L. & Xu, Y. Infrared reflectance spectrum of BN calculated from first principles. *Solid State Communications* **141**, 262–266 (2007).

[140] Koppens, F. H. L., Chang, D. E. & Garcia de Abajo, F. J. Graphene Plasmonics: A Platform for Strong Light–Matter Interactions. *Nano Letters* **11**, 3370–3377 (2011).

[141] Carr, S., Fang, S., Zhu, Z. & Kaxiras, E. Exact continuum model for low-energy electronic states of twisted bilayer graphene. *Physical Review Research* **1**, 013001 (2019).

[142] Guinea, F., Katsnelson, M. I. & Geim, A. K. Energy gaps and a zero-field quantum Hall effect in graphene by strain engineering. *Nature Physics* **6**, 30–33 (2010).

[143] Sharma, G., Trushin, M., Sushkov, O. P., Vignale, G. & Adam, S. Superconductivity from collective excitations in magic-angle twisted bilayer graphene. *Physical Review Research* **2**, 022040 (2020).

[144] Calderón, M. J. & Bascones, E. Correlated states in magic angle twisted bilayer

graphene under the optical conductivity scrutiny. *npj Quantum Materials* **5**, 57 (2020).

[145] Xu, X., Gabor, N. M., Alden, J. S., van der Zande, A. M. & McEuen, P. L. Photo-Thermoelectric Effect at a Graphene Interface Junction. *Nano Letters* **10**, 562–566 (2010).

[146] Lemme, M. C. et al. Gate-Activated Photoresponse in a Graphene p–n Junction. *Nano Letters* **11**, 4134–4137 (2011).

[147] Torre, I. Diffusive solver: a diffusion-equations solver based on FEniCS. *arXiv:2011.04351* (2020).

[148] Lundeberg, M. B. & Koppens, F. H. L. Thermodynamic reciprocity in scanning photocurrent maps. *arXiv:2011.04311* (2020).

[149] Song, J. C. W. & Levitov, L. S. Shockley-Ramo theorem and long-range photocurrent response in gapless materials. *Physical Review B* **90**, 075415 (2014).

[150] Ma, Q. et al. Giant intrinsic photoresponse in pristine graphene. *Nature Nanotechnology* **14**, 145–150 (2019).

[151] Nguyen, M. C., Nguyen, V. H., Nguyen, H.-V., Saint-Martin, J. & Dollfus, P. Enhanced Seebeck effect in graphene devices by strain and doping engineering. *Physica E: Low-dimensional Systems and Nanostructures* **73**, 207–212 (2015).

[152] Caldwell, J. D. et al. Sub-diffractional volume-confined polaritons in the natural hyperbolic material hexagonal boron nitride. *Nature Communications* **5**, 5221 (2014).

[153] Dai, S. et al. Subdiffractional focusing and guiding of polaritonic rays in a natural hyperbolic material. *Nature Communications* **6**, 6963 (2015).

[154] Li, P. et al. Hyperbolic phonon-polaritons in boron nitride for near-field optical imaging and focusing. *Nature Communications* **6**, 7507 (2015).

[155] Sunku, S. S. et al. Hyperbolic enhancement of photocurrent patterns in minimally twisted bilayer graphene. *Nature Communications* **12**, 1641 (2021).

[156] McCann, E. & Koshino, M. The electronic properties of bilayer graphene. *Reports on Progress in Physics* **76**, 056503 (2013).

[157] Liu, X. et al. Tunable spin-polarized correlated states in twisted double bilayer graphene. *Nature* **583**, 221–225 (2020).

[158] Cao, Y. et al. Tunable correlated states and spin-polarized phases in twisted bilayer–bilayer graphene. *Nature* **583**, 215–220 (2020).

[159] Sunku, S. S. et al. Dual-Gated Graphene Devices for Near-Field Nano-imaging. *Nano Letters* **21**, 1688–1693 (2021).

[160] Luo, W. et al. Nanoinfrared Characterization of Bilayer Graphene Conductivity under Dual-Gate Tuning. *Nano Letters* **21**, 5151–5157 (2021).

[161] Kim, C. et al. Fermi Level Pinning at Electrical Metal Contacts of Monolayer Molybdenum Dichalcogenides. *ACS Nano* **11**, 1588–1596 (2017).

[162] Podzorov, V., Gershenson, M. E., Kloc, C., Zeis, R. & Bucher, E. High-mobility field-effect transistors based on transition metal dichalcogenides. *Applied Physics Letters* **84**, 3301–3303 (2004).

[163] Fang, H. et al. High-Performance Single Layered WSe_2 p-FETs with Chemically Doped Contacts. *Nano Letters* **12**, 3788–3792 (2012).

[164] Movva, H. C. P. et al. High-Mobility Holes in Dual-Gated WSe_2 Field-Effect Transistors. *ACS Nano* **9**, 10402–10410 (2015).

[165] Wang, Z. et al. The ambipolar transport behavior of WSe_2 transistors and its analogue circuits. *NPG Asia Materials* **10**, 703–712 (2018).

[166] Das, S. & Appenzeller, J. WSe_2 field effect transistors with enhanced ambipolar characteristics. *Applied Physics Letters* **103**, 103501 (2013).

[167] Rahman, F. Nanostructures in Electronics and Photonics (Pan Stanford, 2016).

[168] Maniyara, R. A. et al. Tunable plasmons in ultrathin metal films. *Nature Photonics* **13**, 328–333 (2019).

[169] Abd El-Fattah, Z. M. et al. Plasmonics in Atomically Thin Crystalline Silver Films. *ACS Nano* **13**, 7771–7779 (2019).

[170] Ju, L. et al. Photoinduced doping in heterostructures of graphene and boron nitride. *Nature Nanotechnology* **9**, 348–352 (2014).

[171] Low, T., Guinea, F., Yan, H., Xia, F. & Avouris, P. Novel Midinfrared Plasmonic Properties of Bilayer Graphene. *Physical Review Letters* **112**, 116801 (2014).

[172] Zhang, Y. et al. Direct observation of a widely tunable bandgap in bilayer graphene. *Nature* **459**, 820–823 (2009).

[173] Fei, Z. et al. Tunneling Plasmonics in Bilayer Graphene. *Nano Letters* **15**, 4973–4978 (2015).

[174] Dai, X., Li, W., Wang, T., Wang, X. & Zhai, C. Bandstructure modulation of two-dimensional WSe_2 by electric field. *Journal of Applied Physics* **117** (2015).

[175] Movva, H. C. et al. Tunable Γ-K Valley Populations in Hole-Doped Trilayer WSe_2. *Physical Review Letters* **120**, 107703 (2018).

[176] Javaid, M., Russo, S. P., Kalantar-Zadeh, K., Greentree, A. D. & Drumm, D. W. Band structure and giant Stark effect in two-dimensional transition-metal dichalcogenides. *Electronic Structure* **1**, 015005 (2018).

[177] Zhao, W. et al. Evolution of Electronic Structure in Atomically Thin Sheets of WS_2 and WSe_2. *ACS Nano* **7**, 791–797 (2013).

[178] Zeng, H. et al. Optical signature of symmetry variations and spin-valley coupling in atomically thin tungsten dichalcogenides. *Scientific Reports* **3**, 1608 (2013).

[179] Lin, Y.-C. et al. Direct Synthesis of van der Waals Solids. *ACS Nano* **8**, 3715–3723 (2014).

[180] Wang, X. et al. Chemical Vapor Deposition Growth of Crystalline Monolayer $MoSe_2$. *ACS Nano* **8**, 5125–5131 (2014).

[181] Eichfeld, S. M. et al. Highly Scalable, Atomically Thin WSe_2 Grown via Metal–Organic Chemical Vapor Deposition. *ACS Nano* **9**, 2080–2087 (2015).

[182] Liu, B. et al. Chemical Vapor Deposition Growth of Monolayer WSe_2 with Tunable Device Characteristics and Growth Mechanism Study. *ACS Nano* **9**, 6119–6127 (2015).

[183] Chen, X. et al. Modern Scattering-Type Scanning Near-Field Optical Microscopy for Advanced Material Research. *Advanced Materials* **31**, 1804774 (2019).

[184] Yang, H. U., Hebestreit, E., Josberger, E. E. & Raschke, M. B. A cryogenic scattering-type scanning near-field optical microscope. *Review of Scientific Instruments* **84**, 023701 (2013).

[185] McLeod, A. S. et al. Nanotextured phase coexistence in the correlated insulator V_2O_3. *Nature Physics* **13**, 80–86 (2017).

[186] Tomaru, T. et al. Vibration analysis of cryocoolers. *Cryogenics* **44**, 309–317 (2004).

[187] Haft, D., Otto, F., Dal Savio, C. & Karrai, K. Optical table. *US Patent App. 15/518,646* (2017).

[188] Vadia, S. et al. Open-cavity in closed-cycle cryostat as a quantum optics platform. *arXiv* 2103.05619 (2021).

[189] Umeda, N. Scanning attractive force microscope using photothermal vibration. *Journal of Vacuum Science and Technology B: Microelectronics and Nanometer Structures* **9**, 1318 (1991).

[190] Mertz, J., Marti, O. & Mlynek, J. Regulation of a microcantilever response by force feedback. *Applied Physics Letters* **62**, 2344–2346 (1993).

[191] Rodriguez, T. R. & Garcia, R. Theory of Q control in atomic force microscopy. *Applied Physics Letters* **82**, 4821–4823 (2003).

[192] Schumacher, Z., Miyahara, Y., Aeschimann, L. & Grütter, P. Improved atomic force microscopy cantilever performance by partial reflective coating. *Beilstein Journal of Nanotechnology* **6**, 1450–1456 (2015).

[193] Voigtländer, B. Scanning Probe Microscopy. NanoScience and Technology (Springer Berlin Heidelberg, Berlin, Heidelberg, 2015).

[194] Giles, A. J. et al. Ultralow-loss polaritons in isotopically pure boron nitride. *Nature Materials* **17**, 134–139 (2018).

[195] Ni, G. et al. Long-Lived Phonon Polaritons in Hyperbolic Materials. *Nano Letters* **21**, 5767–5773 (2021).

[196] Pong, W.-T. & Durkan, C. A review and outlook for an anomaly of scanning tunnelling microscopy (STM): superlattices on graphite. *Journal of Physics D: Applied Physics* **38**, R329–R355 (2005).

[197] Xue, J. et al. Scanning tunnelling microscopy and spectroscopy of ultra-flat graphene on hexagonal boron nitride. *Nature Materials* **10**, 282–285 (2011).

[198] Decker, R. et al. Local Electronic Properties of Graphene on a BN Substrate via Scanning Tunneling Microscopy. *Nano Letters* **11**, 2291–2295 (2011).

[199] Park, C.-H., Yang, L., Son, Y.-W., Cohen, M. L. & Louie, S. G. Anisotropic behaviours of massless Dirac fermions in graphene under periodic potentials. *Nature Physics* **4**, 213–217 (2008).

[200] Park, C.-H., Yang, L., Son, Y.-W., Cohen, M. L. & Louie, S. G. New Generation of Massless Dirac Fermions in Graphene under External Periodic Potentials. *Physical Review Letters* **101**, 126804 (2008).

[201] Yankowitz, M. et al. Emergence of superlattice Dirac points in graphene on hexagonal boron nitride. *Nature Physics* **8**, 382–386 (2012).

[202] Zhang, Y.-H., Mao, D. & Senthil, T. Twisted bilayer graphene aligned with hexagonal boron nitride: Anomalous Hall effect and a lattice model. *Physical Review Research* **1**, 033126 (2019).

[203] Bultinck, N., Chatterjee, S. & Zaletel, M. P. Mechanism for Anomalous Hall Ferromagnetism in Twisted Bilayer Graphene. *Physical Review Letters* **124**, 166601 (2020).

[204] Lin, J.-X. et al. Spin-orbit driven ferromagnetism at half moiré filling in magic-angle twisted bilayer graphene. *arXiv:2102.06566* 1–28 (2021).

[205] Stepanov, P. et al. Competing zero-field Chern insulators in Superconducting Twisted Bilayer Graphene. *arXiv:2012.15126* (2020).

[206] Wang, L. et al. New Generation of Moiré Superlattices in Doubly Aligned hBN/Graphene/hBN Heterostructures. *Nano Letters* **19**, 2371–2376 (2019).

[207] Finney, N. R. et al. Tunable crystal symmetry in graphene–boron nitride heterostructures with coexisting moiré superlattices. *Nature Nanotechnology* **14**, 1029–1034 (2019).

[208] Wang, Z. et al. Composite super-moiré lattices in double-aligned graphene heterostructures. *Science Advances* **5**, eaay8897 (2019).

[209] Chen, G. et al. Evidence of a gate-tunable Mott insulator in a trilayer graphene moiré superlattice. *Nature Physics* **15**, 237–241 (2019).

[210] Eckmann, A. et al. Raman Fingerprint of Aligned Graphene/h-BN Superlattices. *Nano Letters* **13**, 5242–5246 (2013).

[211] Han, T. et al. Accurate Measurement of the Gap of Graphene-hBN Moiré Superlattice through Photocurrent Spectroscopy. *Physical Review Letters* **126**, 146402 (2021).

[212] Woods, C. R. et al. Commensurate–incommensurate transition in graphene on hexagonal boron nitride. *Nature Physics* **10**, 451–456 (2014).

[213] Mesple, F. et al. Heterostrain rules the flat-bands in magic-angle twisted graphene layers. *arXiv:2012.02475* (2020).

[214] Parker, D. E., Soejima, T., Hauschild, J., Zaletel, M. P. & Bultinck, N. Strain-Induced Quantum Phase Transitions in Magic-Angle Graphene. *Physical Review Letters* **127**, 027601 (2021).

[215] Pereira, V. M., Castro Neto, A. H. & Peres, N. M. R. Tight-binding approach to uniaxial strain in graphene. *Physical Review B* **80**, 045401 (2009).

[216] Naumis, G. G., Barraza-Lopez, S., Oliva-Leyva, M. & Terrones, H. Electronic and optical properties of strained graphene and other strained 2D materials: a review. *Reports on Progress in Physics* **80**, 096501 (2017).

[217] Blakslee, O. L., Proctor, D. G., Seldin, E. J., Spence, G. B. & Weng, T. Elastic Constants of Compression-Annealed Pyrolytic Graphite. *Journal of Applied Physics* **41**, 3373–3382 (1970).

[218] Cosma, D. A., Wallbank, J. R., Cheianov, V. & Fal'ko, V. I. Moiré pattern as a magnifying glass for strain and dislocations in van der Waals heterostructures. *Faraday Discuss.* **173**, 137–143 (2014).

[219] Jiang, Y. et al. Visualizing Strain-Induced Pseudomagnetic Fields in Graphene through an hBN Magnifying Glass. *Nano Letters* **17**, 2839–2843 (2017).

[220] Maciá-Barber, E. Thermoelectric materials: Advances and applications (Pan Stanford Publishing, 2015).

[221] Rivera, N. & Kaminer, I. Light–matter interactions with photonic quasiparticles. *Nature Reviews Physics* **2**, 538–561 (2020).

[222] Fitzgerald, J. M., Narang, P., Craster, R. V., Maier, S. A. & Giannini, V. Quantum Plasmonics. *Proceedings of the IEEE* **104**, 2307–2322 (2016).

[223] Parker, M. Physics of Optoelectronics: 104 (Optical Science and Engineering) (CRC Press; 1st Edition, 2005).

[224] Steiner, T. Semiconductor Nanostructures for Optoelectronic Applications (Artech House Publishers, 2004).

[225] Zhao, W. et al. Efficient Fizeau drag from Dirac electrons in monolayer graphene. *Nature* **594**, 517–521 (2021).

[226] Dong, Y. et al. Fizeau drag in graphene plasmonics. *Nature* **594**, 513–516 (2021).

[227] Cocker, T. L., Jelic, V., Hillenbrand, R. & Hegmann, F. A. Nanoscale terahertz scanning probe microscopy. *Nature Photonics* **15**, 558–569 (2021).

[228] Spietz, L., Teufel, J. & Schoelkopf, R. J. A Twisted Pair Cryogenic Filter. *arXiv* cond–mat/0601316 (2006).

[229] Torre, I., Katsnelson, M. I., Diaspro, A., Pellegrini, V. & Polini, M. Lippmann-Schwinger theory for two-dimensional plasmon scattering. *Physical Review B* **96**, 035433 (2017).

[230] Tielrooij, K.-J. et al. Out-of-plane heat transfer in van der Waals stacks through electron–hyperbolic phonon coupling. *Nature Nanotechnology* **13**, 41–46 (2018).

[231] Alnæs, M. S. et al. The FEniCS Project Version 1.5. *Archive of Numerical Software* **3**, 9–23 (2015).

[232] Gunde, M. K. Vibrational modes in amorphous silicon dioxide. *Physica B: Condensed Matter* **292**, 286–295 (2000).

[233] Haastrup, S. et al. The Computational 2D Materials Database: high-throughput modeling and discovery of atomically thin crystals. *2D Materials* **5**, 042002 (2018).